NASA/TP–2020-5005040

Electron Beam Freeform Fabrication of Dissimilar Materials: Cracking in Inconel® 625 Deposited on GRCop-84

Stephen J. Hales
Langley Research Center, Hampton, Virginia

Christopher S. Domack
Analytical Mechanics Associates, Inc., Hampton, Virginia

Karen M. Taminger
Langley Research Center, Hampton, Virginia

August 2020

NASA STI Program . . . in Profile

Since its founding, NASA has been dedicated to the advancement of aeronautics and space science. The NASA scientific and technical information (STI) program plays a key part in helping NASA maintain this important role.

The NASA STI program operates under the auspices of the Agency Chief Information Officer. It collects, organizes, provides for archiving, and disseminates NASA's STI. The NASA STI program provides access to the NTRS Registered and its public interface, the NASA Technical Reports Server, thus providing one of the largest collections of aeronautical and space science STI in the world. Results are published in both non-NASA channels and by NASA in the NASA STI Report Series, which includes the following report types:

- TECHNICAL PUBLICATION. Reports of completed research or a major significant phase of research that present the results of NASA Programs and include extensive data or theoretical analysis. Includes compilations of significant scientific and technical data and information deemed to be of continuing reference value. NASA counter-part of peer-reviewed formal professional papers but has less stringent limitations on manuscript length and extent of graphic presentations.

- TECHNICAL MEMORANDUM. Scientific and technical findings that are preliminary or of specialized interest, e.g., quick release reports, working papers, and bibliographies that contain minimal annotation. Does not contain extensive analysis.

- CONTRACTOR REPORT. Scientific and technical findings by NASA-sponsored contractors and grantees.

- CONFERENCE PUBLICATION. Collected papers from scientific and technical conferences, symposia, seminars, or other meetings sponsored or co-sponsored by NASA.

- SPECIAL PUBLICATION. Scientific, technical, or historical information from NASA programs, projects, and missions, often concerned with subjects having substantial public interest.

- TECHNICAL TRANSLATION. English-language translations of foreign scientific and technical material pertinent to NASA's mission.

Specialized services also include organizing and publishing research results, distributing specialized research announcements and feeds, providing information desk and personal search support, and enabling data exchange services.

For more information about the NASA STI program, see the following:

- Access the NASA STI program home page at *http://www.sti.nasa.gov*

- E-mail your question to help@sti.nasa.gov

- Phone the NASA STI Information Desk at 757-864-9658

- Write to:
  NASA STI Information Desk
  Mail Stop 148
  NASA Langley Research Center
  Hampton, VA 23681-2199

NASA/TP–2020-5005040

Electron Beam Freeform Fabrication of Dissimilar Materials: Cracking in Inconel® 625 Deposited on GRCop-84

Stephen J. Hales
Langley Research Center, Hampton, Virginia

Christopher S. Domack
Analytical Mechanics Associates, Inc., Hampton, Virginia

Karen M. Taminger
Langley Research Center, Hampton, Virginia

August 2020

Abstract

An additive manufacturing technology, known as electron beam freeform fabrication, was used in the construction of a prototype rocket engine component. The structural configuration comprised a cylindrical combustion chamber integrated with a conical thrust nozzle with an approximate wall thickness of 20 mm. The bi-metallic design exploited the physical properties of a Cu-based alloy for the thermal liner and the mechanical properties of a Ni-based alloy for the surrounding structural jacket. The successful project culminated in the radial deposition of Inconel® 625[1] alloy cladding onto a pre-fabricated, complex structure of GRCop-84 alloy.

Proof-of-concept necessitated evaluation of the integrity of the interface between the dissimilar materials. The original aim of this sub-project was the production of test coupon material for extracting standard tensile specimens across the union between Inconel 625 and GRCop-84. A series of deposition trials failed to produce suitable material due to circumferential cracking during processing. Consequently, the effort shifted to a failure investigation and focused on two ring sections that bracketed the average bulk temperature used during the parametric studies.

Ring 1 and Ring 4 represented the lower and upper limit of the substrate temperature (T_{Sub}) maintained during the trials. The significant difference between the deposition protocols was the frequency and duration of static cooling intervals between successive layers. Deposition of Ring 1 was paused between every layer in order to equilibrate at $T_{Sub} \leq 250°C$, whereas deposition at T_{Sub} = 400-550°C proceeded uninterrupted for Ring 4. Significantly, premature cracking was detected during actual deposition of Ring 1, but only during post-deposition cooling of Ring 4.

During the layer additive builds, axial deposition of the 19 mm thick ring sections comprised seven overlapping beads in each of the ≈ 2 mm thick layers. The sequence was such that the first bead was deposited on the inside diameter and the seventh bead on the outside diameter of the ring. Macroscopically, cracking started around the outer wall and progressed radially towards the inner wall, extending through ≥ 80% of wall thickness. The cracks were confined to an interlayer boundary within the deposited material, rather than at the interface between the GRCop-84 substrate and the Inconel 625 deposit, in both Ring 1 and Ring 4.

Microstructural characteristics consisted of a cellular dendritic structure oriented in the build direction and epitaxial growth between the majority of deposited layers. Common to Ring 1 and Ring 4, the interlayer boundary that separated during deposition processing proved to be the exception. The isolated boundary was continuously decorated with a cupronickel phase and exhibited a lack of microstructural bridging (epitaxial growth). The probable fracture mode, fracture mechanisms and driving forces responsible for the premature cracking were identified.

Failure analyses indicated crack formation during deposition and crack opening during periods of static cooling in both Ring 1 and Ring 4. The fractographic evidence was consistent with the unique interlayer boundary behaving like a high-angle GB. Decohesive rupture through a GB phase was the intergranular fracture mode in the semi-solid and solid state. At super-solidus temperatures, the hot cracking via a weld metal liquation cracking mechanism was driven by solidification shrinkage. At sub-solidus temperatures, the warm/cold cracking via a tensile overload/yield-strength-mismatch mechanism was driven by differential thermal contraction.

---

[1] *INCONEL® is a registered trademark of Special Metals Corporation, New Hartford, NY, USA.*

Table of Contents

Table of Figures

Table of Tables

Symbols and Abbreviations

Symbols

at.% .....atomic percentage

Cr.....chromium

Cu.....copper

ΔT.....temperature differential

Mo.....molybdenum

MPa.....megapascals

Nb.....niobium

Ni.....nickel

T .....temperature

T_l .....liquidus temperature

T_m .....melting point

T_s .....solidus temperature

T_{Sub} .....substrate temperature

vol.% .....volume percentage

wt.% .....weight percentage

σ_y .....yield strength

Abbreviations

AM .....additive manufacturing

BF.....bright field (imaging)

BSE .....back-scattered electron (imaging)

B*X* .....bead *X* (*X* = 1 to 7)

compo.....compositional (imaging mode)

CTE .....coefficient of thermal expansion

DDC .....ductility dip cracking

DED .....directed energy deposition

EB .....electron beam

EBF^3.....electron beam freeform fabrication

EDS .....energy-dispersive spectrometry

FB.....fusion boundary
FZ.....fusion zone
GB.....grain boundary
GRC.....Glenn Research Center
HAZ.....heat-affected zone
HIP.....hot isostatic pressing
IGF.....intergranular fracture
LaRC.....Langley Research Center
LC.....liquation cracking
LCF.....low-cycle fatigue
LME.....liquid metal embrittlement
L*Y*.....layer *Y* (*Y* = 1 to 4)
OM.....optical metallography
PM.....powder metallurgy
PMZ.....partially-melted zone
PWHT.....post-weld heat treatment
RC.....reheat cracking
SAC.....strain-age cracking
SC.....solidification cracking
SE.....secondary electron (imaging)
SEM.....scanning electron microscopy
SGB.....solidification grain boundary
S-L.....solid-liquid (interface)
SLM.....selective laser melting
STR.....solidification temperature range
TMF.....thermo-mechanical fatigue
topo.....topographic (imaging mode)
WMLC.....weld metal liquation cracking
YSM.....yield-strength-mismatch

1. Introduction

1.1. Electron Beam Freeform Fabrication

1.1.1. Construction of Rocket Engine Components

Additive manufacturing (AM) of multi-alloy, integrated structures is one element of NASA's 'Low Cost Upper Stage Propulsion' program [ref. 1]. The philosophy adopted for design and construction of a liquid rocket engine component is captured in figure 1. As shown in figure 1(a), the prototype component comprises a regeneratively-cooled, combustion chamber integrated with a thrust nozzle. The key features of the structure are the thermal liner and structural jacket, which are bonded together and perform different roles [ref. 2]. The function of the liner material is to accommodate the operating temperatures, and that of the jacket material is to sustain the operating pressures. The bi-metallic design exploits the thermal properties of GRCop-84 for the inner structure, and the elevated temperature tensile properties of Inconel 625 for the outer cladding.

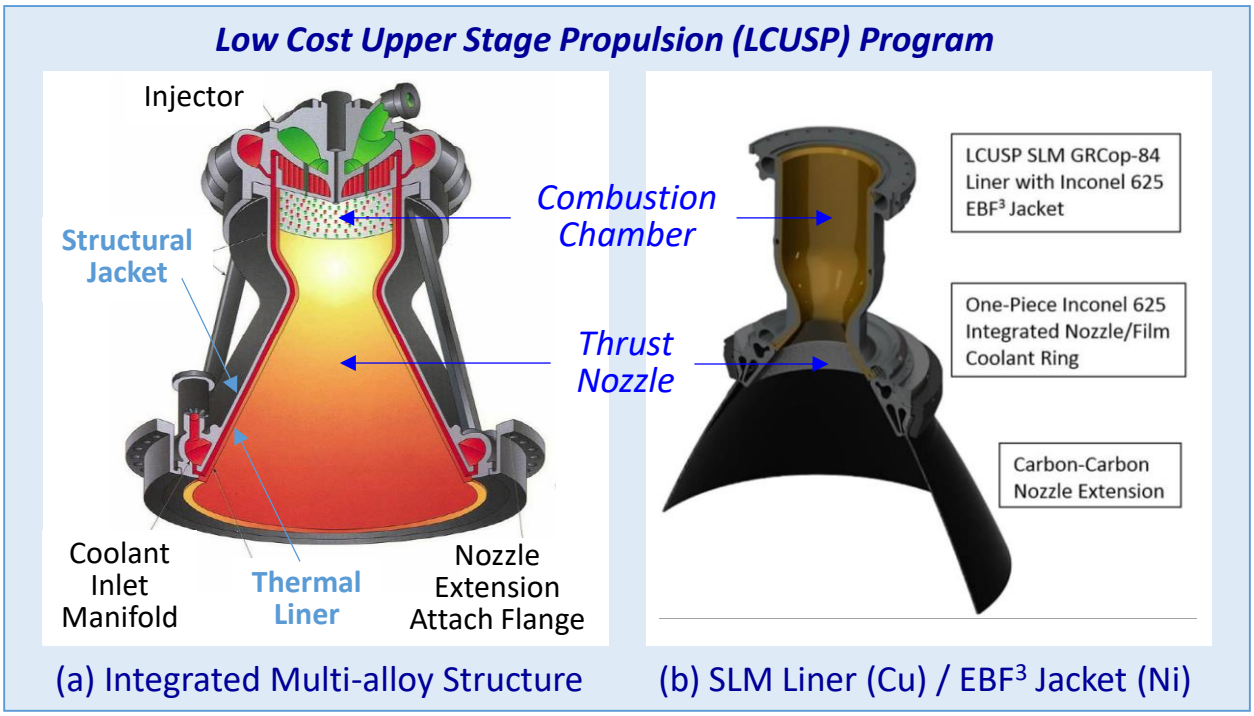

Figure 1. Prototype liquid rocket engine component: (a), integrated combustion chamber/thrust nozzle structure [ref. 2]; (b), GRCop-84 thermal liner fabricated via SLM and Inconel 625 structural jacket fabricated via EBF^3 [ref. 1].

As shown in figure 1(b), construction of the combustion chamber/thrust nozzle component utilizes both AM technology and dissimilar materials. GRCop-84 is a powder metallurgy (PM) alloy developed at NASA-GRC that is customarily processed using standardized powder-bed fusion technology [ref. 3]. Inconel 625 is a common high temperature alloy that is available in the form of wire feedstock for directed-energy deposition (DED) processes. The 10 mm-thick GRCop-84 liner, containing complex cooling channels, is manufactured by selective laser melting (SLM) [ref. 1]. The 10 mm-thick Inconel 625 jacket is then radially deposited on the external surface of the pre-fabricated liner using electron beam freeform fabrication (EBF^3), a technology patented by NASA-LaRC [ref. 4].

The concept of electron beam (EB)-assisted AM has been around since the early 1990s, with pioneering research being conducted at Massachusetts Institute of Technology [ref. 5]. In general, processing is conducted within a vacuum chamber and the EB gun/wire feed assembly is capable of limited travel. The substrate moves in a predetermined pattern during deposition, similar to computer-aided machining. A small pool of molten metal is created that solidifies immediately after the EB has passed. The deposited material rapidly gains sufficient structural strength to be self-supporting. The process is repeated in a layer-wise fashion, resulting in a near-net-shape component that frequently only requires finish machining and heat treatment.

Careful process control is required to ensure that transient thermal effects are minimized until the deposit cools to ambient temperatures. *In vacuo* processing dictates that heat dissipation is primarily confined to conduction through the substrate beneath the deposited material [ref. 6]. As a consequence, optimal process parameters minimize residual stresses by regulating the highly-directional temperature gradient and entire cooling profile [ref. 7]. The deposition strategy adopted during wire feed, DED processing can also be exploited to avoid distortion and cracking during solidification [ref. 8]. Customarily, an effective strategy must include the deposition sequence and layer pattern, which may require adjustment with build height [ref. 9].

The EBF^3 facility at NASA-LaRC, which is a modified version of a Sciaky 42 kW EB welder, is shown in figure 2(a). The dimensions of the effective working volume are 1.8 m x 0.9 m x 0.6 m and the typical operating pressure of the vacuum chamber is 10^{-5} torr [ref. 10]. Employing the system for radial deposition of the rocket engine component is shown in figure 2(b). The EB gun and wire feeder translate along the X direction as the horizontally mounted substrate rotates about the X axis. A constant working distance is maintained with increasing build height by raising the EB gun in the Z direction. The deposition sequence is such that material is deposited in discrete sections of the component profile for thermal management purposes. In this particular image, the GRCop-84 substrate is partially-covered with the first layer of Inconel 625.

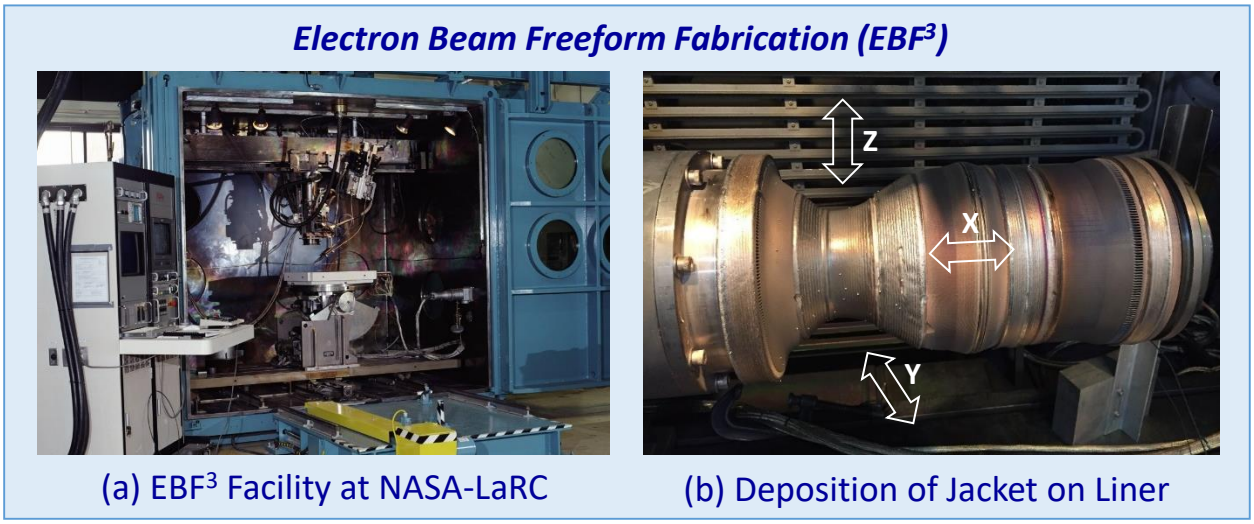

Figure 2. Fabrication of prototype bi-metallic combustion chamber/thrust nozzle: (a), EBF^3 facility at NASA-LaRC; (b), partial deposition of Inconel 625 structural jacket on to GRCop-84 thermal liner.

The schematics contained in figure 3 illustrate the radial deposition of an Inconel 625 build onto a GRCop-84 substrate. The EB is oriented vertically, the wire feeder is inclined at a fixed angle, and the cylindrical substrate is oriented horizontally, rotating about the X axis. Figure 3(a)

shows the sequence for the initial layer of beads and figure 3(b) how subsequent layers of beads are deposited. Each bead is deposited as an individual ring and the EB gun/wire feeder assembly is translated horizontally via a pre-determined step function that permits a 50% overlap between consecutive beads. The process is interrupted momentarily after each bead is deposited in order to re-position the assembly. The start/stop point in adjacent beads is continually advanced so that any associated material discontinuities are dispersed around the circumference.

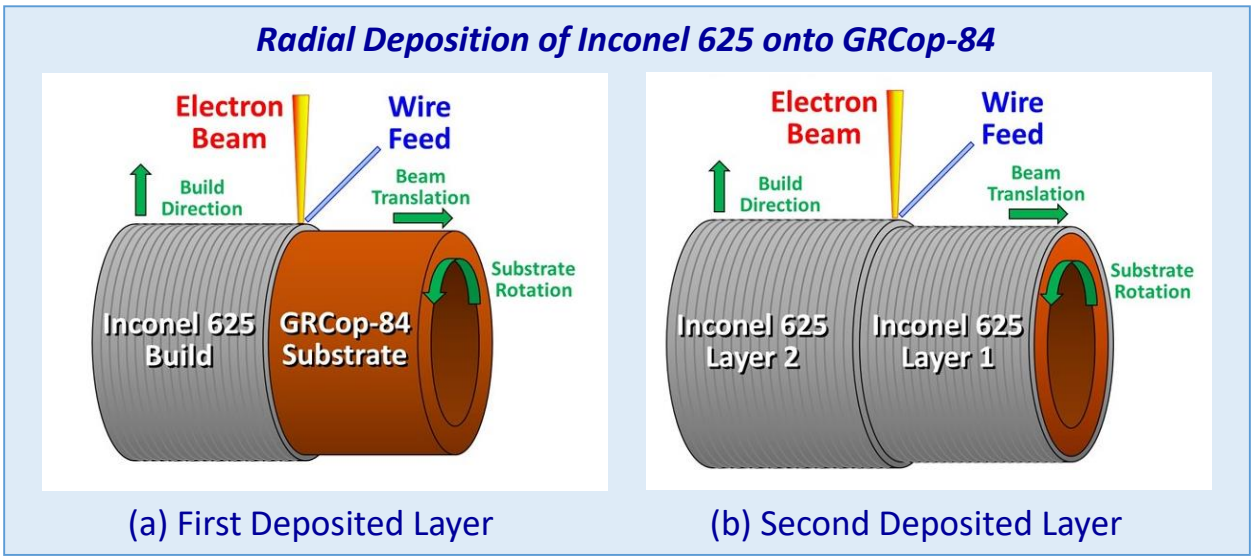

Figure 3. Radial deposition of Inconel 625 onto GRCop-84. Electron beam translation and substrate rotation: (a), first deposited layer; (b), second deposited layer.

Preceding studies dictated that the processing conditions used for the initial layer were different than those used for subsequent layers. Additional beam power was required to ensure good adherence of the deposit to the substrate for this dissimilar alloy combination [ref. 11]. The initial layer involved Inconel 625-to-GRCop-84 deposition, whereas the remaining layers involved Inconel 625-to-Inconel 625 deposition. The process was also interrupted between layers in order to maintain the substrate at a target temperature. The LaRC EBF^3 system contained no provision for active cooling during deposition or post-deposition operations. Consequently, the process variable used to moderate the average bulk temperature was the time interval allowed between successive layers. The duration of these beam-off pauses increased as the target substrate temperature decreased to accommodate the additional cooling required.

1.1.2. Production of Test Coupon Materials

Qualification of a prototype rocket engine component via EBF^3 required evaluation of the structural integrity of the thermal liner/structural jacket interface. However, the complex shape and ≈ 20 mm wall thickness of the combustion chamber/rocket nozzle component are not compatible with the extraction of mechanical test blanks. As illustrated in figure 4(a), fabrication of suitable bimetallic tensile coupons is best fulfilled by axial deposition of Inconel 625 onto the end of a cylindrical GRCop-84 substrate. Note that the build is artificially separated from the substrate for clarity in the schematic.

Similar to radial deposition, the EB is oriented vertically and the wire feeder is inclined at the same fixed angle. The EB gun/wire feeder assembly also translates along the X axis. In contrast with radial deposition, the cylindrical substrate is oriented vertically and rotates about the Z axis.

Customarily, deposition commences at the inner wall and progresses towards the outer wall for every layer. Each layer comprises beads individually deposited via a pre-determined step function that retains the designated overlap. The process is paused after each complete rotation to re-position the assembly and interrupted after each full layer to allow equilibration at the target substrate temperature. Again, the start/stop point is continuously varied between adjacent beads to disperse any material discontinuities created by the pause in deposition.

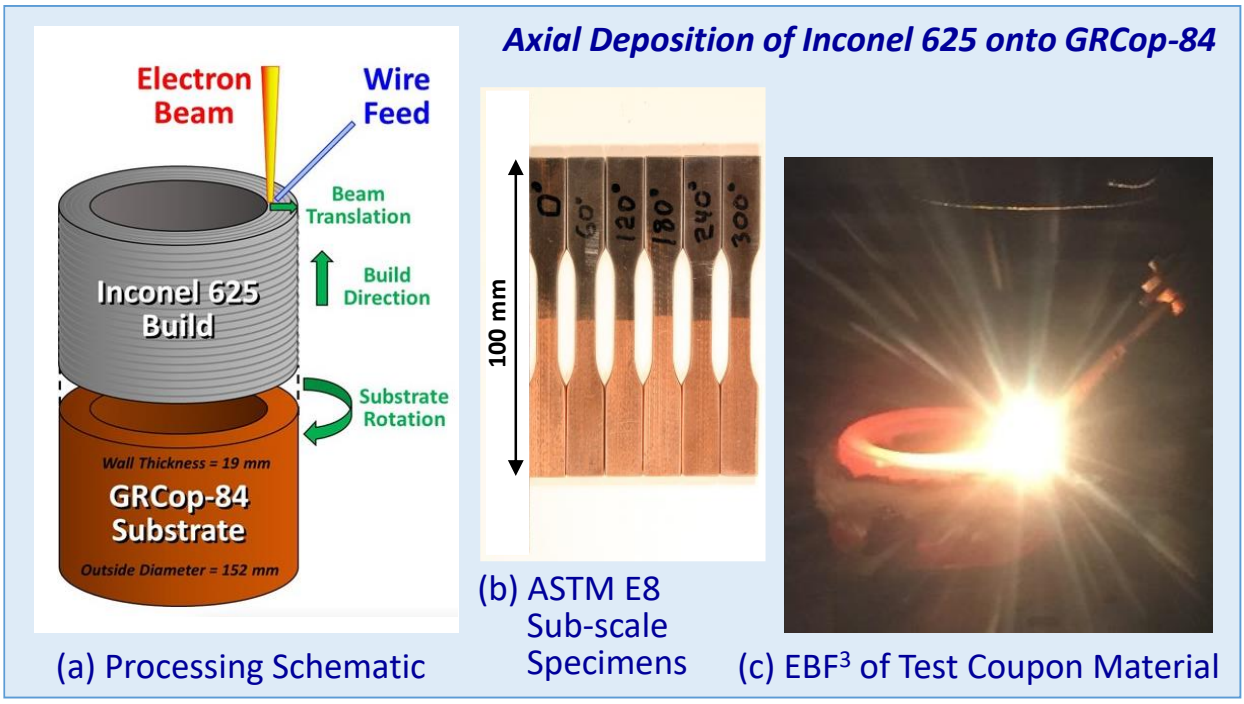

Figure 4. Axial deposition of Inconel 625 onto GRCop-84: (a), schematic of electron beam translation and substrate rotation; (b), typical ASTM E8 specimens for evaluating interface properties; (c), EBF^3 of test coupon material at LaRC.

An example of a series of sub-size specimens to assess the mechanical properties of the junction between GRCop-84 and Inconel 625 is presented in figure 4(b). The substrate/build interface is located at the center of the gage section of the ASTM E8 sub-scale tensile specimens. Representative standard dimensions comprise 100 mm long by 10 mm wide by 6 mm thick, with a gage length and width of 25 mm and 6 mm, respectively. Axial deposition of test coupon material utilizing the LaRC EBF^3 system is shown in figure 4(c). It is essential that the processing conditions are comparable to those used for constructing the rocket engine component. This guarantees that the interfaces created between Inconel 625 and GRCop-84 during axial and radial deposition exhibit similar characteristics.

1.1.3. Metallurgy of Inconel 625 and GRCop-84

Inconel 625 has a nominal composition of Ni-25Cr-5.6Mo-1.5Nb (at.%), exhibits a liquidus temperature (T_l) of 1,350°C and a solidus temperature (T_s) of 1,290°C, which equates to a solidification temperature range (STR) of $\Delta T = 60$°C [ref. 12]. Primarily a solid solution-strengthened alloy, supplementary strength contributions are provided by intermetallic phases

based on $Ni_3(Nb, Mo)$, $Ni_2(Cr, Mo)$ and Cr_2Nb [ref. 13]. The alloy is also prone to the formation of undesirable A_2B-type Laves phases during solidification processing [ref. 14].

Complex $(Ni, Cr)_2(Nb, Mo)$-based agglomerates tend to segregate in interdendritic and intergranular regions of the microstructure [ref. 15]. These brittle phases are known to be detrimental to notch-sensitive mechanical properties of Inconel 625, particularly when distributed as a continuous network [ref. 16]. In monolithic form, the alloy has proven compatible with AM technology due to the lack of allotropic transformations, low residual stresses, and minimal distortion [ref. 17]. Powder bed methods include consolidation using a laser beam [ref. 18] or EB [ref. 19] and wire feed methods include pulsed plasma arc deposition [ref. 20].

The specified composition of GRCop-84 is Cu-8Cr-4Nb (at.%), with an almost pure Cu matrix that results in a singular melting point of $T_m \approx 1080°C$ [refs. 21 and 22]. As a PM alloy, rapidly solidified particulate has traditionally been consolidated via extrusion and hot isostatic pressing (HIP) [ref. 23]. Selective laser melting (SLM) methodology, combined with HIP, has recently emerged as a viable candidate for fabricating more complex shapes with internal features [ref. 1].

Primarily a dispersion-strengthened material, the consolidation goal is to retain a fine, uniform distribution of particles within the matrix. The Cr_2Nb dispersoids that reside in bulk product are typically 0.5-1.0 μm in diameter, with a theoretical volume fraction of 13.5 vol.% [refs. 24 and 25]. A detrimental effect associated with EB melting of GRCop-84 has proved to be the decrease in mechanical properties caused by coarsening and agglomeration of these dispersoids [ref. 26].

1.2. EBF³ Involving Dissimilar Alloys

1.2.1. Weld Microstructures in Ni-based Alloys

In general, weld solidification initiates by epitaxial nucleation at the fusion boundary (FB) and progresses via competitive grain growth into the weld pool. Figure 5 shows a plan view of a typical weld pass with the FB separating the re-solidified weld metal from the un-melted base metal. Epitaxial nucleation at the FB is illustrated in figure 5(a) [ref. 27]. Individual grains extend from the polycrystalline aggregate, each possessing the crystallographic orientation of a parent grain. Competitive growth into the weld pool is illustrated in figure 5(b) [ref. 28]. Those grains with the preferential growth direction (<100> in f.c.c. metals) oriented closest to the heat flow direction tend to progressively eliminate competitors. Figure 6 summarizes the various modes of solidification that are commonly observed in f.c.c. metals [ref. 29]. These modes categorize the differing morphological forms that the solid-liquid (S-L) interface may assume during the competitive growth phase. The microstructures most frequently associated with fusion welding of Ni-base alloys exhibit cellular dendritic or columnar dendritic characteristics (figure 6(c) and 6(d)) [ref. 27].

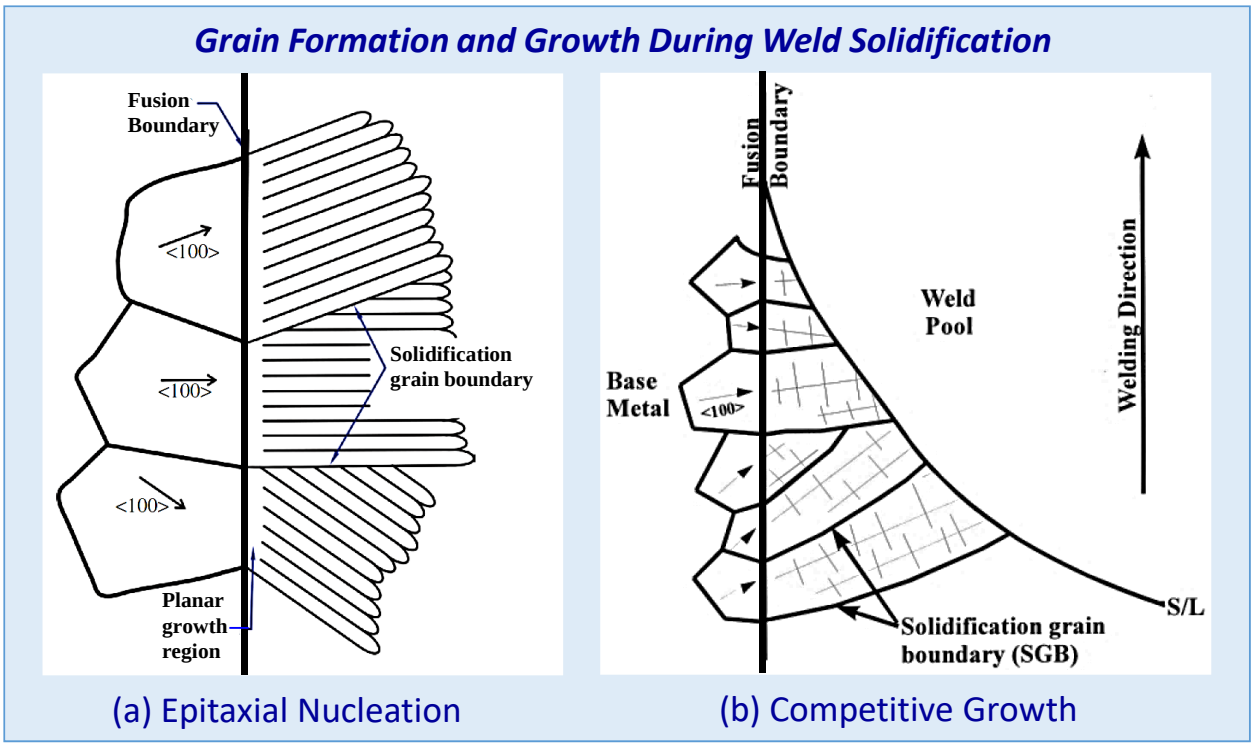

Figure 5. Grain formation and growth during weld solidification: (a), epitaxial nucleation at the fusion boundary [ref. 27]; (b), competitive growth into the weld pool [ref. 28]. Note that low-angle SGBs are usually created between the different colony orientations.

The distinguishing feature between these solidification modes is the degree of dendrite branching. Cellular growth is dominated by primary dendrites, whereas columnar growth incorporates prolific secondary dendrite arms. The solidification mode is governed by the temperature gradient in the molten metal and the solidification growth rate. The contours of the S-L interface conform with the array of advancing dendritic grains. Low melting point constituent accumulates ahead of this interface and the distribution is governed by the mode of solidification. Free-flowing between primary dendrites, terminal liquid tends to be propelled by the S-L interface during cellular dendritic growth, but entrapment between secondary dendrites is prevalent during columnar dendritic growth.

Inconel 625 solidifies as a fully austenitic grain structure (γ phase) during fusion welding, with segregation of alloying elements at interfaces created within the microstructure [ref. 30]. In single-pass welds, the grains are dendritic in nature and exhibit crystallographic epitaxy with the base metal. Subsequently, competitive growth defines the final grain morphology and the arrangement of these solidification grain boundaries (SGBs). Most of the SGBs that form are low-angle in nature because the misorientation between neighboring dendrites tends to be small. In the semi-solid state, this will govern the accumulation of terminal liquid between the impinging dendritic grains at the end of solidification. Common in low Si/low C versions, the intermetallics that can form during solidification of monolithic Inconel 625 comprise $(Ni, Cr)_2(Nb, Mo)$ Laves phases and limited NbC carbides [refs. 31 and 32].

Modes of Grain Growth During Weld Solidification

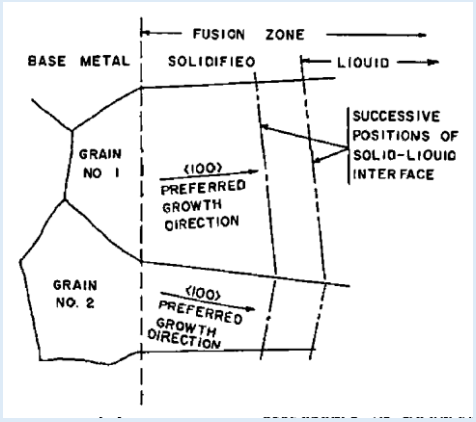

(a) Planar

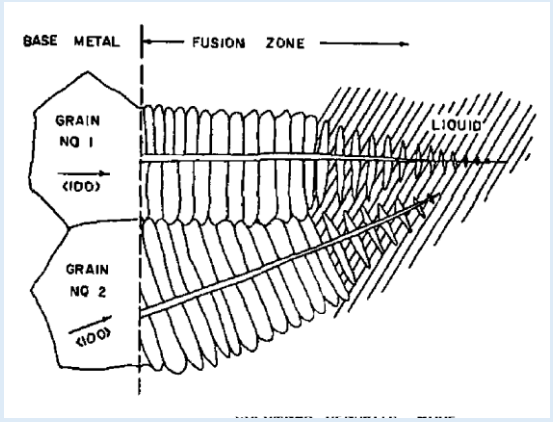

(d) Columnar Dendritic

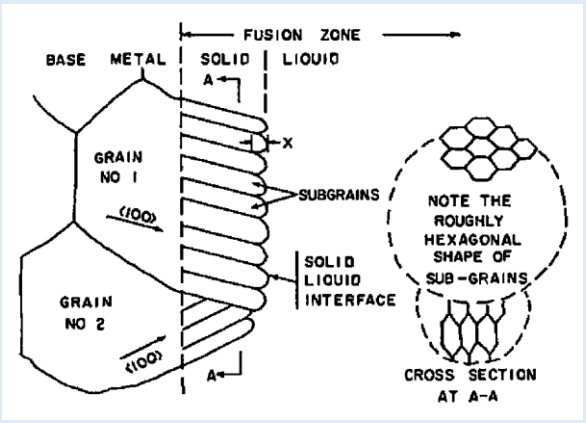

(b) Cellular

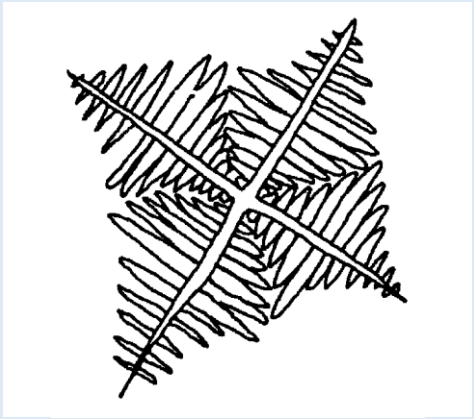

(e) Equiaxed Dendritic

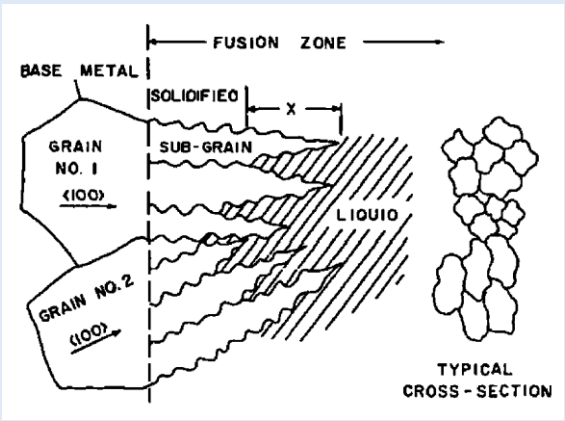

(c) Cellular Dendritic

Figure 6. Modes of grain growth during weld solidification: (a), planar; (b), cellular; (c), cellular dendritic; (d), columnar dendritic; (e), equiaxed dendritic. Active mode depends on temperature gradient and solidification rate [ref. 29].

In multi-pass welds, the dendritic microstructure usually exhibits epitaxial growth across inter-bead boundaries within the weld metal [ref. 27]. In DED/AM deposits, dendritic grains tend to extend through multiple layers and assume the form of columnar architectures oriented roughly parallel with the primary heat flux direction [ref. 33]. In both microstructures, deposited metal is subject to repeated thermal excursions of progressively decreasing intensity. Beads directly adjacent to the FB are partially re-melted, and more remote beads undergo varying levels of heat treatment. The net result is that solute segregation in the pre-existent, dendritic microstructure is augmented and redistributed during subsequent weld passes. Pipe diffusion or capillary action is accelerated and causes low melting point solute accumulation at the majority of interfaces [ref. 15]. Under certain solidification conditions, microstructural bridging can be disrupted by the presence of terminal liquid as a continuous inter-bead layer [ref. 27].

1.2.2. Cracking During Single-pass Welding

The majority of available literature establishes mechanisms for weld cracking behavior during single pass welding. Cracks in single pass welds can be located in both the deposited weld metal and the existing base metal. The type of fracture may be divided into distinct regimes using the incipient melting point, or solidus temperature (T_S), of the weld metal as the discriminator; $T << T_S$ - cold cracking; $T < T_S$ - warm cracking; and $T > T_S$ - hot cracking.

Consequently, cold cracking applies to fracture in the solid state at temperatures approaching ambient. Likewise, warm cracking also applies to the solid state, but at temperatures just below the solidus. In contrast, hot cracking occurs in the semi-solid state at super-solidus temperatures and includes the action of highly-localized molten metal [ref. 34]. Each regime involves SGBs and the propensity for weld cracking is always influenced by interdendritic and intergranular segregation [ref. 35]. The accumulation of low-melting-point constituents in the semi-solid state can lead to the formation of low yield strength phases in the solid state. The root cause of fracture is that deposited material is unable to sustain the thermally-induced stresses generated by thermal cycling and/or static cooling.

The two most common causes of hot cracking during single-pass welding are referred to as solidification cracking (SC) and liquation cracking (LC) [ref. 36]. SC occurs at interdendritic boundaries in partially-solidified weld metal, and LC occurs at existing grain boundaries (GBs) in partially-melted base metal. Cracks form because the molten elements of predominantly-solid material are unable to accommodate shrinkage strains and thermal contraction. Activation of both mechanisms is contingent on the degree of physical constraint and the cooling rate from the welding temperature.

A common method for determining susceptibility to hot cracking, known as circular patch weld testing, is shown in figure 7 [ref. 37]. Figure 7(a) illustrates the welding of a patch into a hole in a plate, both firmly secured to an underlying fixture (figure 7(a)(i)). Of significance, the geometrical constraints are analogous to those encountered during axial deposition of a cylindrical cross-section using EBF^3. The phenomenon of hot cracking can occur by SC within the fusion zone (FZ), or by LC in the adjacent partially-melted zone (PMZ) (figure 7(a)(ii)). The PMZ resides between the FZ and the heat-affected zone (HAZ) in the base metal. The macroscopic features are easily distinguished, as presented in figure 7(b) and 7(c). SC is located within the weld bead and follows a tortuous crack path. In contrast, LC is located on the periphery of the weld bead and the curved crack path follows the weld profile.

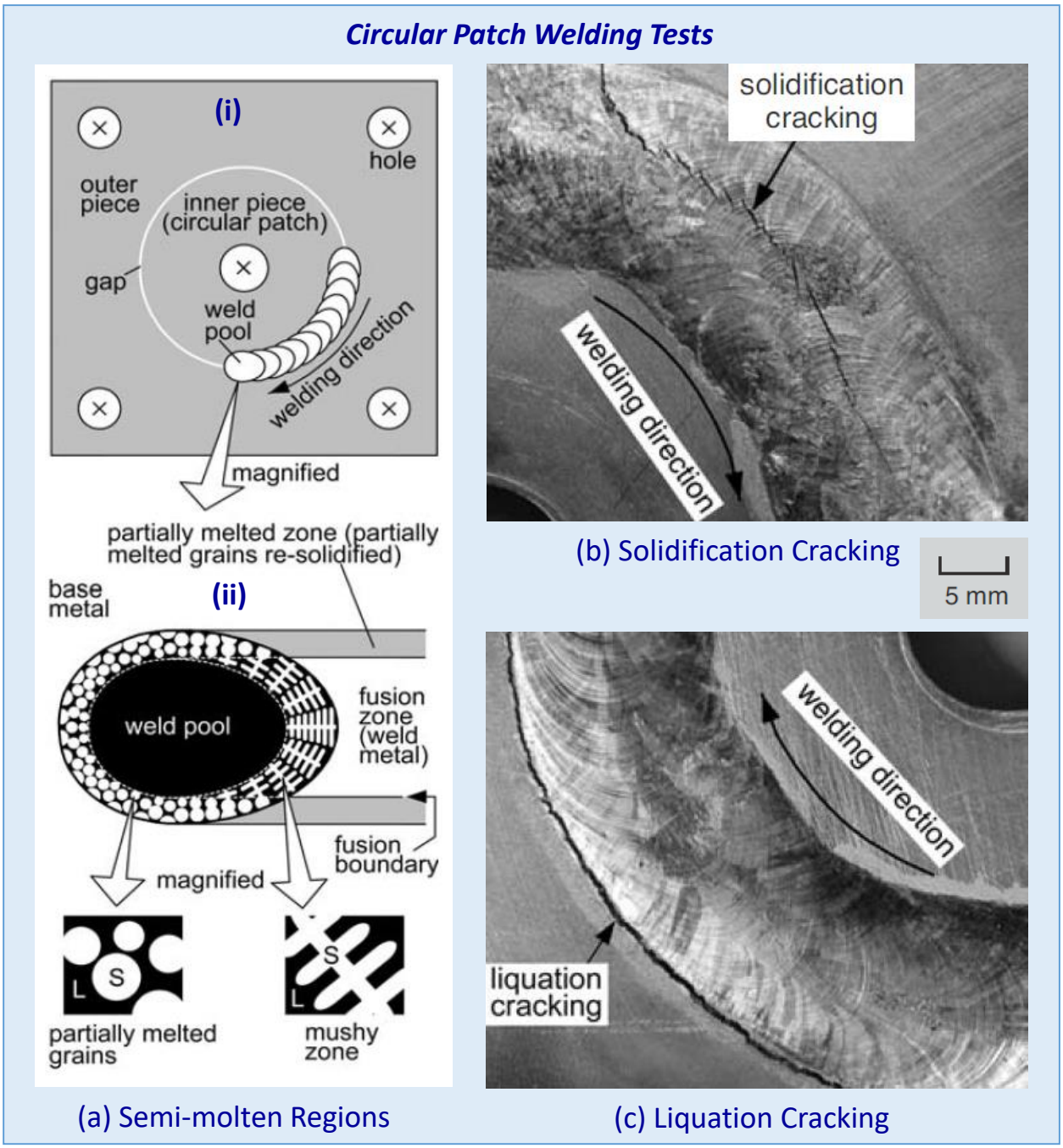

Figure 7. Circular patch welding tests: (a)(i), thermal contraction is geometrically constrained during cooling; (a)(ii), characteristics of PMZ in parent metal vs. weld metal; (b), SC occurs within weld bead; (c), LC occurs around weld bead [ref. 37].

The microscopic characteristics of intergranular fracture (IGF) by SC and LC are illustrated in figure 8 [ref. 38]. Figure 8(a) shows that SC in the FZ is associated with solute-rich, weld metal grain boundaries created by the impingement of dendrite colonies. Such interfaces are high-angle SGBs, and the resulting fracture surface exhibits uneven features that reflect the underlying dendritic morphology [refs. 36 and 39]. In contrast, figure 8(b) shows that LC in the PMZ is associated with solute-rich, pre-existing grain boundaries in the base metal. The resulting

fracture surface exhibits smooth features with facets that adhere to the grain structure beneath. In both cases, the crack surfaces tend to be decorated with a thin, solute-rich film, and coverage increases with the amount of segregation [ref. 40].

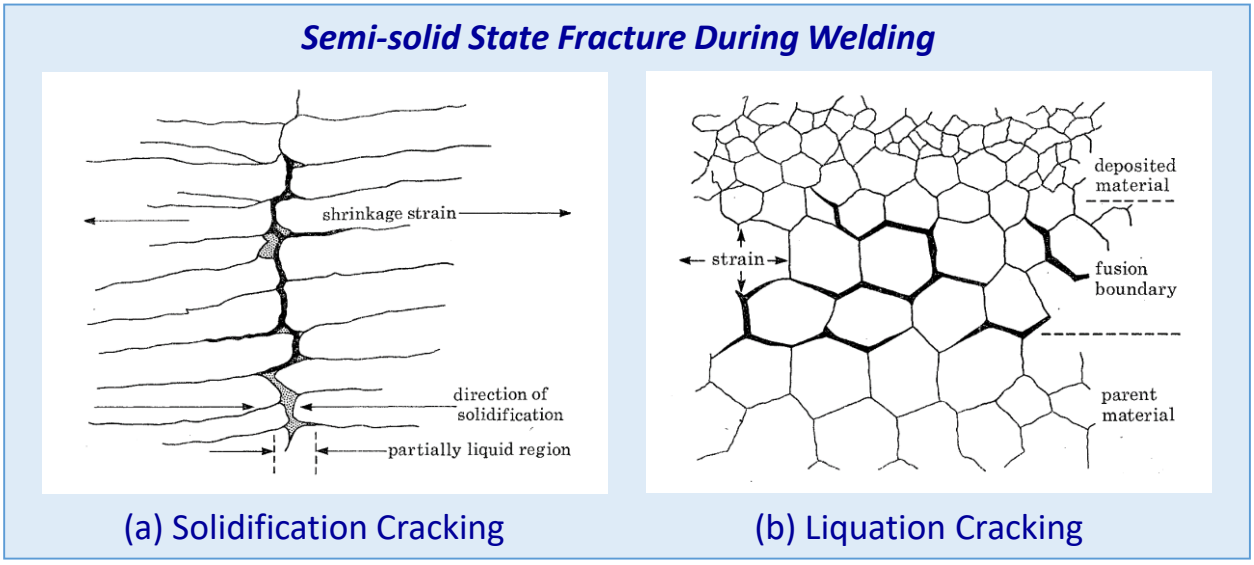

Figure 8. Hot cracking in the semi-solid state during welding: (a), solidification cracking between dendrite colonies (SGBs) within the FZ in weld metal; (b), liquation cracking at grain boundaries within the PMZ in base metal [ref. 38].

Figure 9 illustrates how the volume of terminal liquid can affect the topography of the fracture surface following hot cracking in Ni-based alloys [ref. 35]. The two examples shown relate to SC in a Ni-30Cr alloy with < 5 vol.% eutectic liquid (figure 9(a) and 9(b)) and ≈ 10 vol.% eutectic liquid (figure 9(c) and 9(d)). The key observation is that the high fraction of terminal liquid conceals the underlying dendritic structure. Creation of a continuous liquid film along SGBs can promote hot cracking by delaying the formation of solid-to-solid boundaries [ref. 36]. The resultant weakening of these boundaries with a secondary phase has implications for both semi-solid state and solid state fracture behavior.

Irrespective of the temperature regime, intergranular separation is the predominant cracking mechanism and the mode of fracture is either dimple rupture, or decohesive rupture [refs. 41and 42]. Dimple rupture is intergranular separation in the solid state that is accompanied by extensive plastic deformation and frequently classified as ductile fracture. Microvoid formation and coalescence results in a crack morphology consisting of tearing and prolific, cup-like depressions also known as “ductile dimples”.

Decohesive rupture refers to cracking through, or on the surface of, weak GB phases. Such behavior can include either semi-solid state fracture of molten material on the GBs before complete solidification, or solid state fracture of melted and re-solidified GB constituents [ref. 41]. This fracture mode has also been termed liquid-metal embrittlement (LME) in the semi-solid state because the fracture features are obscure due to immersion in a liquid [ref. 43]. The phenomenon is often referred to as yield-strength-mismatch (YSM) in the solid state and is accompanied by very limited plastic deformation [ref. 44]. The fracture behavior is frequently categorized as brittle on a macroscopic scale and ductile on a microscopic scale [ref. 42]. The crack morphology is predominantly flat and the underlying microstructural features tend to be hidden by the intergranular phase. In equiaxed grain structures, the resulting fracture surfaces

exhibit a faceted, or rock candy appearance. In dendritic microstructures, the tips of dendrites can protrude through the separated GB phase, resulting in a so-called 'eggcrate' pattern [ref. 41].

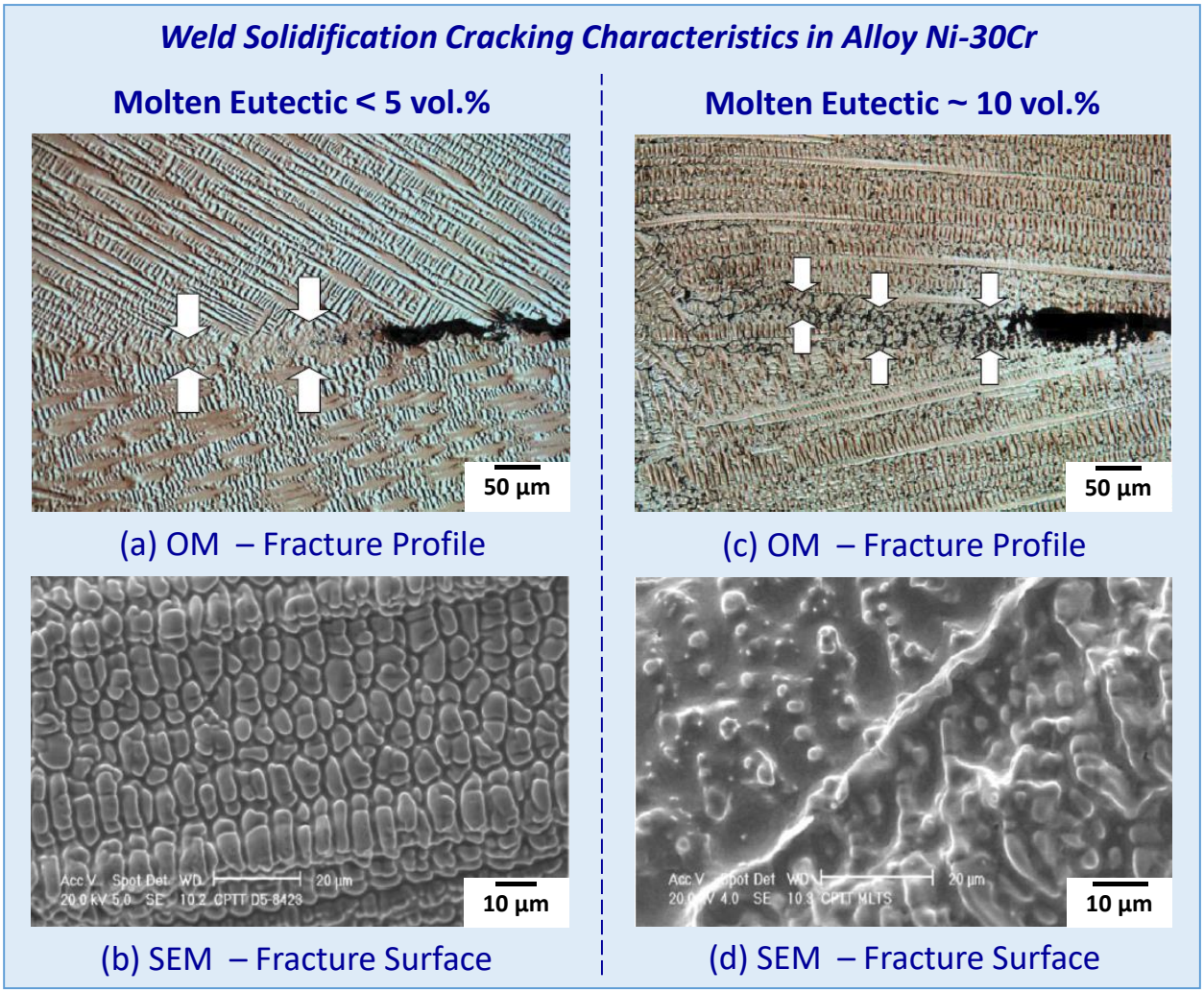

Figure 9. Dependence of fracture characteristics on volume of terminal liquid at the end of solidification. OM and SEM images: (a) & (b), < 5 vol.% molten eutectic; (c), & (d), ≈ 10 vol.% molten eutectic during welding of a NiCr30 alloy [ref. 35].

1.2.3. Cracking During Multi-pass Welding

Fracture behavior during DED/AM processes is closely aligned with a multiple pass welding scenario. In multi-pass welds, cold cracking usually refers to fast, unstable fracture at ambient temperatures. Driven by thermally-induced residual stresses, tensile overload, or 'pop-in' are traditional descriptions [ref. 45]. Warm cracking may include progressive or accelerated fracture in the form of ductility dip cracking (DDC), reheat cracking (RC), and strain age cracking (SAC) [ref. 36]. These phenomena may be in response to thermomechanical fatigue (TMF) and/or low-cycle fatigue (LCF) loading conditions caused by repetitive heating [ref. 40]. Precipitation-strengthened Ni-base alloys are highly susceptible to such high temperature, solid state fracture mechanisms as a result of intermetallic phases. In contrast, Inconel 625 is a solid solution-strengthened alloy that is not prone to DDC, RC, or SAC due to the absence of secondary phases [ref. 46].

A special category of LC, known as 'weld metal liquation cracking' (WMLC), is a hot cracking mechanism unique to multi-pass welding [ref. 47]. The principal difference between LC and WMLC is the nature of the parent grain structure. Fracture occurs in partially-melted weld metal that has been deposited during prior weld passes. In contrast with LC that occurs at pre-existing GBs in the base metal, WMLC occurs at high-angle SGBs created in the weld metal [ref. 37]. These SGBs comprise interfaces between dendrite colonies that reside within the weld beads and at inter-bead interfaces [ref. 48]. The high solute content of Ni-base alloys makes these boundaries highly-susceptible to WMLC during multi-pass welding [ref. 36]. SC, LC, and WMLC involve intergranular separation assisted by low-melting-point, solute segregation and all are sub-categories of decohesive rupture in the semi-solid state.

Although layer-by-layer AM is analogous to multi-pass welding, the highly directional heat flux associated with EBF^3 on a substrate does create a unique situation [ref. 33]. In the absence of convection and with limited radiation, dendritic growth aligns with the build direction. Weld cracking tends to be confined to boundaries created within the heavily-aligned microstructure during solidification. WMLC has been observed in monolithic Inconel 718 following both EB welding [ref. 49] and laser beam AM [ref. 15]. The grain structure comprises an array of dendrite colonies oriented in close proximity with the build direction. Interdendritic terminal liquid tends to be forced to colony extremities as solidification advances. Terminal liquid that migrates in the build direction tends to promote segregation at interlayer boundaries.

1.2.4. Welding of Inconel 625 to GRCop-84

Alloy mixing between Inconel 625 and GRCop-84 in the first few deposited layers will govern the incipient melting point and the secondary phases formed. The extent of Cu migration from the substrate into the deposited material will determine the gradient in T_s. Cr, Nb and Mo have approximate maximum solubilities of 30, 8, and 1.3 wt.% in liquid Cu, but only 0.7, 1.3, and 0 wt.% in solid Cu, respectively [ref. 50]. It is also worth noting that binary intermetallic phases between Cu and Ni, Cr, Mo, or Nb are non-existent [ref. 13]. In contrast, Cu and Ni exhibit complete miscibility in both the liquid and solid state, and create a continuous series of cupronickel solid solutions. Consequently, the Ni content of any Cu-rich segregation will govern T_s of the terminal liquid and the non-equilibrium STR within the alloy transition zone.

During single pass welding, alloy mixing can widen the STR, enlarge the PMZ, and exacerbate weld cracking [ref. 30]. The susceptibility to semi-solid state fracture is influenced by the volume/longevity of terminal liquid, and solid state fracture by the amount/distribution of secondary phases [ref. 51]. In both cases, weld cracking is promoted the most by the presence of interdendritic and/or intergranular segregation. During multi-pass welding, the effect is compounded by the addition of inter-bead and/or inter-layer segregation. The broader STR in a multi-alloy deposit will also magnify the associated solidification shrinkage strains generated in the semi-solid state [ref. 52].

Solute mixing of Inconel 625 with GRCop-84 will likely cause the formation cupronickel phases at interfaces in the alloy transition zone. Differences in the intrinsic material properties between the parent alloys and varying blends of the two will also exert an influence on semi-solid and solid state fracture. The most relevant properties of Inconel 625, GRCop-84, and a selection of cupronickel alloys are summarized in table 1. Variations in the mechanical properties of microstructural constituents will govern the mechanical behavior of the deposit in the mixed solute region. The important physical property that must be considered is differential thermal

contraction between the deposited and substrate materials. As illustrated in figure 10, the differential in the coefficient of thermal expansion (CTE) will create tensile residual stresses between Inconel 625 and GRCop-84 at any process temperature [refs. 56, 57, and 58].

Table 1. Physical and mechanical properties of materials relevant to this study; Inconel 625, GRCop-84, and projected blends of the two alloys in the transition zone of the build. Note that cupronickel phases comprise a continuous series of solid solutions due to total miscibility.

ALLOY	Condition or Designation	Solidification Temperature Range		Coefficient of Thermal Expansion	Tensile Properties @ 20°C			Refs.
		$T_{Solidus}$ °C	$T_{Liquidus}$ °C	20-300°C 10^{-6}/°C	σ_{UTS} MPa	σ_{YS} MPa	El. %	
Inconel 625	Casting N06625	1290	1350	13.3	710	350	48	*53*
	Powder Fed/ Electron Beam Deposited				750	410	44	*19*
	Laser Beam Sintered Powder				744	485	43	*18*
	Wire fed/ Arc Plasma Deposited				721	438	49	*20*
GRCop-84	Laser Beam Sintered Powder	1077	1083	16.3	482	279	18	*23*
Cr_2Nb Phase	*Intermetallic Dispersoid*	*1770*		---	---	*1200*	---	*54*
High Purity Cu	Casting C81100	1065	1083	16.9	170	62	40	*50*
CuNi10	Casting C96200	1100	1150	16.2	310	170	20	*50*
	Casting C70600				280	120	20	*55*
CuNi20	Casting C96300	1140	1200	15.8	---	---	---	*50*
	Casting C71000				---	---	---	
CuNi30	Casting C96400	1170	1240	15.4	470	255	28	*50*
	Casting C71500				340	120	18	*55*

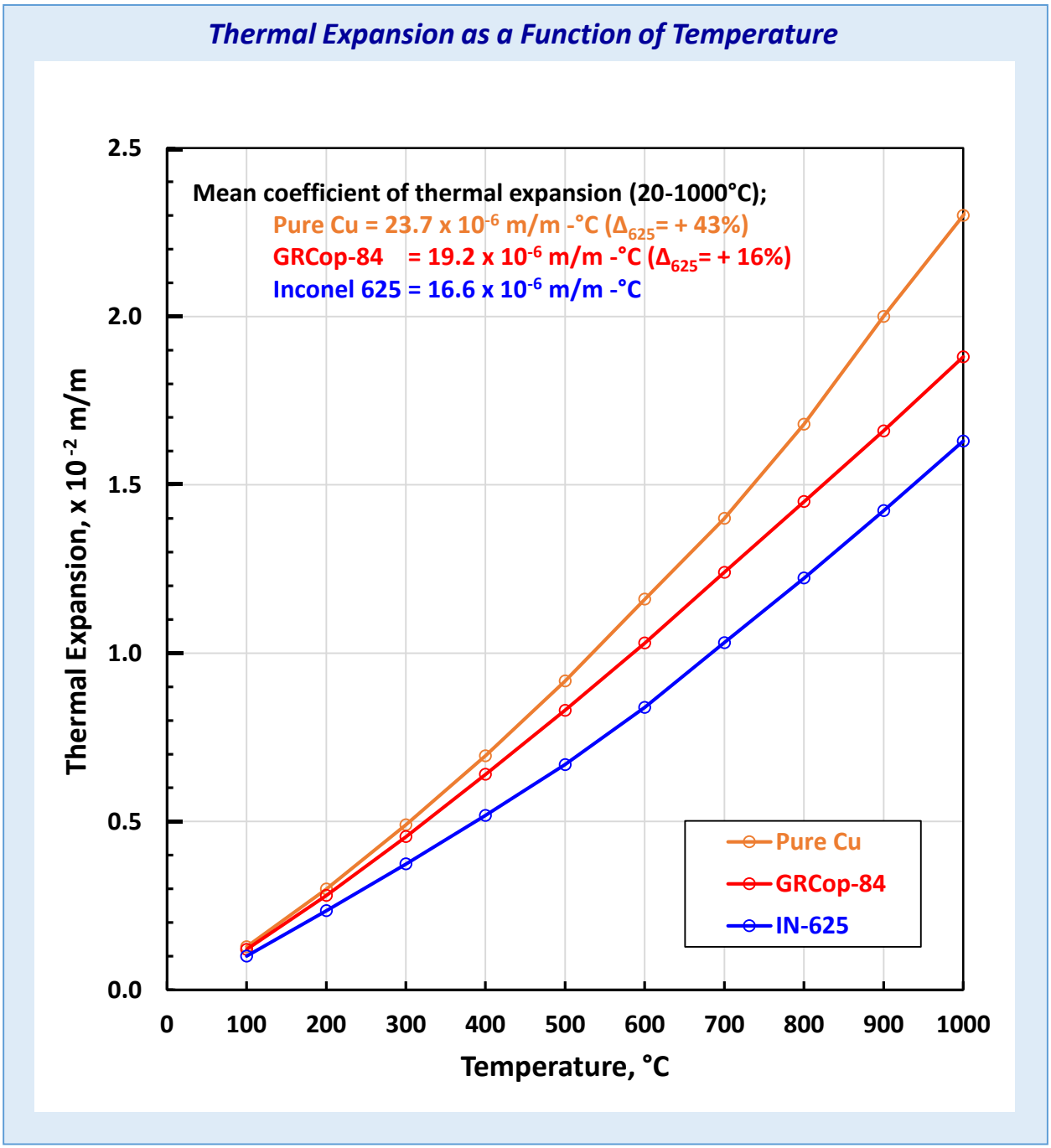

Figure 10. Effect of temperature on thermal expansion of pure Cu and GRCop-84 with respect to Inconel 625 [refs. 56, 57, and 58]. Note that thermal contraction of the substrate will be greater than the build over the entire solid-state temperature regime.

2. Experimental Procedures

2.1. EBF^3 Deposition Trials

The main purpose of this project was to generate test coupon material suitable for evaluating the tensile properties of the Inconel 625/GRCop-84 interface. The original goal was to employ the same processing conditions used for manufacturing the rocket engine component. Unexpectedly, deposition of the first ring section had to be aborted when cracking was detected in the vicinity of the substrate/build interface. It was suspected that excessive residual stresses created during deposition were responsible for the premature failure. The ensuing parametric study, designed to alleviate the problem, consisted of a series of ten EBF^3 trials. The experimental philosophy adopted was to increase the average bulk temperature in order to reduce the effects of differential thermal contraction between the substrate and build materials.

A key objective was to adjust the average bulk temperature while maintaining a layer height and penetration (re-melt) depth comparable with the rocket engine component. The individual trials involved permutations of the following primary process variables; beam power, travel speed (beam translation), wire feed rate, and substrate temperature. Fine tuning of secondary process variables such as beam focus, bead spacing and bead height was also included to control deposit geometry. The development of circumferential cracks in the vicinity of the substrate/build interface either during or after deposition persisted in every ring section manufactured. Consequently, mechanical testing was forestalled and a failure investigation initiated.

Two ring sections from the EBF^3 trials were selected for analysis, hereafter referred to as Ring 1 and Ring 4. The processing conditions best bracketed the range of substrate temperatures employed in the parametric study. For Ring 1 at the lower limit, the processing conditions for the axial build duplicated those employed for the radial build of the rocket engine component. For Ring 4 at the upper limit, the primary process variables were all increased by a factor of approximately two for the majority of the layers. The premise was that increasing the substrate temperature would lower the temperature gradient across the substrate/build interface, thereby reducing the residual stresses generated.

Both Ring 1 and Ring 4 started with the same parameters for deposition of the initial Inconel 625 layer onto the GRCop-84 substrate. Prior to depositing the first layer, the substrate was pre-heated using the EB (without wire) at a reduced power level. The target temperature was in the range 200-250°C, already proven to facilitate metallurgical bonding of Inconel 625 to GRCop-84. During deposition of the subsequent layers, the substrate temperature was restricted to $T_{Sub} \leq$ 250°C for Ring 1, and maintained at T_{Sub} = 400-550°C for Ring 4. The temperature was monitored using a thermocouple in contact with the rotating GRCop-84 substrate at a distance of $\approx$ 12.5 mm below the substrate/build interface.

Each bead was deposited individually and the process was momentarily suspended after each complete rotation. During the pause, the beam was repositioned via a step function that permitted a $\approx$ 50% overlap between consecutive beads. Each layer consisted of seven, evenly spaced beads with the deposition sequence starting at the inner wall and progressively advancing toward the outer wall. As indicated earlier, the EBF^3 system had no provision for active cooling, so the time interval between layers was used to control the substrate temperature. For Ring 1 and Ring 4, the deposition parameters were pre-set and each bead in a given 7-bead layer was deposited in immediate succession (B1 through B7). After B7 was deposited, the EB gun/wire feeder assembly was re-positioned to the B1 location for the next layer, but the process was

interrupted until the substrate temperature was within the prescribed range. This operating protocol resulted in longer beam-off pauses and larger thermal cycles between layers during deposition of Ring 1 than Ring 4.

Heat accumulated rapidly during deposition due to the limited conduction through the substrate. In the case of Ring 1, the intervals progressively increased with build height to allow time for the heat to dissipate before starting the next layer. The temperature continuously increased with repeated deposition cycles such that the pause between the first and second layer was on the order of 5 minutes. However, the time intervals often exceeded 10 minutes with subsequent layers. In the case of Ring 4, successive layers were deposited immediately after completion of the prior layer. This was necessary in order to maintain the higher substrate temperature, particularly during deposition of the first few layers.

2.2. Failure Investigation

The Ring 1 and Ring 4 trial deposits that were the focus of the failure investigation are presented in figure 11(a) and 11(b). Both ring sections have an outside diameter of ≈ 152 mm and a wall thickness of ≈ 19 mm. Ring 1 has a build height of ≈ 36 mm owing to the deposition trial being aborted when cracking was detected. In contrast, Ring 4 is ≈ 66 mm tall because the trial progressed to the scheduled height. Cracking was detected after an extended period of post-deposition cooling. Figure 11(c) and 11(d) show Ring 1 and Ring 4 sectioned for metallurgical analyses, with the bulk of the substrate removed. The cracks navigate the full circumference of the outer wall, but do not penetrate to the inner wall. Specimens compatible with evaluating macrostructure, microstructure, bulk composition, solute gradient/distribution, and fracture characteristics were subsequently extracted.

Specimens for metallurgical analyses were prepared using traditional methods and standard characterization techniques were applied [refs. 59and 60]. Metallographic practices developed for Ni-base superalloys proved compatible with the present Inconel 625/GRCop-84 combination. During scanning electron microscopy (SEM) studies, specimens were evaluated in the as-polished condition, i.e. un-etched. Solute gradients were quantified using energy dispersive spectroscopy (EDS) and compositional mapping established solute distribution. Backscattered electron (BSE) imaging was used for qualitative compositional analysis (compo mode). Secondary electron (SE) imaging was used for microstructural/fractographic analyses (topo mode).

During examination by optical metallography (OM), color tint etching methods were selected to highlight macrostructural and microstructural characteristics [refs. 61and 62]. Empirical studies revealed that electrolytic chromic acid was the best macro-etchant and Lucas reagent was the best micro-etchant. Chromic acid macro-etching comprised 50 g chromium III oxide (CrO_3), 500 ml distilled water, and electrolytic, RT, 6V, 10-30 sec. Lucas reagent micro-etching comprised 150 ml hydrochloric acid (HCl), 50 ml lactic acid ($C_3H_6O_3$), 3 g oxalic acid ($C_2H_4O_4$), and electrolytic, RT, 2V, 10-20 sec. OM images were collected using cross-polarized illumination and electronically stitched together to form microstructural montages.

Figure 11. Circumferential cracking (⇨) during axial deposition of Inconel 625 onto GRCop-84 via EBF3; (a), Ring 1 build; (b), Ring 4 build; (c), Ring 1 sectioned; (d), Ring 4 sectioned.

2.3. Metallurgical Characterization

For reference, the nominal composition of Inconel 625 is Ni-22.3Cr-8.7Mo-3.7Nb (wt.%) and that of GRCop-84 is Cu-6.5Cr-5.6Nb (wt.%). The measured compositions of the wire and powder feedstock, as provided by the vendors, are listed in table 2 [refs. 63and 64]. The powder was consolidated into the hollow, cylindrical substrate material via SLM methods and supplied

to LaRC [ref. 1]. Subsequent metallurgical analyses were divided into discrete tasks, each with a specific objective:

- **Assess the macrostructural characteristics by identifying the individual deposited layers with respect to the fracture location in each build.** These macrographs were employed as a roadmap during quantification of the transitions in microstructure and composition between the deposited and substrate materials.
- **Establish the microstructural characteristics of the two ring sections in the vicinity of the substrate/build interface.** OM was employed to analyze the prevailing grain/dendritic structure and establish the mode of solidification. Studies included correlating processing conditions with changes in the microstructural transition between the dissimilar materials.
- **Evaluate the extent of alloy mixing in the transition zone on a macroscopic level.** Wet chemistry analyses were conducted on a series of three, 2 mm-thick sections extracted from the first 8 mm of each build. The goal was to ensure that micro-chemical analysis data taken from the same regions were truly representative of the bulk material.
- **Determine the solute gradient and distribution in the transition zone on a microscopic level.** SEM/EDS was used for qualitative and quantitative analyses of the compositional variations within the alloy mixing zone. The goal was to isolate any differences adjacent to the fracture locations in the two ring sections.
- **Characterize the fracture behavior, by correlating crack morphology with microstructure through the cross-section in each build.** The characteristics of a typical fracture surface were revealed by macroscopic examination and microscopic details were revealed via conventional SEM fractography.

2.4. Metallurgical Analysis Roadmaps

The microstructural characteristics resulting from layer-by-layer AM of monolithic materials exhibit periodicity. Features depend upon individual bead morphology and the geometry of the rows of beads. In this case, the first few deposited layers also constitute a transition region when the deposit and substrate comprise dissimilar materials. The influence of alloy mixing within this region diminishes with build height, resulting in the superposition of microstructural and compositional gradients. Employing a variety of analytical techniques on a progressively finer scale is necessary to fully evaluate these characteristics. Therefore, establishing the exact locations of the metallurgical analyses performed is critical for integration of the different types of data. The ‘roadmaps’ presented in figure 12 and figure 13 serve this purpose for the transition region in Ring 1 and Ring 4, respectively.

The OM micrographs in figure 12(a) and figure 13(a) show the areas analyzed to establish the overall microstructural characteristics in the first four layers and the arrangement of the interlayer boundaries. The OM macrographs in figure 12(b) and figure 13(b) show the areas analyzed to determine the overall compositional gradient in the first four layers, with the locations of the interlayer boundaries identified. The BSE(compo) images in figure 12(c) and figure 13(c) show the areas analyzed surrounding the site of crack origination at the outer wall of the build, with the locations of the adjacent layers identified. The BSE(compo) images in figure 12(d) and figure 13(d) show the areas analyzed along the path of crack progression through the

build cross-section, with the series of individual beads identified. These particular micrographs aid in interpretation of location-dependent features during the subsequent fractographic analyses.

Table 2. Measured compositions of the starting feedstock as provided by the vendors [refs. 63and 64]; Inconel 625 wire for the EBF3 system and GRCop-84 powder for the SLM system.

Inconel 625 Wire (wt.%)				GRCop-84 Powder (wt.%)			
Element	Specification		Meas.	Element	Specification		Meas.
	Min.	Max.			Min.	Max.	
Ni	Balance		64.7	Cu	Balance		87.9
Cr	20.0	23.0	22.3	Cr	6.2	6.8	6.45
Mo	8.0	10.0	8.7	Nb	5.4	6.0	5.61
Nb	3.15	4.15	3.67	Fe		0.02	<0.004
Fe		5.0	0.13	O		0.07	0.058
Co		1.0	0.03	C			0.002
Mn		0.5	0.03	N			<0.001
Si		0.5	0.053				
Al		0.4	0.13				
Ti		0.4	0.23				
C		0.1	0.01				
Ta			0.002				
Cu			0.003				
Source	Arcos Industries, LLC Lot# AP9902, Heat# QQ106			Source	ATI Metals Corporation Melt# 522-405		

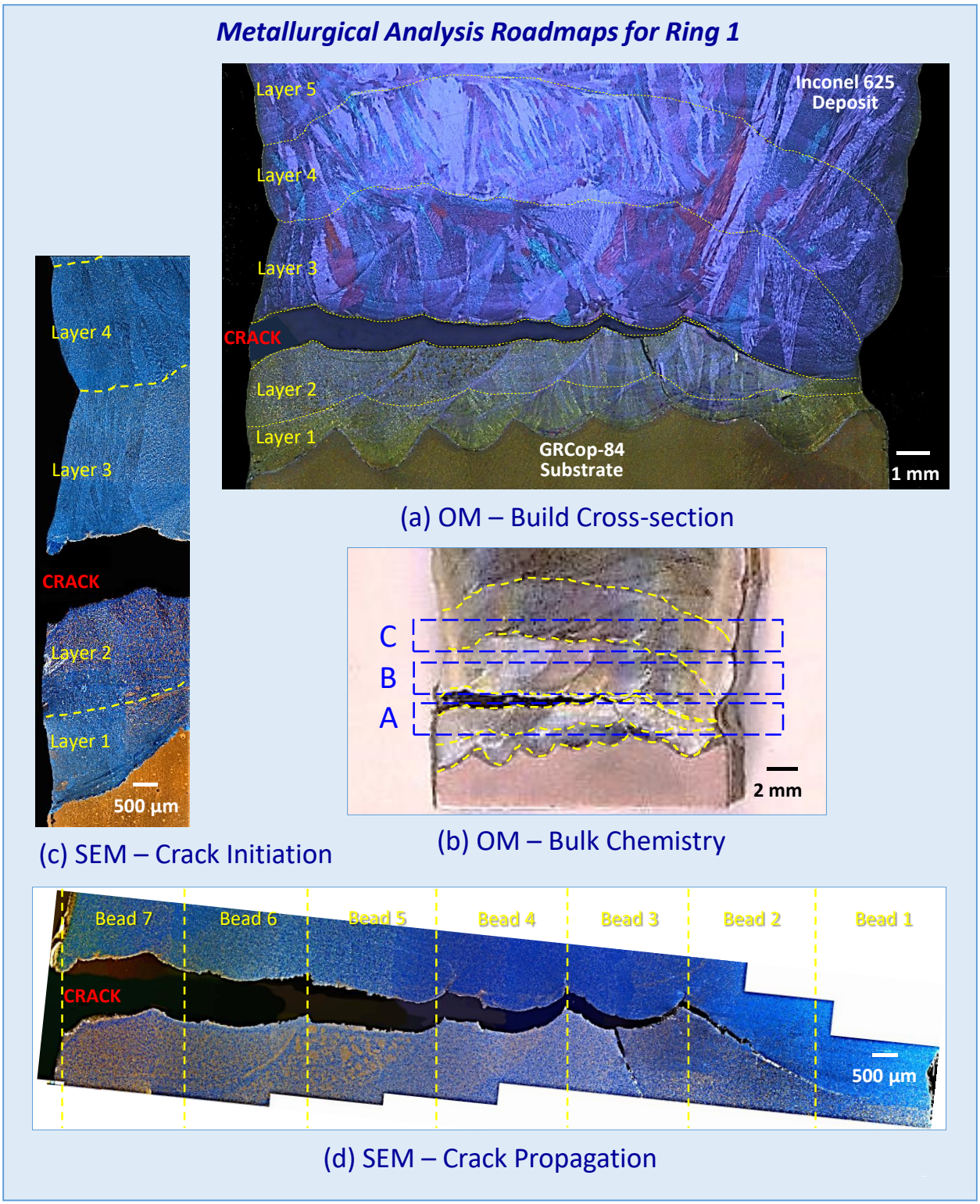

Figure 12. Metallurgical analysis roadmaps for Ring 1; (a), OM micrograph – microstructural characteristics; (b), OM macrograph – bulk chemistry; (c), BSE(compo) image – crack formation at the outer wall; (d), BSE(compo) image – crack opening through the build cross-section.

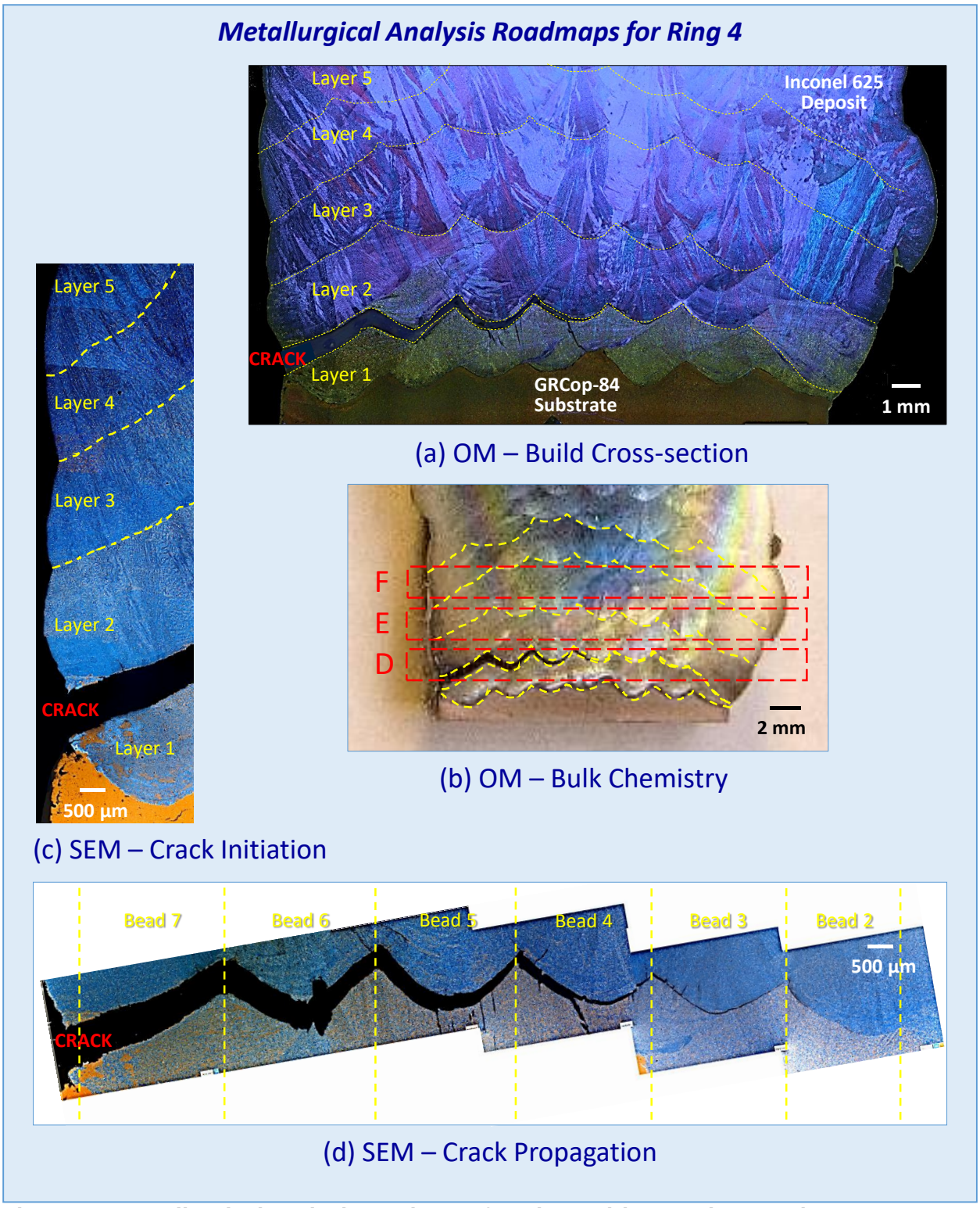

Figure 13. Metallurgical analysis roadmaps for Ring 4; (a), OM micrograph – microstructural characteristics; (b), OM macrograph – bulk chemistry; (c), BSE(compo) image – crack formation at the outer wall; (d), BSE(compo) image – crack opening through the build cross-section.

3. Results

3.1. Macrostructural Characteristics

Macrosections of the Inconel 625 deposits on the GRCop-84 substrates are presented in figure 14. The viewing orientation, nomenclature adopted, and deposition sequence are documented in figure 14(a) for Ring 1. Each layer consists of seven beads with the first bead deposited at the inner wall and the last bead deposited at the outer wall. Macrographs representative of Ring 1 and Ring 4, prepared using electrolytic chromic acid reagent, are shown in figure 14(b) and 14(c). In both sections, the deposited layers exhibit a crown-shaped profile through the thickness. The layers are of comparable, uniform height at the center (≈ 2 mm) and taper in thickness toward both walls. The individual beads have a more scalloped appearance in the mid-section of Ring 4 than in Ring 1. Of most significance, failure did not occur at the substrate/build interface in either build. The evidence indicates that the circumferential cracks formed between deposited layers in both ring sections.

The macrostructural characteristics of the first ten layers of both ring sections are revealed in more detail in figure 15. The cross-sections of Ring 1 and Ring 4 are shown in figure 15(a) and 15(b). A comparison reveals that the bead morphology differs between the builds, appearing asymmetric in Ring 1 and symmetric in Ring 4. The aspect ratio (width/depth) of the individual beads is also larger in Ring 4 than Ring 1, which may be a reflection of the higher bulk temperature. In both builds, the interlayer crack profile appears to mimic the shape of the underlying beads. As a result, the crack morphology may be described as planar in Ring 1 and serrated in Ring 4. An important function of these images is to map the layers of beads with respect to the crack location in each build. Of most significance, the cracks reside between L2 and L3 in Ring 1, but between L1 and L2 in Ring 4. It is also evident that the crack opening is wider and that cracking extends further through the wall thickness in Ring 1 than Ring 4.

3.2. Microstructural Characteristics

The overall microstructural characteristics of Ring 1 are displayed in figure 16(a). The most striking feature is that the solidification microstructure above and below the crack exhibits different characteristics. Above the crack, the layers of the Inconel 625 are dominated by a cellular dendritic structure that appears heterogeneous. The dendrite colonies are of different shapes and sizes with isolated examples extending across multiple layers. The colonies are oriented in close proximity with the build direction, the variance tending to be larger toward the free surfaces. Below the crack, it is difficult to discern the microstructural features, i.e. in L1 and L2. The differential etching response may be a result of the close proximity to the substrate and increased Cu content. The locations of the seven beads making up each layer are visible and there is evidence of a dendritic structure in some of the beads. The profile of the substrate/build interface clearly reflects deposition of the individual beads contained in each layer, which were deposited from right to left. The primary crack path is confined to the L2/L3 boundary and extends through greater than 90% of the cross-section. There is also evidence of secondary cracks extending through L1 and L2 towards the substrate/build interface.

The overall microstructural characteristics of Ring 4 are displayed in figure 16(b). Again, the difference in the features of the solidification microstructure above and below the crack is the most striking feature. Above the crack, a more homogeneous dendritic structure predominates and the cellular dendrites appear less fragmented than in Ring 1. The dendritic colonies tend to be oriented normal to the interlayer boundaries and follow the crowned shape of the deposited

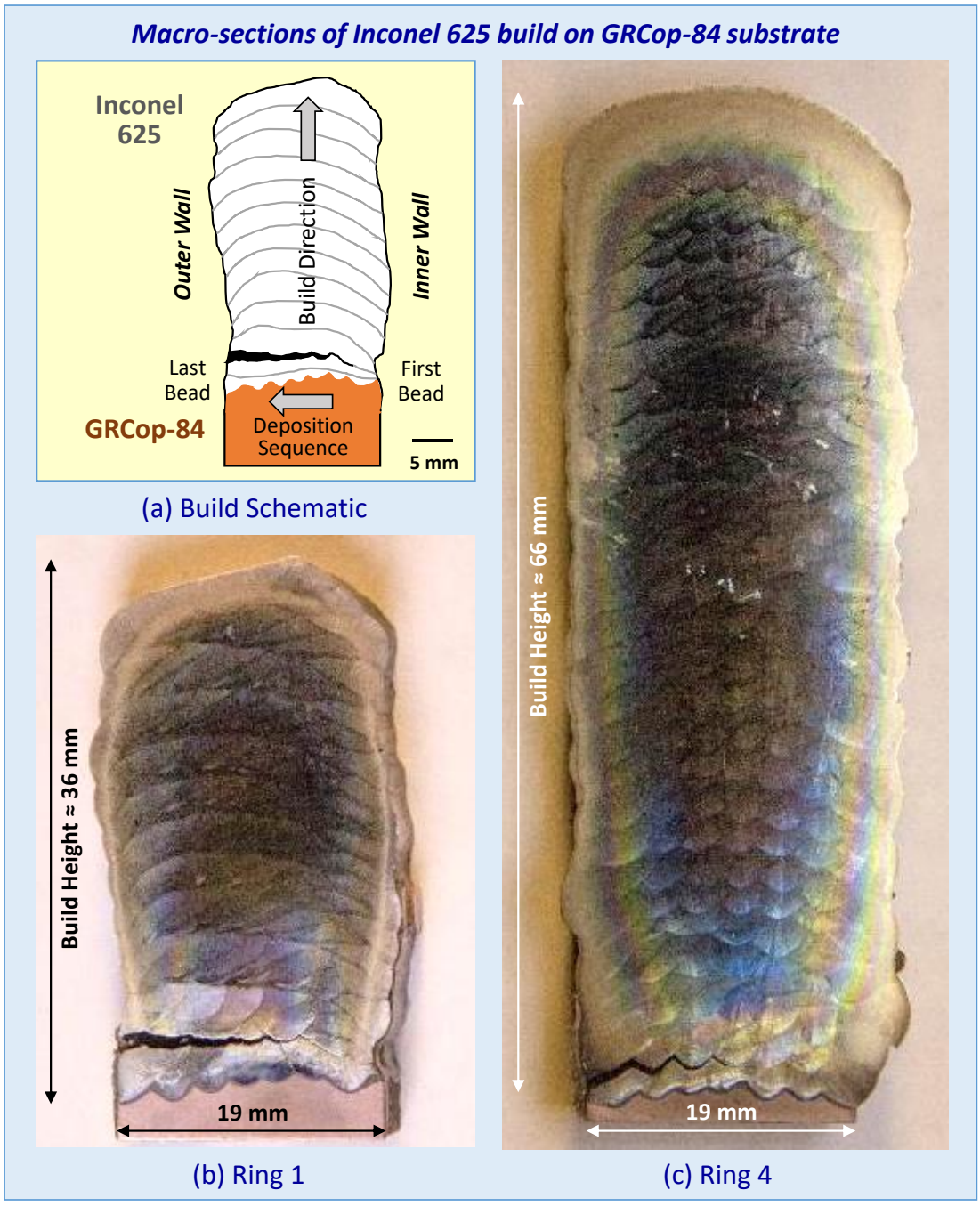

Figure 14. Representative macrosections of Inconel 625 deposited on GRCop-84 substrate; (a), schematic illustrating nomenclature adopted; (b), Ring 1 (build height ≈ 36 mm); (c), Ring 4 (build height ≈ 66 mm).

layers. The individual beads are more visible and the dendrite inclination appears to be affected by the change in bead morphology. The profile of the interlayer boundaries has transitioned from being almost planar to more serrated in appearance. Below the crack, L1 in Ring4 appears similar to L1 and L2 in Ring 1, again a consequence of differential etching response. It remains difficult to discern the microstructural features, but there is still evidence of a dendritic structure within isolated beads. The profile of the substrate/build interface again mimics the shape of the

series of beads making up each layer, deposited from right to left. The primary crack path is confined to the L1/L2 boundary and extends through ≈ 80% of the cross-section. There is also evidence of multiple secondary cracks extending through L1 towards the GRCop-84 substrate.

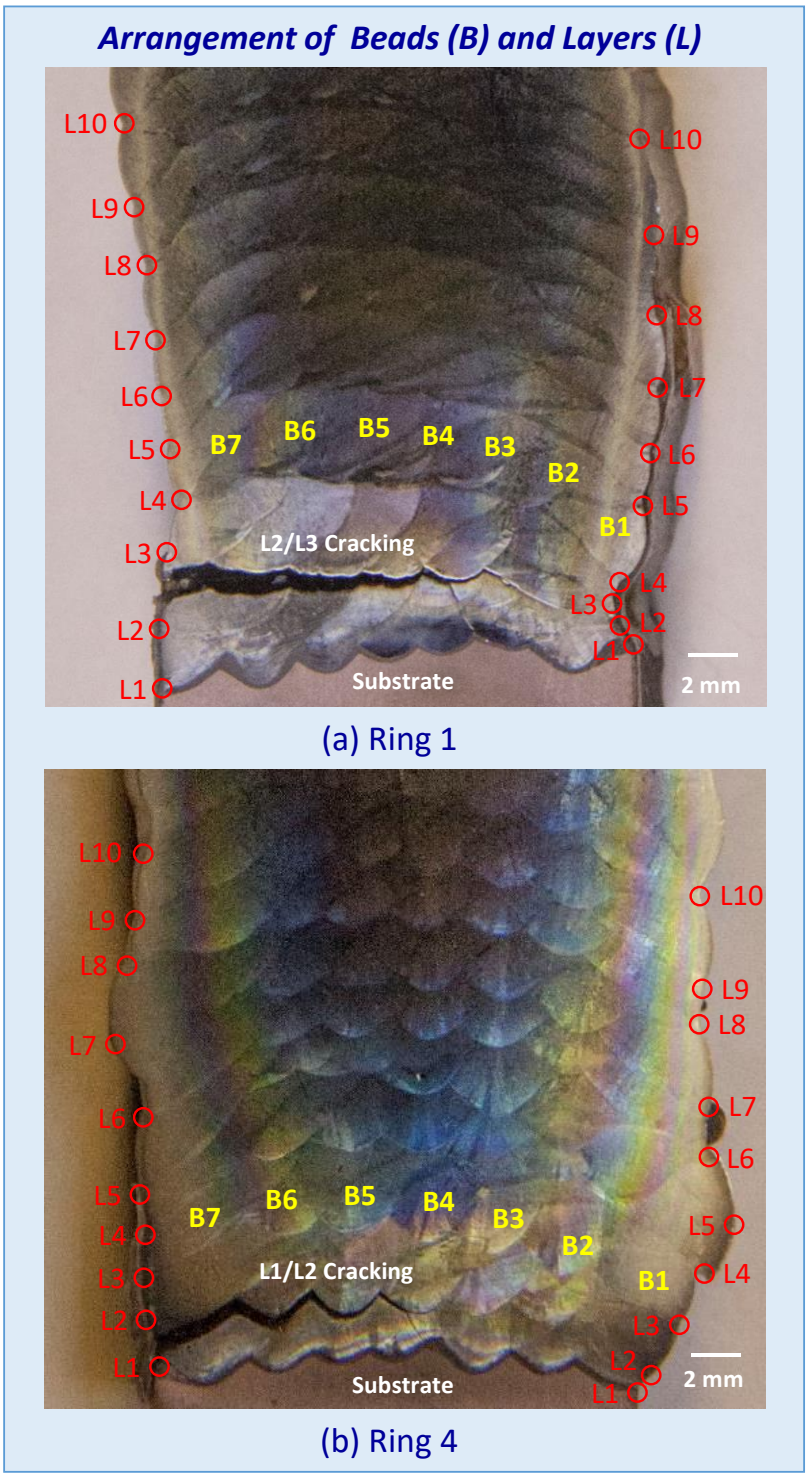

Figure 15. OM macrographs highlighting the first ten deposited layers in each build; (a), Ring 1; (b), Ring 4. The distribution of beads within a layer, the arrangement of the layers, and the location of the crack are identified.

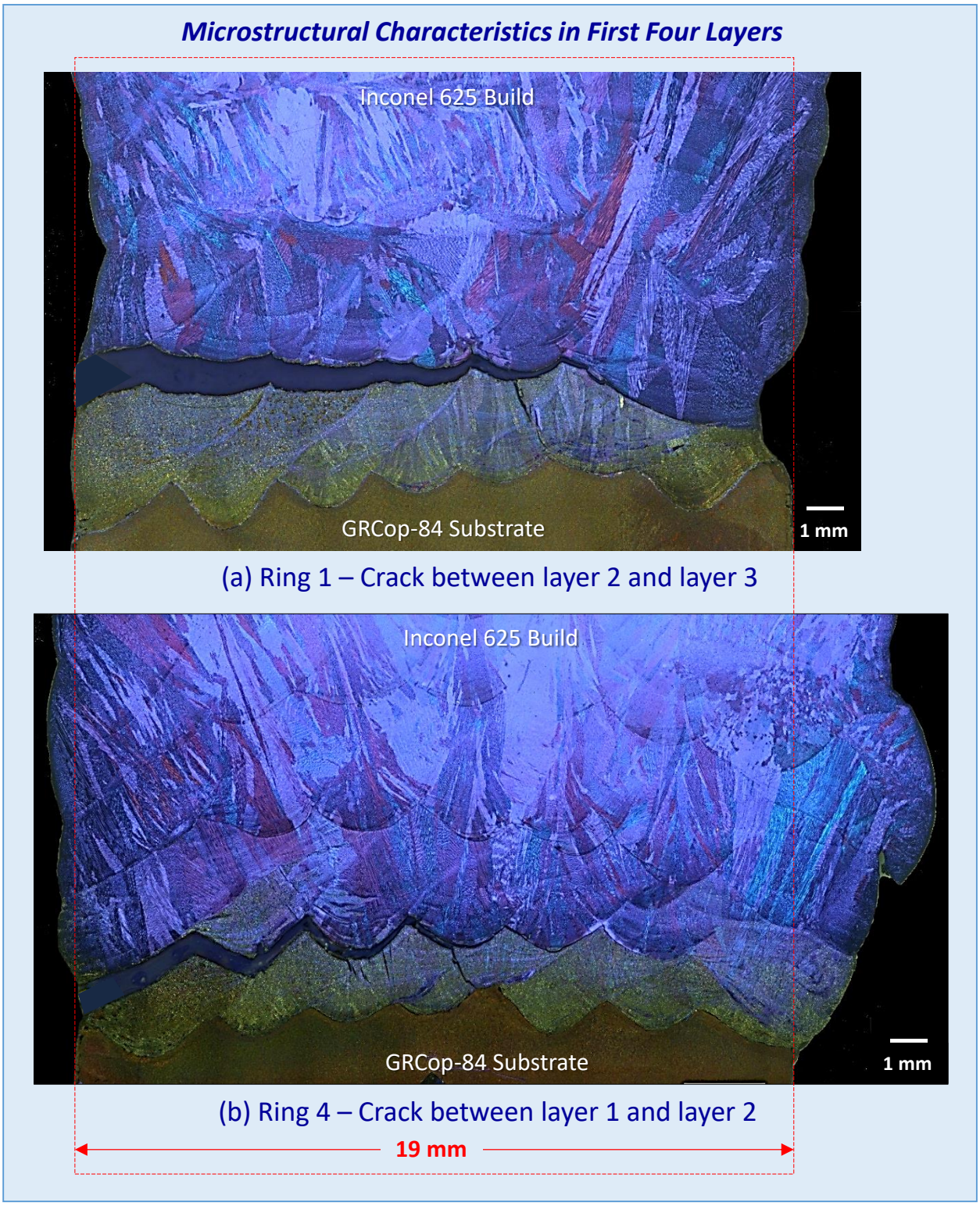

Figure 16. Metallographic cross-sections documenting the cellular dendritic microstructure within the first four layers; (a), Ring 1; (b), Ring 4. The crack follows the L2/L3 and L1/L2 interlayer boundary, respectively.

Detailed views representative of the interlayer boundaries separating the first four layers (L1 to L4), and include the substrate/build interface (Sub/L1), are shown in figure 17. The L3/L4, L2/L3, L1/L2 boundaries, and the Sub/L1 interface are compared in figure 17(a)(i-iv) for Ring 1. Fabricated at the lower bulk temperature, cracking occurred during deposition between L2 and L3, i.e. along the L2/L3 boundary shown in figure 17(a)(ii). The image reveals evidence of a distinct microstructural discontinuity across this interlayer boundary. The characteristics adjacent to the upper crack surface are consistent with the bulk of the deposit, i.e. the solidification microstructure of monolithic Inconel 625. The characteristics adjacent to the lower crack surface are consistent with a transition, i.e. an indistinct dendritic structure caused by solute blending of Inconel 625 with GRCop-84. Of significance, there is no evidence of dendrite bridging or epitaxial growth between L2 and L3. Above the crack, figure 17(a)(i) reveals epitaxial growth of dendrite colonies across the L3/L4 boundary. Below the crack, figure 17(a)(iii) reveals microstructural continuity across the L1/L2 boundary, even though dendritic features are indistinct. Although figure 17(a)(iv) reveals a distinct joint between the dissimilar materials at the Sub/L1 interface, the bond line appears metallurgically sound.

The L3/L4, L2/L3, L1/L2 boundaries, and the Sub/L1 interface are compared in figure 17(b)(i-iv) for Ring 4. Fabricated at the higher bulk temperature, cracking occurred following deposition between L1 and L2 in Ring 4, i.e. along the L1/L2 boundary shown in figure 17(b)(iii). Again, the image shows the presence of a microstructural discontinuity. The dendritic features adjacent to the upper crack surface are consistent with solidification of a monolithic alloy. The microstructural features adjacent to the lower crack surface are suggestive of considerable alloy mixing. The dendritic structure is masked as a result of migration of solute from the substrate into the deposit. Similarly, there is no evidence of epitaxial growth or dendrite bridging across the boundary. Above the crack, figure 17(b)(i) and (ii) reveal epitaxial growth of dendrite colonies across the L3/L4 and L2/L3 boundaries. Below the crack, the features of the Inconel 625/GRCop-84 joint in figure 17(b)(iv) suggest good adhesion at the Sub/L1 interface.

The inability of OM to resolve the features in the layer(s) below the cracks prompted a closer examination using SEM/BSE(compo) imaging, as shown in figure 18. A representative area containing the substrate, L1 and L2 in Ring 1 is shown in figure 18(a). A dendritic structure is evident throughout the initial layers of the build, with dendrite colonies of comparable dimensions in each layer. However, figure 18(b) does suggest that the dendrites in L1 become finer approaching the interface with the substrate. The image also reveals evidence of secondary phase formation at the Sub/L1 interface. Of most significance, figure 18(c) reveals little change in dendrite orientation across the L1/L2 boundary, consistent with an epitaxial relationship. The objective of this series of images is to identify any microstructural reason for the differing fracture location during the two EBF^3 trials. It may be concluded that cracking in both deposits coincides with an isolated, interlayer boundary exhibiting a lack of epitaxy, i.e. L2/L3 in figure 17(a)(ii) for Ring 1, and L1/L2 in figure 17(b)(iii) for Ring 4.

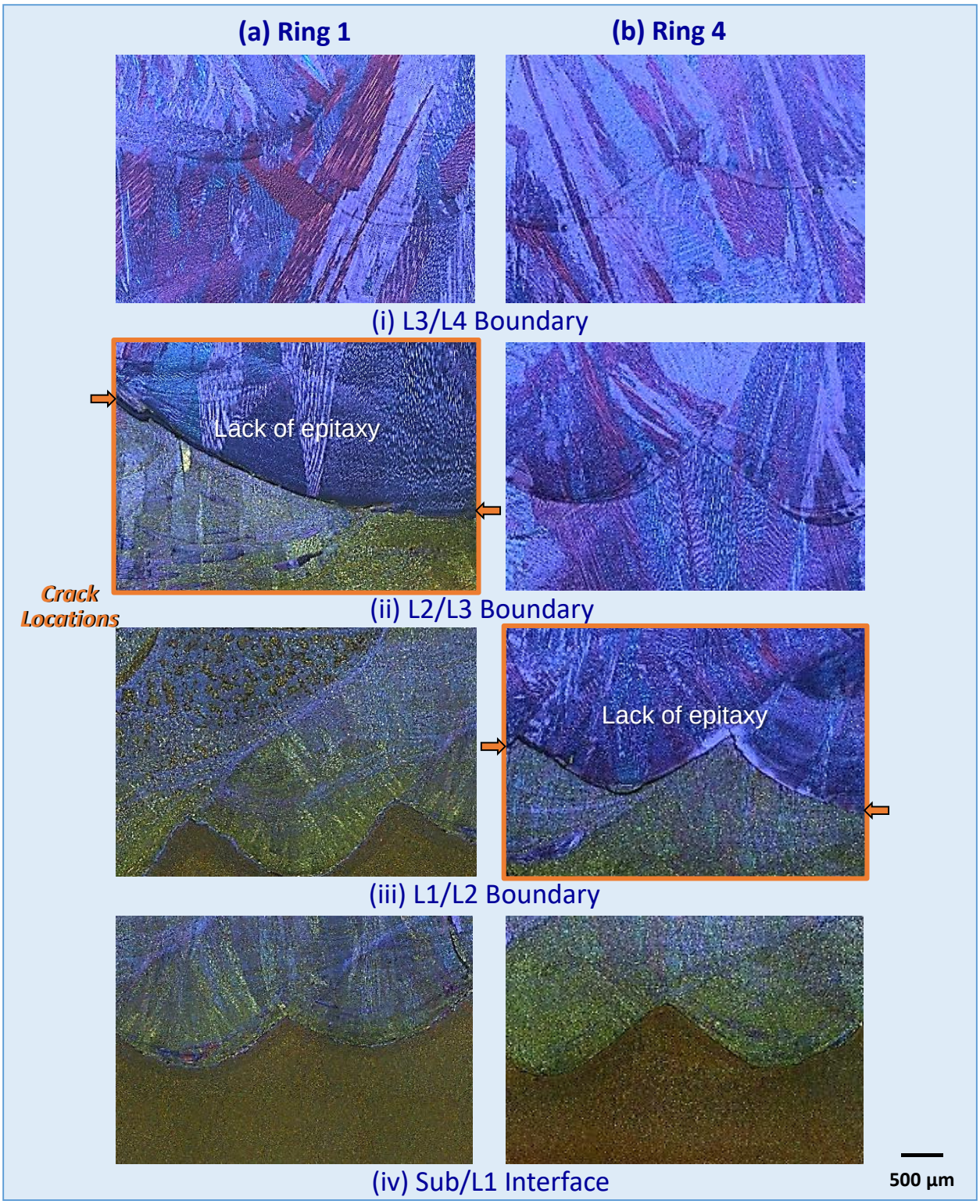

Figure 17. Representative OM images of boundaries separating the first 4 deposited layers; (a), Ring 1; (b), Ring 4. In each case, the interlayer boundaries compared are; (i), L3/L4; (ii), L2/L3; (iii), L1/L2; (iv), Sub/L1. Note the lack of epitaxy across the cracked boundary (⇨) in both builds.

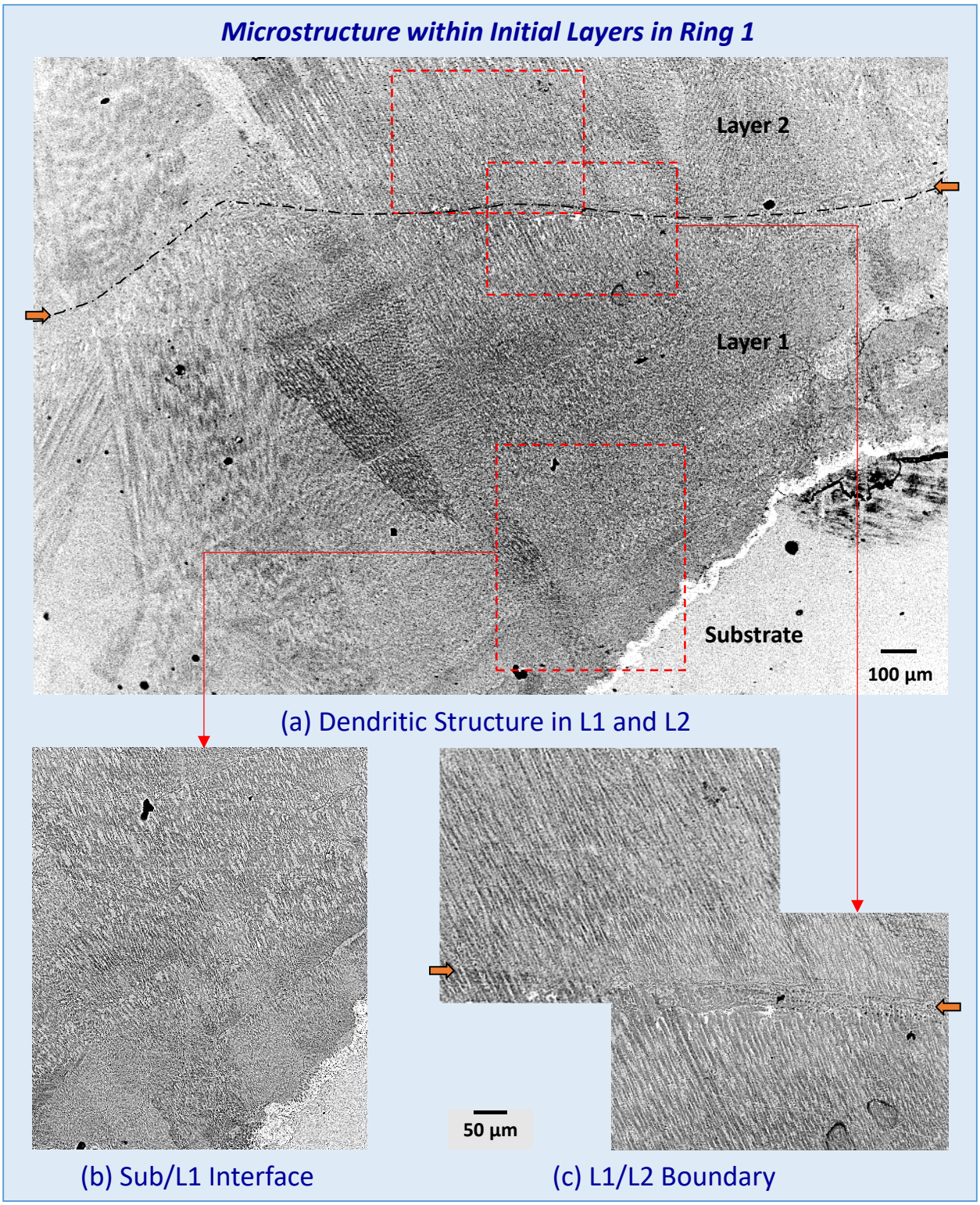

Figure 18. BSE image within Figure 17(a)(iii), revealing the microstructural characteristics of initial layers in Ring 1; (a), cellular dendritic microstructure; (b), Sub/L1 interface; (c), L1/L2 boundary (⇨). Note the epitaxial relationship between L1 and L2.

3.3. Compositional Characteristics

3.3.1. Bulk Chemical Analysis (Ring #1 & Ring #4)

The metallographic data suggest significant alloy mixing in the deposited material residing between the crack and the substrate in both ring sections. Bulk chemical analysis was employed to gain a broad sense of compositional variations within the Inconel 625 adjacent to the GRCop-84 substrate. The three discrete sections were extracted from similar locations in Ring 1 and Ring 4, roughly corresponding with the first four layers. The objective was to establish any differences in the degree of solute mixing within this alloy transition region. It should be noted that the sampling did not isolate layers and the results provide a comparison as a function of build height alone.

The bulk composition data are presented in table 3, which is accompanied by inset images indicating the precise locations of the analyzed sections. The top sections (C & F), representing the region 5-8 mm from the substrate, have a composition close to that of the feed wire with the inclusion of a small quantity of Cu. Section C in Ring 1 has a lower Cu content than Section F in Ring 4, i.e. 0.72 vs. 2.3 wt.%. The middle sections (B & E), representing the region 3.5-5.5 mm from the substrate, show a shift away from the wire composition due to increasing Cu content. Section B in Ring 1 has a lower Cu content than Section E in Ring 4, i.e. 2.9 vs. 7.2 wt.%. The bottom sections (A & D), representing the region 0-3 mm from the substrate, have a composition that deviates significantly from that of the Inconel 625 wire as a result of a large Cu content. Section A in Ring 1 has a higher Cu content than Section D in Ring 4, i.e. 37.6 vs. 20.6 wt.%, respectively.

3.3.2. Microchemical Analysis (Ring #1)

Establishing a difference in Cu gradient within the first 8 mm of the build height in Ring 1 and Ring 4 prompted a microanalytical investigation using SEM/EDS techniques. In contrast with bulk chemical analysis, the results from microchemical analysis provided layer-specific measures of solute blending and segregation. The first task was to quantify the Cu gradient in the first four layers at the outer wall of the deposits. The second task was to examine the distribution of Cu within the layers and at the interlayer boundaries. The main objective was to determine whether the Cu gradient and/or distribution exerted an influence on the location of crack formation. Figure 19 summarizes the analytical results from the region surrounding the interlayer boundary at which cracking originated in Ring 1, i.e. between L2 and L3.

The BSE(compo) image shows the outer wall of the build and corresponds with the last bead deposited in each of the first four layers. Two EDS datasets reveal the localized Cu content measured at regular increments relative to the build height, along with the calculated average values for each layer. The microchemistry data are in good agreement with the bulk chemistry data with regard to the overall gradient in Cu content through the transition region. The data indicate that the gradient is not smooth and discontinuities exist at each of the interlayer boundaries. Of significance, the differential is most pronounced (27.6 to 3.5 wt.%) at the L2/L3 boundary, the interlayer boundary where the crack initiated.

Table 3. Comparison of the variation in bulk composition with increasing build height between Ring 1 and Ring 4. Inset images illustrate specimen extraction at discrete increments from the Sub/L1 interface for the chemical analyses.

Variations in Bulk Composition with Build Height

Inconel 625		Elemental Composition (wt.%)					
		Ni	Cr	Mo	Nb	Others	Cu
Feed Wire		64.8	22.3	8.7	3.7	0.54	0.003
Ring 1	C	64.8	21.3	8.6	3.6	0.99	0.72
	B	63.2	21.0	8.3	3.7	0.87	2.9
	A	35.5	16.3	5.2	4.9	0.52	37.6
Ring 4	F	63.7	21.1	8.6	3.6	0.69	2.3
	E	59.3	21.1	8.1	3.6	0.68	7.2
	D	48.1	19.5	6.7	4.4	0.68	20.6

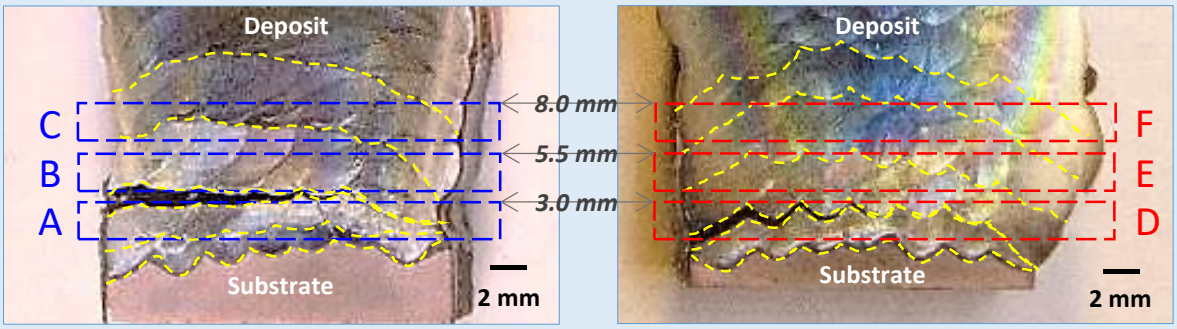

Ring 1 Ring 4

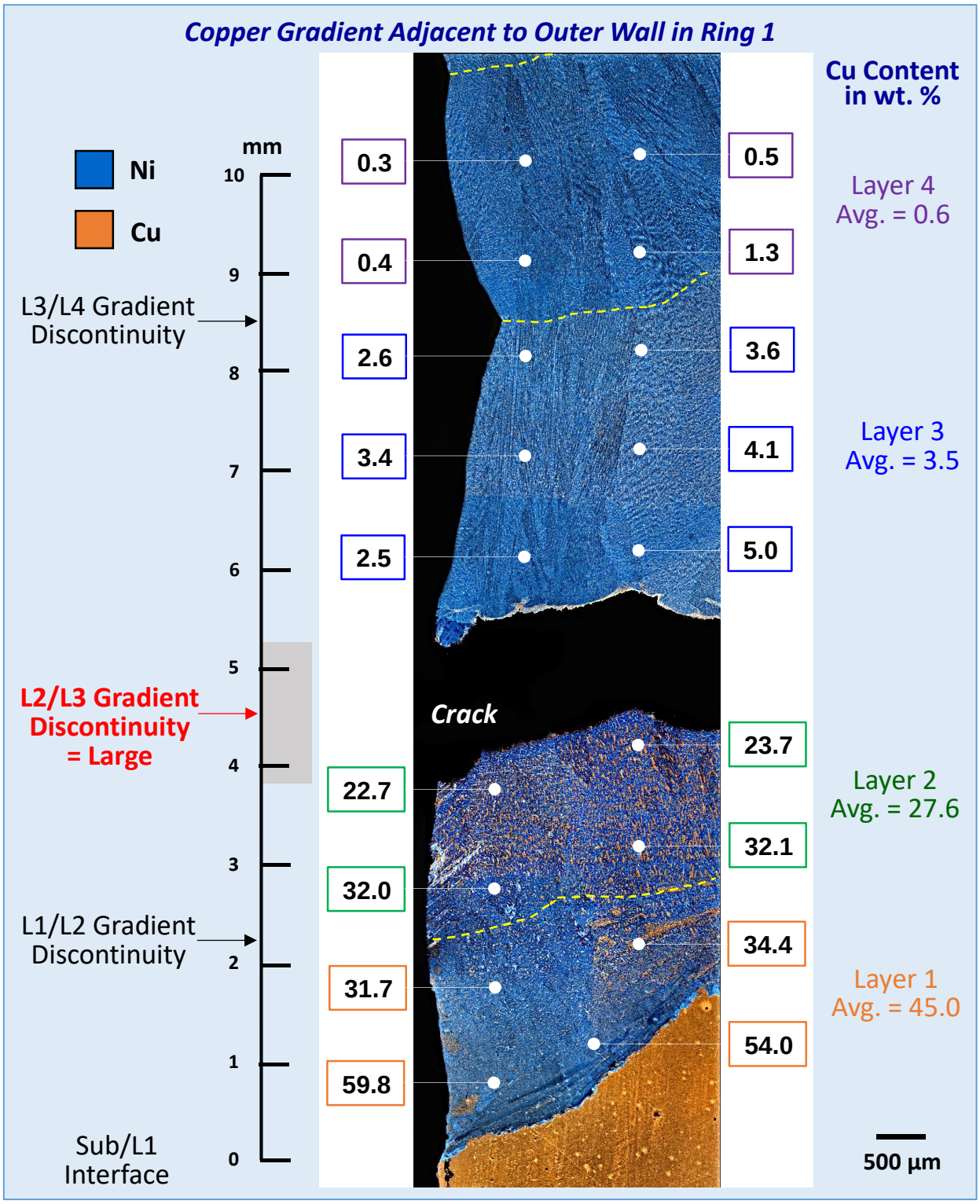

Figure 19. SEM compositional analysis – Cu gradient as a function of build height adjacent to the outer wall in Ring 1; BSE(compo) image showing microstructure adjacent to the crack, accompanied by the results from a series of EDS spectra collected normal to the crack.

The distribution of Cu in and around the first three interlayer boundaries of the build is shown in figure 20 and figure 21 for Ring 1 and later in figure 23 and figure 24 for Ring 4. The distributions of Cu and Nb in and around and the substrate/build interface are also included. Interfacial segregation of Nb may be indicative of the formation of $(Ni, Cr)_2(Nb, Mo)$ Laves phases and/or the agglomeration of Cr_2Nb dispersoids from the substrate. As an alloy constituent of both Inconel 625 and GRCop-84, the abundance of such Nb-bearing intermetallics may have contributed to the crack resistance of the interface.

For Ring 1, BSE BF/compo map pairs are shown in figure 20(a) and 20(b), respectively. Figure 20(a)(i) and 20(b)(i) show the L3/L4 boundary. Figure 20(a)(i) reveals that the dendritic microstructure is continuous across the boundary (highlighted). There is an obvious epitaxial relationship between the dendrite colonies on either side of the boundary that is maintained with varying orientations. Figure 20(b)(i) reveals a uniform Cu distribution within each of the adjoining layers with little segregation at the boundary. However, there is a differential in Cu content across the boundary; 3.5 wt.% in L3 decreases to 0.6 wt.% in L4.

When combined, figure 20(a)(ii)/20(b)(ii) and figure 20(a)(iii)/20(b)(iii) represent the L2/L3 boundary (across the crack). The BSE BF images reveal an absence of microstructural continuity across the boundary. The dendritic structure is well-defined in L3, whereas the dendritic structure is indistinct in L2. The compo maps reveal a markedly different Cu distribution in the layers on either side of the crack. Cu is evenly distributed through L3 as a fine dispersion. In contrast, the dispersion is coarse at the top of L2 and exhibits features consistent with extensive Cu interdendritic segregation. The differential in Cu content across this boundary is the largest; 27.6 wt.% in L2 decreases to 3.5 wt.% in L3. Of significance, there is also evidence of additional Cu segregation at the L2/L3 boundary. The compositional maps reveal that the upper and lower crack surfaces are decorated with a thin, continuous layer of Cu.

Figure 21(a)(i) and 21(b)(i) show the pair of images related to the L1/L2 boundary. BSE BF imaging is unable to resolve the dendritic structure in L1 and L2 in this instance (as revealed in figure 18). It should be noted that B7 is imaged in figure 21, whereas B3 is imaged in figure 18. The composition map suggests that the dispersion of interdendritic Cu is finer and more uniform in L1 than L2. The image also reveals the presence of coarse, globular inclusions of Cu interspersed within the dendrites. There is a differential in Cu content across the boundary; 45.0 wt.% in L1 decreases to 27.6 wt.% in L2.

Figure 21(a)(ii), 21(b)(ii), and 21(b)(iii) show a BSE BF image, plus Cu and Nb compositional maps, of the Sub/L1 interface. The Cu map suggests a finer dendritic structure at the bottom of L1, close to the substrate interface. Figure 21(b)(ii) also reveals evidence of Cu rafting close to and parallel with the interface. Figure 21(b)(iii) indicates that the Nb distribution is fairly uniform in both the deposit and the substrate. The Nb content across the interface drops from 5.4 wt.% in the substrate to 4.1 wt.% in L1. These values are comparable with starting materials; Nb content of GRCop-84 = 5.61 wt.% and Inconel 625 = 3.67 wt.% (table 2). However, a semi-continuous decoration of Nb-containing phase(s) on the Sub/L1 interface is also evident.

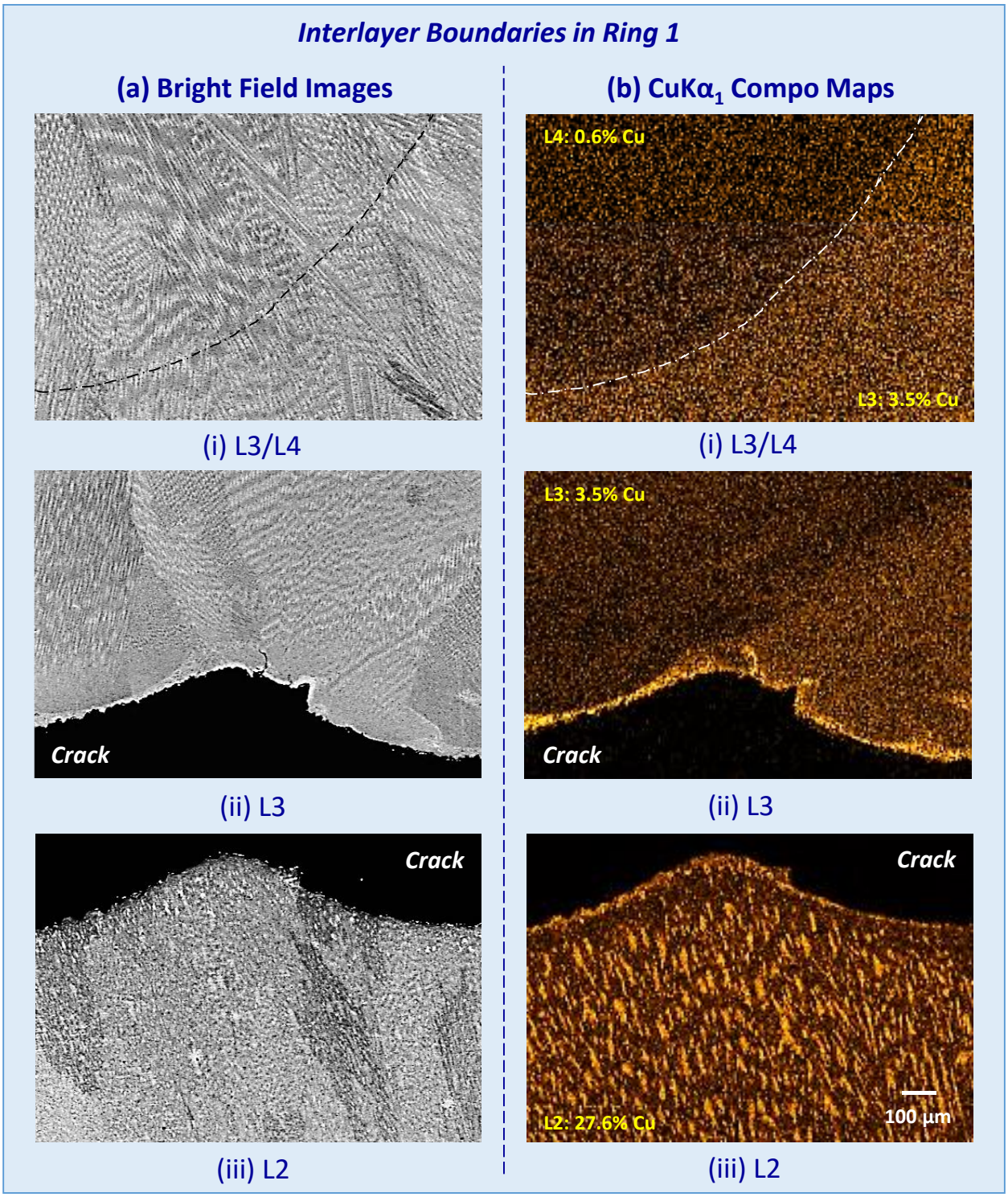

Figure 20. BSE imaging of interlayer boundaries in Ring 1; (a) bright field images, (b) CuKα$_1$ compo maps. The boundary characteristics shown are; (i), L4/L3; and L3/L2 is represented by (ii), L3, and (iii), L2 (separated by the crack).

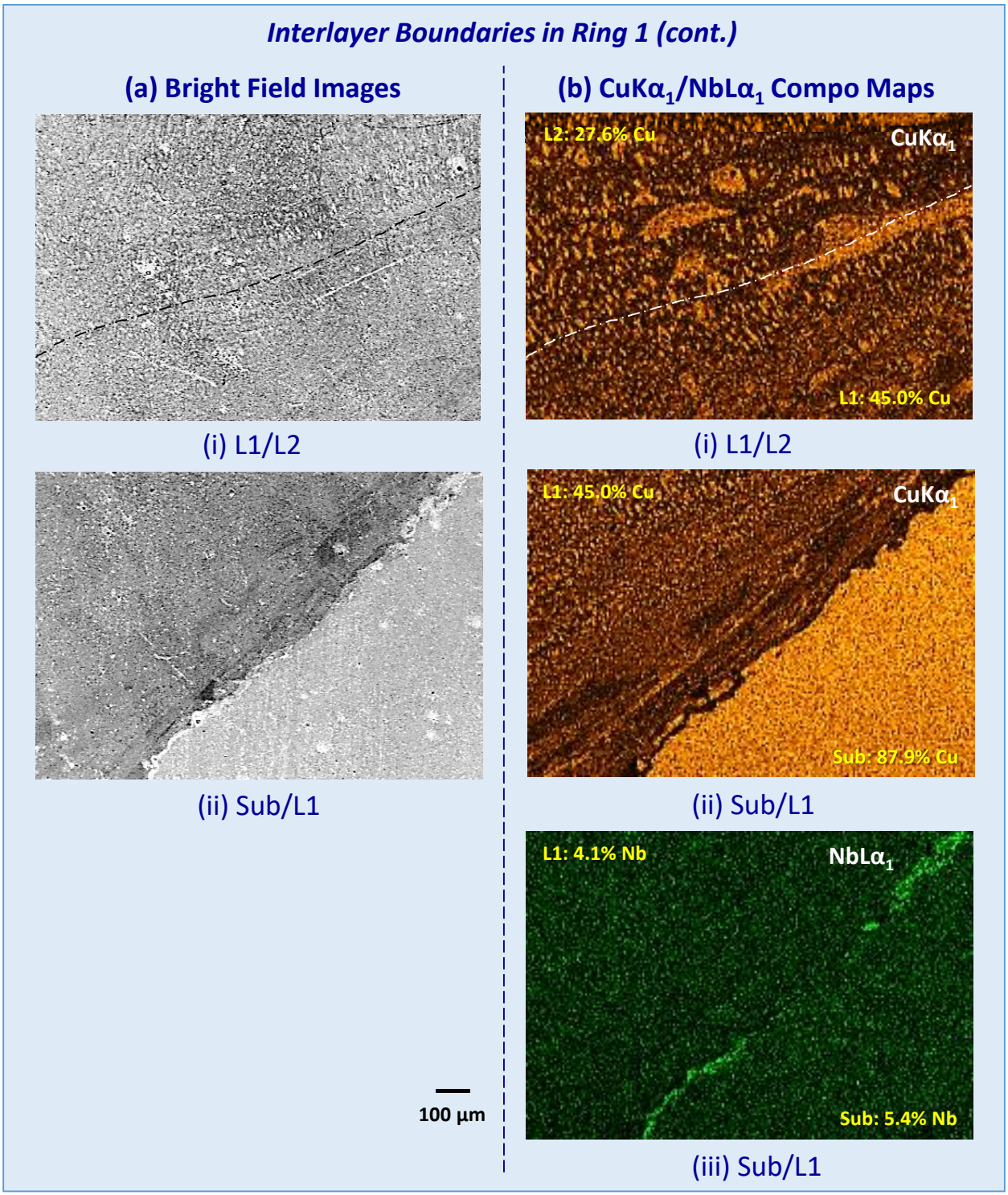

Figure 21. BSE imaging of interlayer boundaries in Ring 1 [continued]; (a) bright field images, (b), CuKα$_1$/NbLα$_1$.compo maps. The boundary characteristics shown are; (i), L1/L2 using CuKα$_1$, (ii), Sub/L1 using CuKα$_1$, and (iii), Sub/L1 using NbLα$_1$.

The results of spectrographic analysis of the Sub/L1 interface and surrounds are summarized in table 4. Spectra 8 and 12 show compositions representative of the bulk of L1 and the substrate, respectively. Spectrum 8 contains a contribution from interdendritic Cu segregation. Spectra 10 and 11 are associated with two types of phases residing at the Sub/L1 interface. The compositions are consistent with $(Ni, Cr)_2(Nb, Mo)$ Laves being the predominant phase, but the possibility of isolated MC (NbC) carbides remains (even with very low C content of alloy) [ref. 65]. There is also the possibility that Cr_2Nb dispersoids make a contribution to Spectrum 10. Primary, 0.5-1.0 µm diameter particles would be stable upon localized melting of the substrate during deposition of L1 [refs. 22and 25]. Superimposed on all of these spectra is a varying Cu content, reflecting the extensive migration of solute from the substrate into the deposited material.

Spectrum 9 coincides with the raft-like Cu segregation, as observed in figure 21(b)(ii). The composition of such Cu-rich regions provides an indication of the extent to which the local incipient melting point of the deposit is depressed. It is evident that the segregation within the build is not pure Cu, but more likely comprises a Cu/Ni solid solution. The Cu:Ni ratio is approximately 2.2:1, which is comparable with the composition of a CuNi30 cupronickel alloy (T_s= 1170°C). As outlined in table 1, the presence of this constituent will govern melting of the deposit (Inconel 625; T_s= 1290°C) during EBF^3 thermal cycling. Of significance, susceptibility to hot cracking increases with the width of the non-equilibrium STR.

3.3.3. Microchemical Analysis (Ring #4)

Figure 22 summarizes microchemical analysis results from the region surrounding the interlayer boundary at which cracking originated in Ring 4, i.e. between L1 and L2. The outer wall, corresponding with B7 in each of the first four layers is shown in the BSE(compo) image. The accompanying sets of EDS data reveal the incremental change in Cu content as a function of build height, including the average values calculated for each layer. The overall Cu gradient through the transition region indicated by the microchemistry data are in good agreement with the complementary bulk chemistry data. The data reveal that discontinuities exist at each of the interlayer boundaries and the gradient is not smooth. Of significance, the differential is most pronounced at the site of crack formation, i.e. the L1/L2 boundary(33.8 to 13.2 wt.%).

figure 23 and figure 24 contain BSE BF/compo map pairs that reveal the Cu distribution relative to the microstructure at each of the interlayer boundaries within Ring 4, and the distribution of Cu and Nb at the substrate/build interface. Figure 23(a)(i) and 23(b)(i) show the L3/L4 boundary. There is a differential in Cu content across the boundary; 4.4 wt.% in L3 decreases to 1.6 wt.% in L4. Figure 23(a)(ii) and 23(b)(ii) show the L2/L3 boundary. There is a differential in Cu content across the boundary; 13.2 wt.% in L2 decreases to 4.4 wt.% in L3. The BSE BF images reveal epitaxial growth of dendrites across both boundaries (highlighted) and the compo maps show a uniform dispersion of Cu in the adjoining layers with no boundary segregation.

Table 4. Solute distribution in B7 near the Sub/L1 interface in Ring 1. Inset BSE(compo) image shows the locations of a series of EDS spectra collected from discrete microstructural features.

Solute Segregation at Interface in Ring 1

Spectrum #	Composition (wt.%)				
	Ni	Cr	Mo	Nb	Cu
8	40.6	15.4	4.5	4.2	34.9
9	27.2	9.6	2.0	1.9	59.3
10	34.5	28.0	5.5	19.7	12.3
11	42.3	23.6	7.1	12.5	14.2
12	3.2	6.8	0	5.3	84.7

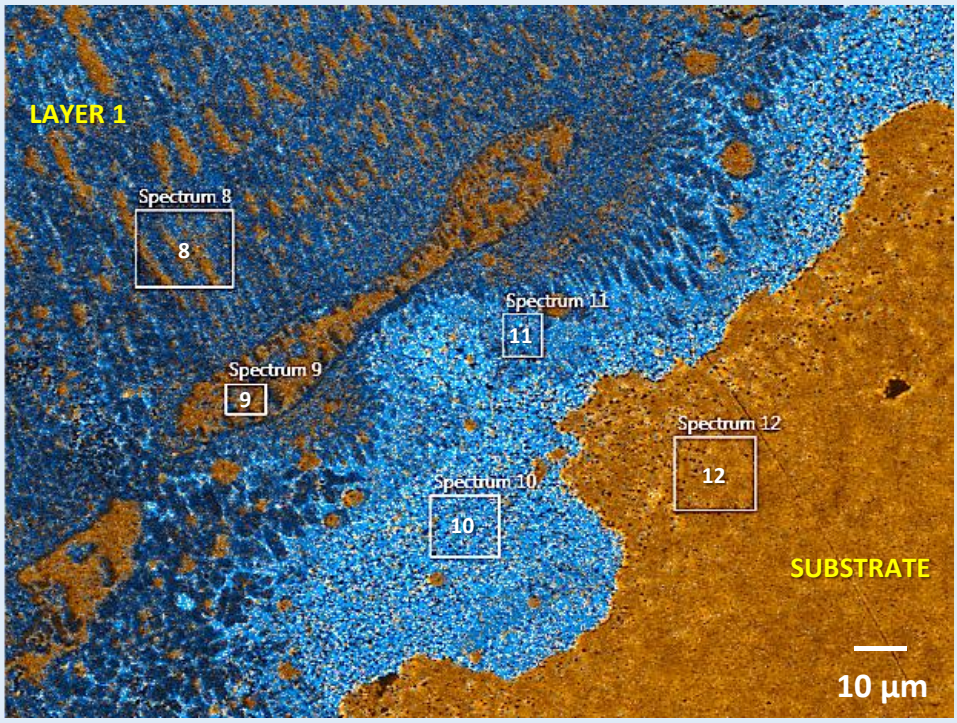

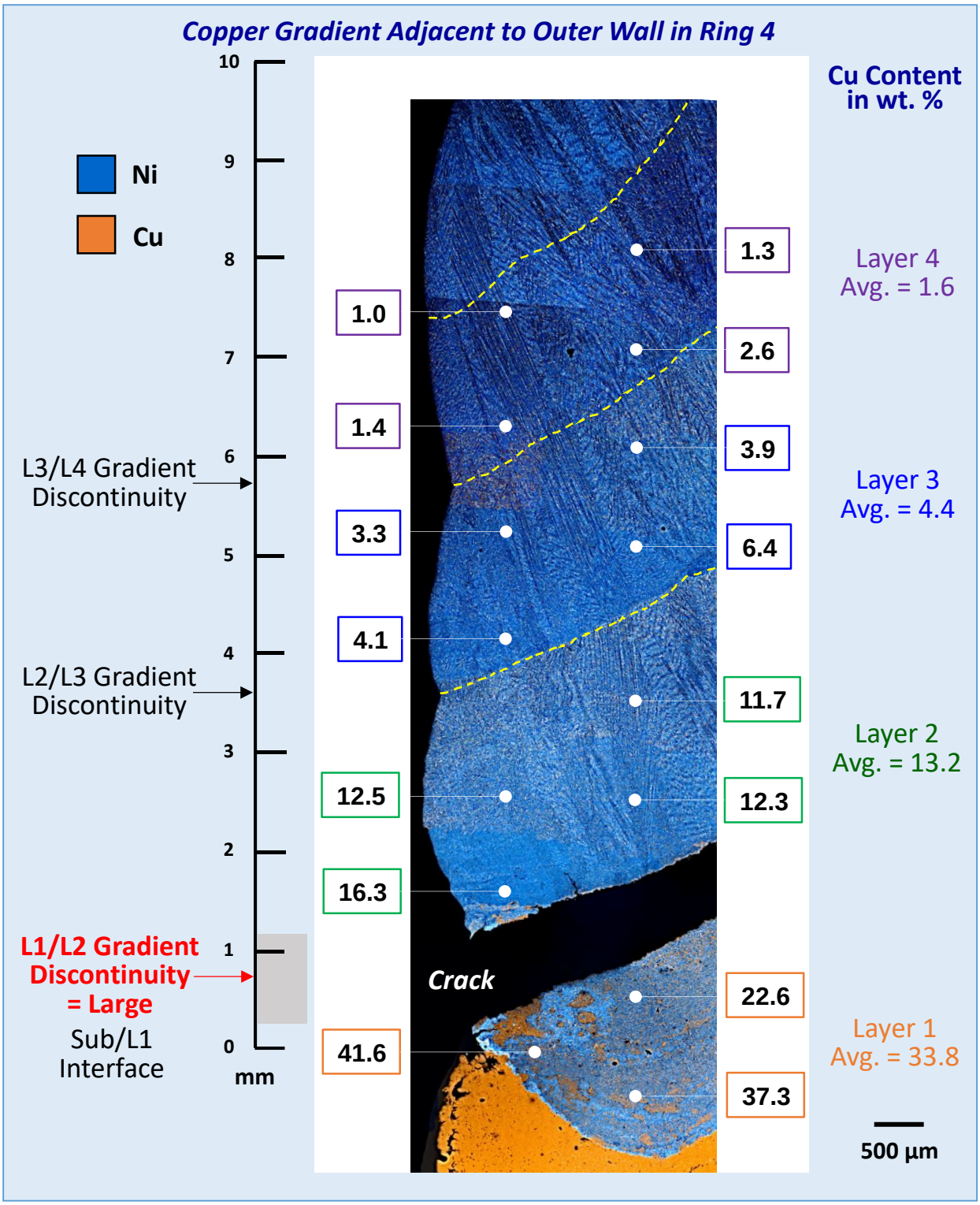

Figure 22. SEM compositional analysis – Cu gradient as a function of build height adjacent to the outer wall in Ring 4; BSE(compo) image showing microstructure adjacent to the crack, accompanied by the results from a series of EDS spectra collected normal to the crack.

In combination, figure 23(a)(iii)/23(b)(iii) and figure 24(a)(i)/24(b)(i) represent the L1/L2 boundary (across the crack). Comparing the BSE BF images reveals an absence of microstructural continuity across the boundary. The dendritic structure is well-defined in L2, whereas the dendritic structure is indistinct in L1. The compo maps reveal a markedly different Cu distribution in the layers on either side of the crack. The bottom of L2 contains a fine, uniform distribution of Cu, whereas the top of L1 contains a coarser distribution that includes larger, globular Cu segregation. The differential in Cu content across this boundary is the largest; 33.8 wt.% in L1 decreases to 13.2 wt.% in L2. Of significance, there is additional segregation on the L1/L2 boundary; the crack surfaces are decorated with a thin, continuous layer of Cu.

Figure 24(a)(ii), 24(b)(ii), and 24(b)(iii) show a BSE BF image, plus Cu and Nb compositional maps, of the Sub/L1 interface. The Cu map reveals many globular Cu segregation at the bottom of L1, close to the substrate interface in addition to the interdendritic segregation. The Nb map indicates a fairly uniform distribution in L1, with the exception of the locations of the globular Cu inclusions. The Nb content across the interface drops from 5.5 wt.% in the substrate to 4.3 wt.% in L1. Again, these values are comparable with starting materials; Nb content of GRCop-84 = 5.61 wt.% and Inconel 625 = 3.67 wt.% (table 2). Similar to Ring 1, there is also evidence of a semi-continuous decoration of Nb-containing phase(s) on the Sub/L1 interface in Ring 4.

The results of spectrographic analysis of the globular Cu-rich segregation and surrounds in B7 of L1 in Ring 4 are summarized in table 5. Spectra 1-4 show that the composition of the surrounding matrix has a Cu content that varies between 17.0 and 29.8 wt.%. Spectra 5-7 show the composition of the Cu-rich inclusions to vary between 61.5 and 76.5 wt.%. The mean value is comparable with the average Cu content of L1 being 33.8 wt.%, as determined in figure 22. Again, the globules likely comprise a Cu/Ni solid solution, with minor contributions from other solute. Spectrum 5 shows a Cu:Ni ratio of 4.5:1, consistent with a CuNi20 alloy (T_s = 1140°C). Spectra 6 and 7 show a Cu:Ni ratio of 2.3:1, consistent with a CuNi30 alloy (T_s = 1170°C). Therefore, the incipient melting point within the alloy transition zone of the deposit is depressed by 120°C from the equilibrium solidus, T_s = 1290°C. This is significant because the corresponding increase in the STR enhances the susceptibility to hot cracking when compared with solidification of a monolithic Inconel 625 deposit.

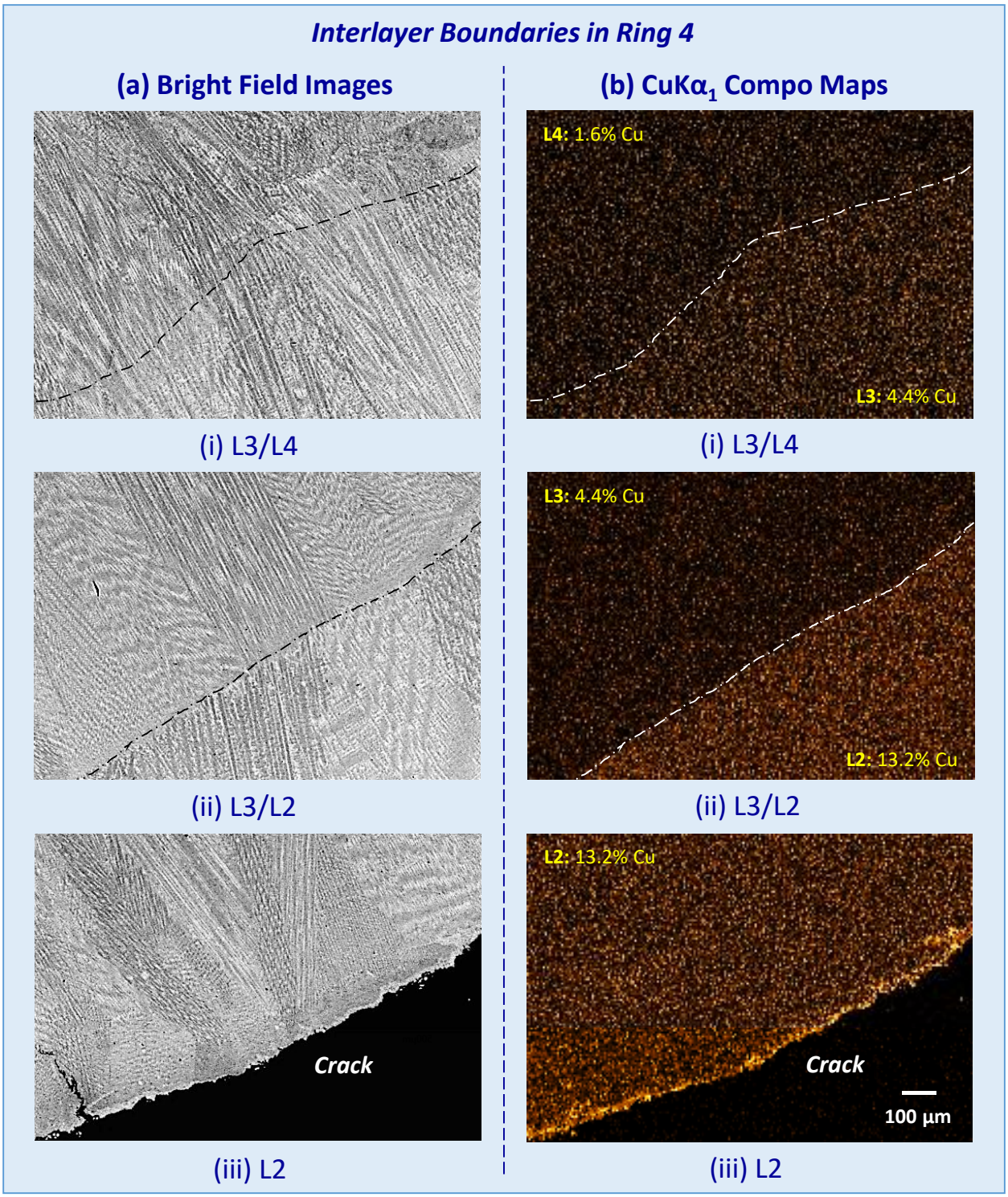

Figure 23. BSE imaging of interlayer boundaries in Ring 4; (a) bright field images, (b) CuKα$_1$ compo maps. The boundary characteristics shown are; (i), L3/L4, (ii), L2/L3, and (iii), L2 (above the crack).

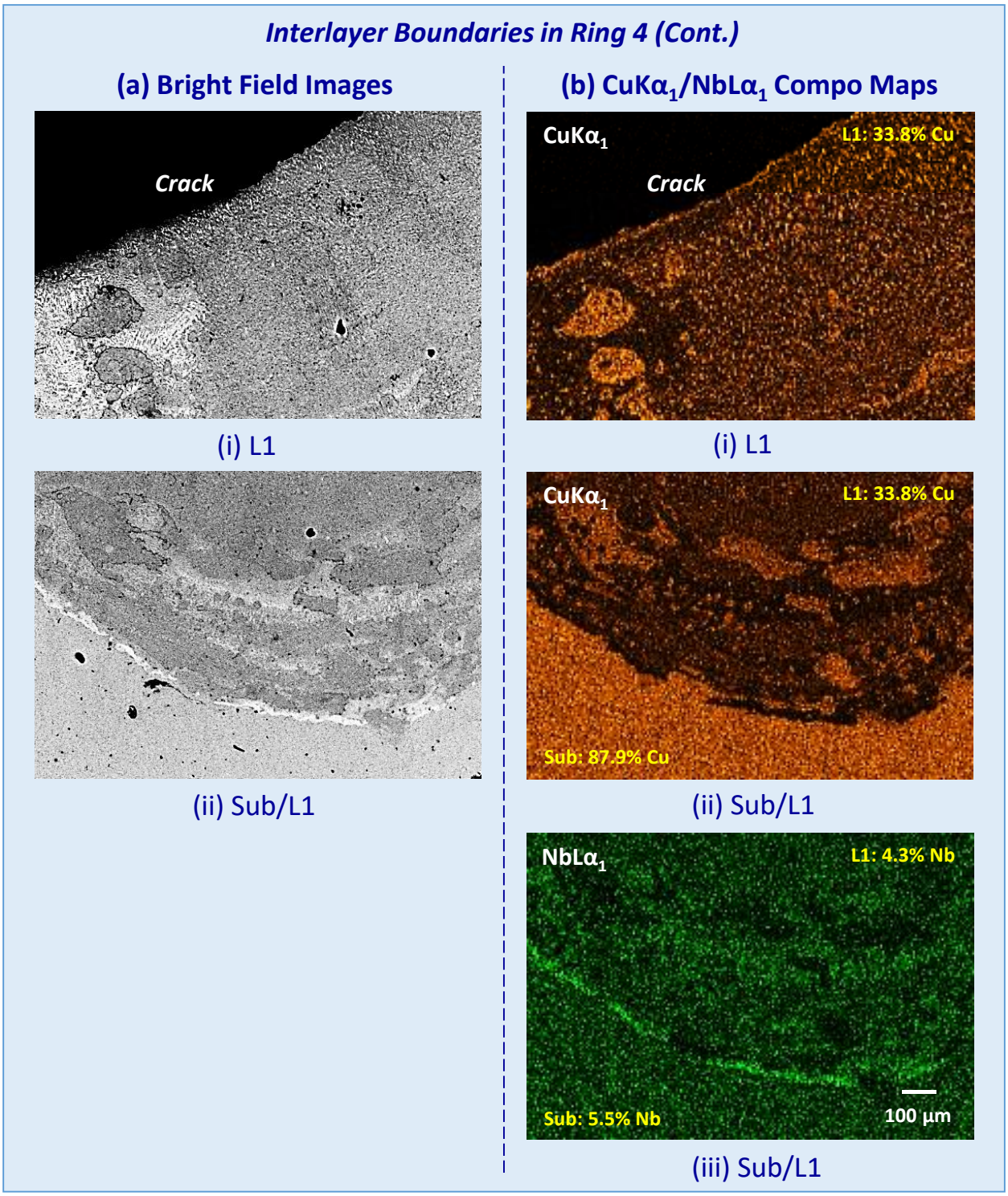

Figure 24. BSE imaging of interlayer boundaries in Ring 4 [continued]; (a) bright field images, (b), $CuK\alpha_1/NbL\alpha_1$.compo maps. The boundary characteristics shown are; (i), L1 (below the crack) using $CuK\alpha_1$, (ii), Sub/L1 using $CuK\alpha_1$, and (iii), Sub/L1 using $NbL\alpha_1$.

Table 5. Solute distribution within B7 of L1 in Ring 4. Inset BSE(compo) image shows the locations of a series of EDS spectra collected from discrete microstructural features.

Solute Segregation in Layer 1 of Ring 4

Spectrum #	Composition (wt.%)				
	Ni	Cr	Mo	Nb	Cu
1	44.2	21.9	8.0	8.6	17.0
2	43.4	21.6	8.6	8.0	18.1
3	43.1	20.9	8.2	7.7	19.8
4	41.4	17.6	6.1	5.0	29.8
5	16.7	5.4	0.2	1.0	76.5
6	24.8	9.8	1.6	2.4	61.5
7	24.3	9.6	1.4	2.3	62.3

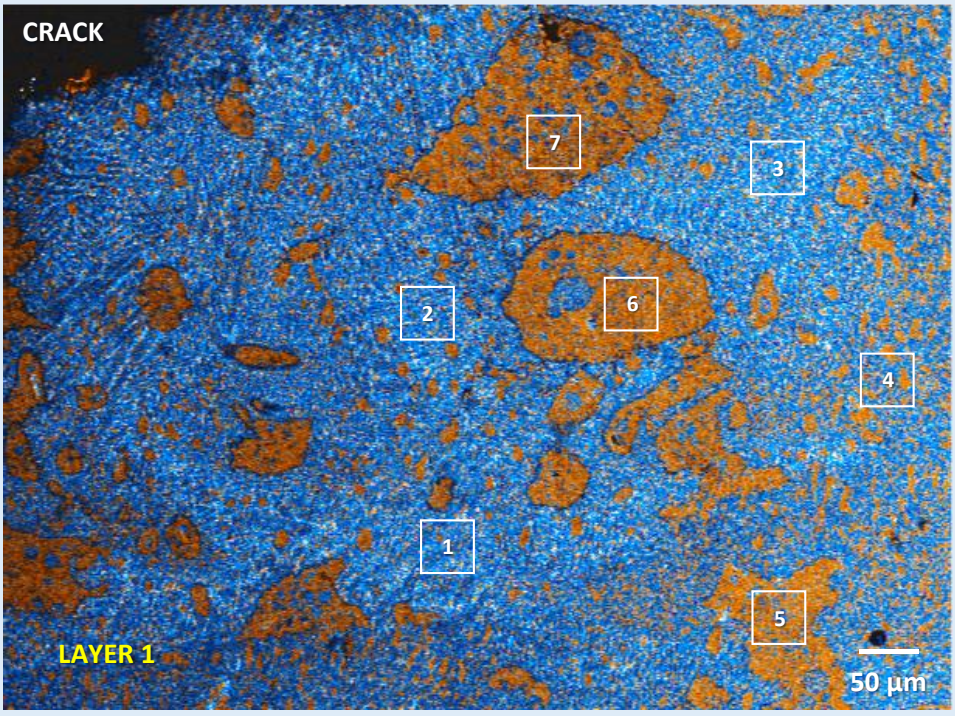

3.4. Fracture Characteristics

The philosophy adopted during fractographic analysis was to divide the cracking behavior into two regimes, referred to as crack formation and crack opening. Crack formation is associated with crack initiation and early crack propagation that likely involves progressive fracture. Crack opening is correlated with extensive crack growth that likely involves unstable fracture. Examination of crack formation took precedent over crack opening in order to gain the most insight on the prevention of cracking. Consequently, the focus was on the outer half of the wall thickness, specifically the fracture characteristics associated with B7, B6 and B5. The results are interpreted by alluding to fracture modes and mechanisms established for weld cracking in Ni-base alloys.

Common to both Ring 1 and Ring 4, the crack path follows an interlayer boundary that exhibits no epitaxial growth, no dendritic bridging, and is heavily decorated with a Cu-rich phase. It has been established that none of the other interlayer boundaries exhibit these characteristics in either deposit. The degree of epitaxy may be correlated with the crystallographic misorientation of an interlayer boundary. The presence or absence of epitaxial growth, may be equated with behavior as a low- or high-angle GB, respectively [ref. 66]. Adopting this analogy, the isolated interlayer boundaries at which cracking occurred may be treated as high-angle GBs. Fractography may then be interpreted as intergranular separation potentially being influenced by a prominent GB phase.

The microstructure neighboring the cracks comprises cellular dendrite colonies intersecting the interface at a high angle. These dendritic grain structures also contain interdendritic segregation of the Cu-rich phase. Impingement of these features on the interlayer boundary contributes to the topography of the crack. In addition to these microstructural features, there is another factor that will influence crack morphology. It is evident that the primary direction of fracture is from the outer wall to the inner wall of both deposits. However, it is unlikely that crack growth in the radial direction occurred at the same rate around the circumference. There is a high probability that crack extension through the cross-section includes a radial and a circumferential contribution. This eliminates interpolation of any directionality in fracture characteristics, such as asymmetric features pointing toward the site of crack origination.

3.4.1. Fractographic Analysis (Ring #1)

In figure 25, the profile of the interlayer crack is correlated with the macroscopic and microscopic characteristics of fracture in Ring 1. The positions of the seven, individual beads (B7 through B1) that constitute L2 are included for reference. The SEM/BSE(compo) image in figure 25(a) reveals that the primary crack path is relatively straight with small undulations coinciding with the array of beads. On this scale, the only evidence of secondary cracking is in B3 that contains a single, large crack. The higher Cu content below (L2) than above (L3) is readily discernible along the length of the primary crack, particularly near the outer wall. The dispersion of Cu-rich phase is coarser within B7, B6, and B5 and there appears to be more Cu accumulation on the corresponding crack surface.

The macrograph in figure 25(b) provides a plan view of the lower crack surface (L2) traversing the whole cross-section. Macroscopically, the surface appears dull gray and fibrous from B7 to B2. The exceptions are B3, that contains the secondary crack, and B1, where sawing to separate the crack created the surface finish. In general, the crack topography comprises a series of ridges that reflect the bead spacing, but a pronounced lip between B6 and B5 (⇨) is evident. The

accompanying SEM/SE(topo) images in figure 25(c) provide roadmaps for fractographic analysis of cracking near the outer wall (B7, B6, and B5). The image reveals that the intersection of B6 with B5 (⇨) coincides with a marked change in the crack surface characteristics. A significant decrease in the surface roughness across the lip is suggestive of a transition in fracture behavior.

A closer inspection of the change in fracture surface characteristics between B6 and B5 in Ring 1 is presented in figure 26. The BSE(compo) image in figure 26(a) reaffirms that the Cu content below the crack (L2) is significantly higher than above the crack (L3). The location of the pronounced lip coinciding with the intersection of an inter-bead boundary with the interlayer boundary is also confirmed. The underlying microstructural characteristics in L2 reveal that the dispersion of Cu-rich phase within the dendritic structure is much coarser in B5 than B6. The Cu segregation is distributed as more widely spaced, globular inclusions, even though the level of Cu may not have changed. Segregation of Cu between B6 and B5 and between L2 and L3 is also evident. The inter-bead boundary is decorated with a continuous band and the interlayer boundary is partially-decorated with Cu-rich phase that varies in thickness.

Figure 26(a) also reveals that the crack path traverses some of the Cu-rich phases residing at the interlayer boundary. The accompanying SE(topo) images in figure 26(b) and (c) show crack morphologies representative of the B6 and B5 cross-sections. B6 in figure 26(b) exhibits a tortuous fracture surface with features comprising a random pattern. B5 in figure 26(c) exhibits a much flatter fracture surface containing shallower features in a more regular pattern. Any relationship between these fracture characteristics and either the underlying dendritic microstructure, or the distribution of Cu-rich phase on the crack surfaces is not readily discernible.

The higher magnification SE(topo) images contained in figure 27 outline the change in fracture behavior during early cracking near the outer wall in Ring 1. The radial fracture direction through B7, B6, and B5 is identified in figure 27(a) for reference. Figure 27(b), (c), and (d) show the fracture characteristics representative of the mid-section of B7, B6, and B5, respectively. The most noticeable difference is that the roughness of the fracture surface progressively decreases from B7 to B5. B7 in figure 27(b) exhibits a very tortuous crack path with some evidence of interdendritic separation. It is likely that fracture through the Cu-rich interlayer phase contributed to smoothing of the facets. The rounded protuberances are indicative of molten metal involvement in the fracture process [ref. 35], i.e. hot cracking in the semi-solid state.

In contrast, fracture of B5 in figure 27(d) displays a predominantly planar surface with a textured appearance. The sharper and finer characteristics are consistent with solid state fracture through the Cu-rich interlayer phase and evidence of interdendritic separation is absent. The surface is pock-marked, which is suggestive of localized plastic deformation involving microstructural bridges through the interlayer. The dispersion of irregular-shaped and round cavities may be indicative of dendrite tip and Laves phase pull-out, respectively [ref. 16]. The survival of such well-defined features in the presence of molten metal is improbable, suggesting elevated temperature fracture in the solid state by warm cracking phenomena.

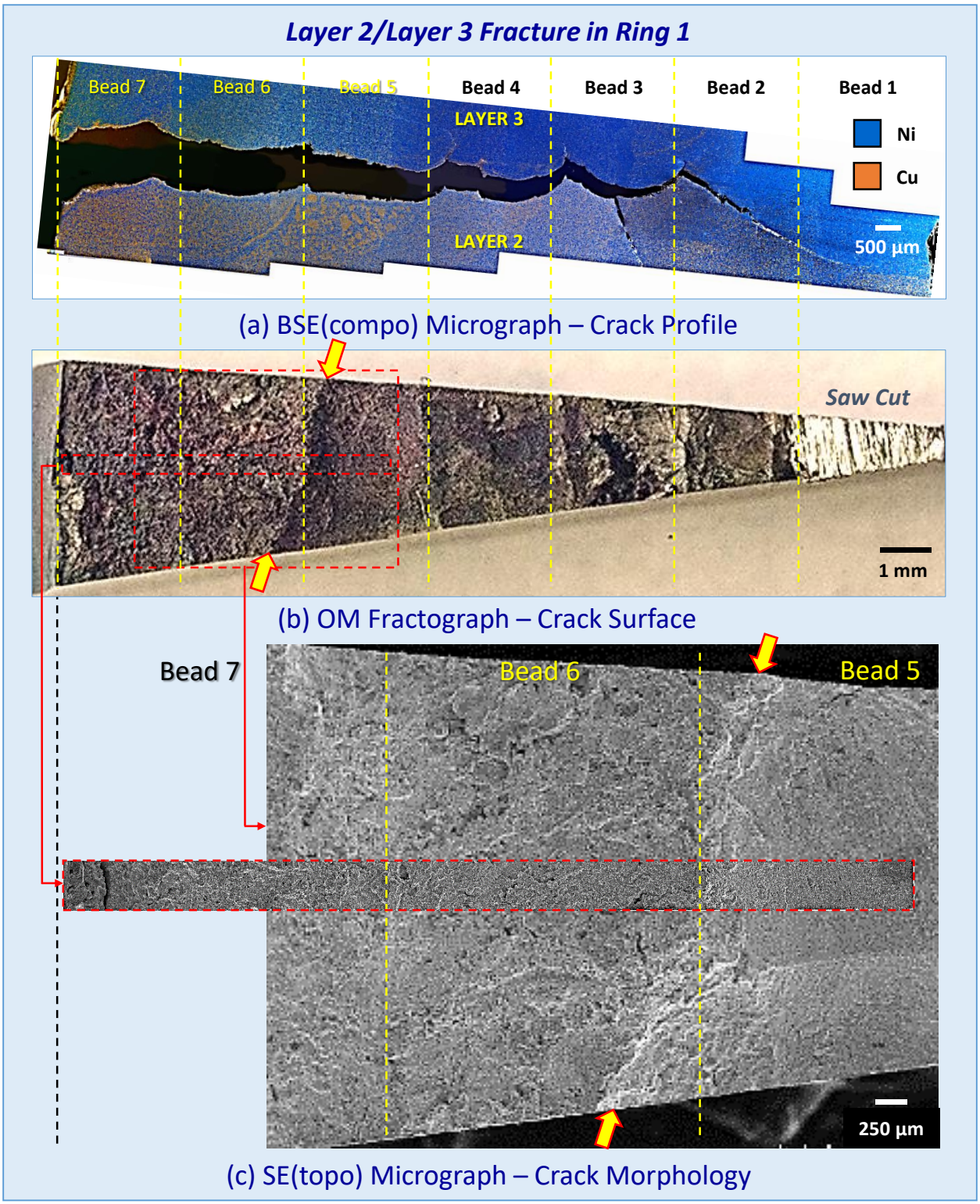

Figure 25. Fracture characteristics at the L2/L3 boundary through the cross-section of Ring 1; (a), BSE(compo) image of crack profile; (b), OM fractograph of crack surface; (c), SE(topo) images of fracture morphology in B7, B6, and B5. Note the pronounced ridge (⇨) between B6 and B5.

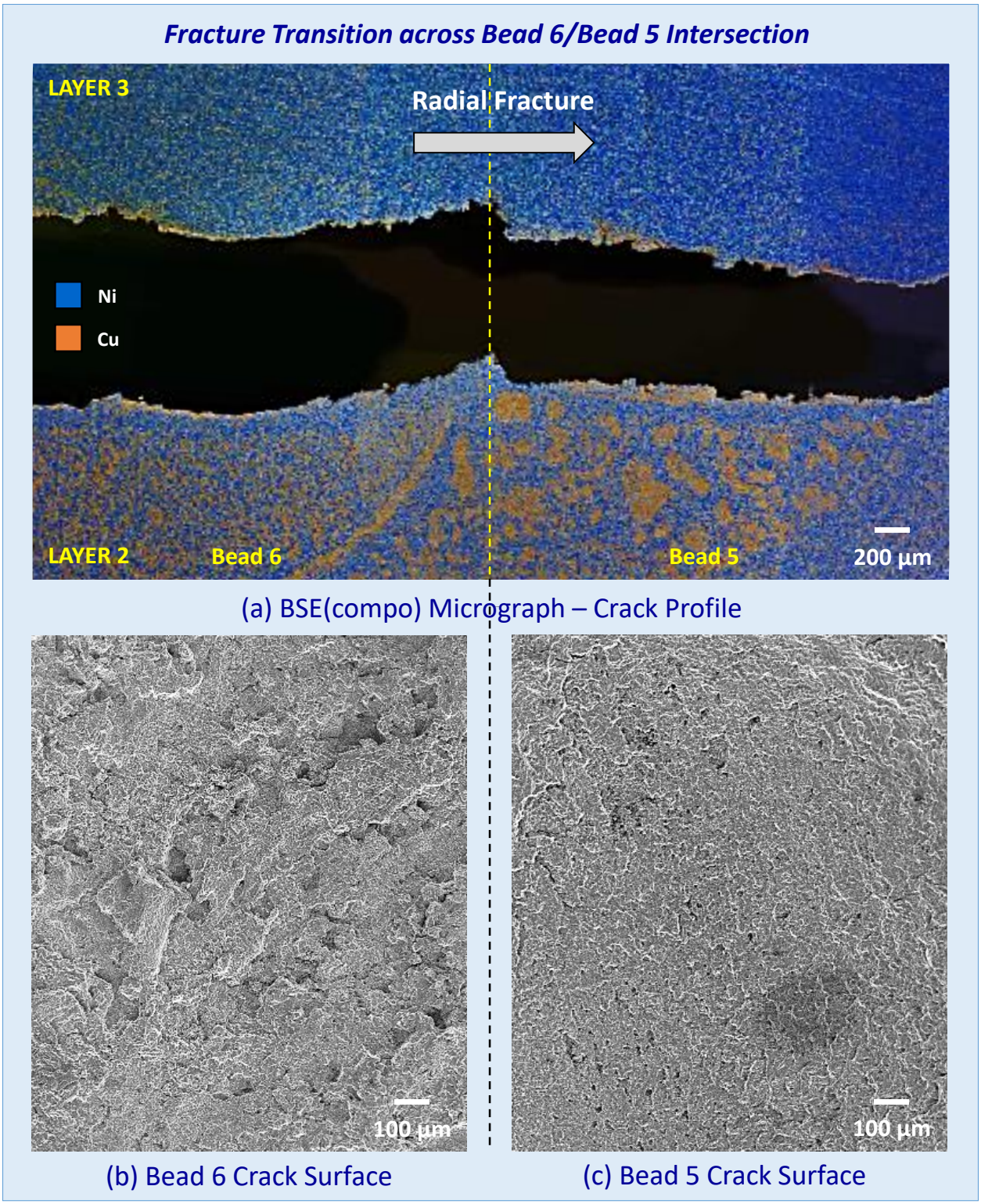

Figure 26. SEM imaging to correlate fractographic features of the lower crack surface with the crack profile across the B6/B5 intersection in L2 of Ring 1; (a), BSE(compo) image of crack profile; (b), SE(topo) image of B6; (c), SE(topo) image of B5. Note that the direction of fracture is left to right.

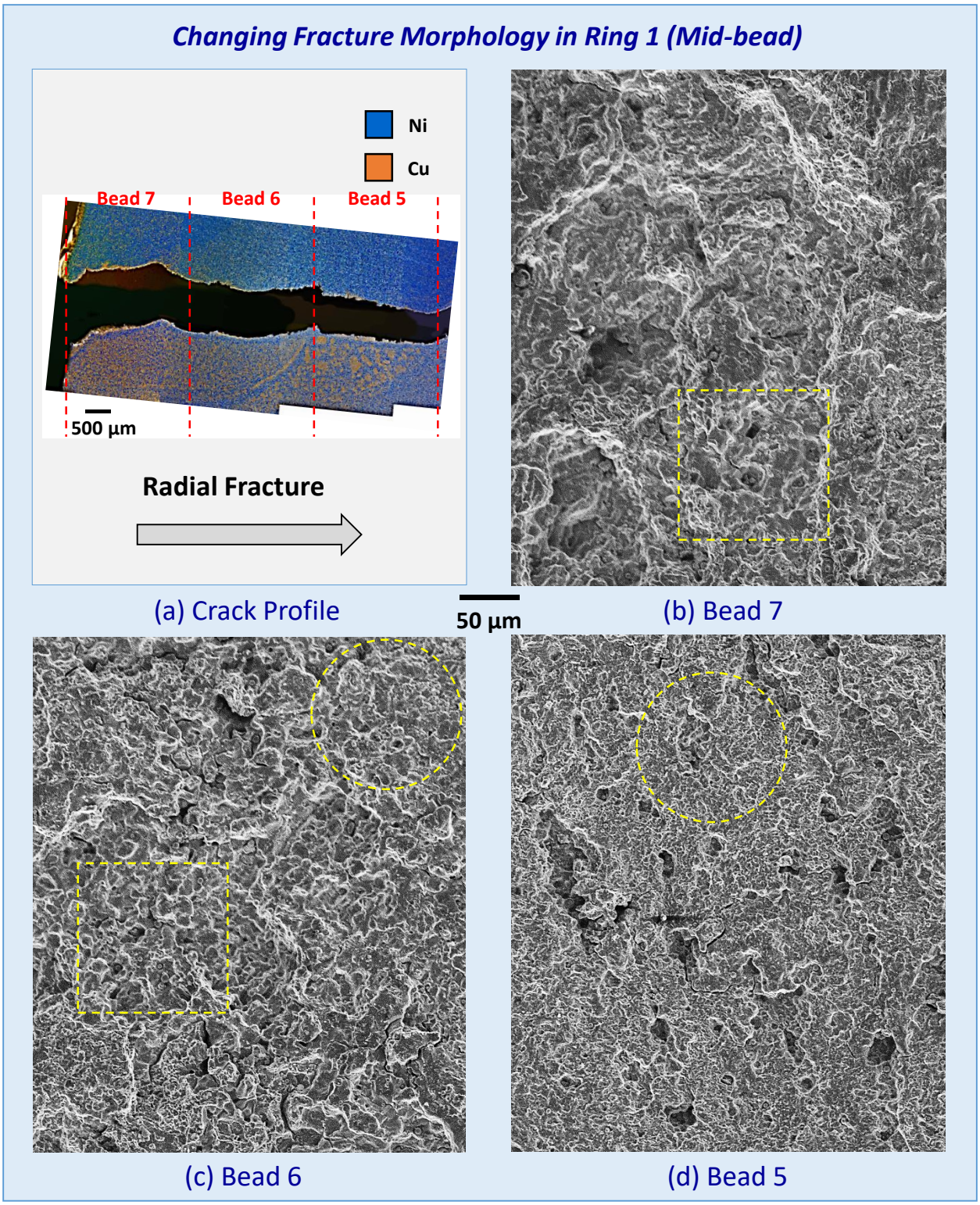

Figure 27. SEM images documenting the transition in fracture morphology between B7 and B5 in L2 of Ring 1; (a), BSE(compo) image of crack profile and representative SE(topo) images of the lower crack surface in; (b), B7, (c), B6, and (d), B5. Note that the direction of fracture is left to right.

Fracture across B6 in figure 27(c) may be regarded as a mixture of the morphologies exhibited by the crack surfaces in B7 and B5. The squares highlight areas of commonality between B6 and B7, and the circles between B6 and B5. Most of the fracture surface is tortuous, comprising rounded dendritic protuberances that appear shallower than in B7. The surface also displays isolated regions of flatter fracture, that comprise fine, sharp features similar to B5. Such a description strengthens the notion of a transition in fracture behavior as the crack traversed B6. The concept of cracking by a mixture of semi-solid state interdendritic fracture and solid state flat fracture has been introduced previously [ref. 67]. This raises the possibility that the fracture process involved a combination of, or a transition between, hot cracking and warm cracking phenomena.

3.4.2. Fractographic Analysis (Ring #4)

In figure 28, the interlayer crack profile is correlated with the macro- and micro-scopic fracture characteristics in Ring 4. The BSE(compo) image in figure 28(a) highlights a serrated crack path that adheres to an interlayer boundary. Note that the geometry of the individual beads is more scalloped when compared with Ring 1. The size and spacing of the serrations are coincident with the established bead pattern from B7 through B2. There is also evidence of secondary cracking into L1 and L2 along the primary crack, the largest residing in B5 and B4 of L1. The differential in Cu content across the crack is clearly visible over most of the cross-section. The dispersion of Cu appears fairly uniform and is coarser from B7 through B4. In contrast with Ring 1, larger, globular inclusions are more isolated and are located in the vicinity of the outer wall in B7 only. Decoration of the crack surface with Cu-rich phase is not clearly discernible in this cross-sectional view.

The macrograph in figure 28(b) provides a better view of the lower crack surface on L1. The correlation between the fracture path undulations and the periodicity of the bead array is illustrated. The crack topography resembles a geological formation that consists of a series of regularly-spaced ridges separated by valleys containing rivulets. Secondary cracking is not evident in B7 through B5, but large secondary cracks are visible in B4 onwards. The crack morphology in Ring 4 appears smoother and brighter than the characteristics of Ring 1. The most noticeable feature is that the crack surface is heavily laden with shiny, Cu-rich phase near the outer wall. B7 and B6 exhibit a continuous coating, B5 is partially coated, and coverage of B4 is further reduced.

The SE(topo) image in figure 28(c) provides a roadmap for fractographic analysis from crack origination in B7 to crack extension through the remaining beads. The location of figure 28(c) within figure 28(b) is outlined for comparative purposes. The periodic arrangement of ridges and valleys on the crack surface approximates the bead width and spacing. The bead interiors are populated with a network of protuberances that may be a reflection of the underlying microstructure. These vein-like features are pronounced in B7 and B6, but become much less distinct in B5 and beyond. The diminishing Cu coating witnessed in figure 28(b) appears to coincide with the change in fracture characteristics observed in figure 28(c).

An assessment of the transition in fracture characteristics from B6 to B5 of Ring 4 is presented in figure 29. The BSE(compo) image of the crack profile in figure 29(a) shows that the serrated crack has a predominantly flat surface and the Cu coating seen in figure 28(b) is indiscernible. The higher Cu content below (L1) than above (L2) the crack is readily apparent. The dispersion of the Cu-rich phase does not alter from B6 to B5, being comparable with the size/distribution

observed in B6 of Ring 1. The SE(topo) images in figure 29(b) and (c) reveal that the fracture morphology in B6 and B5 has much in common. The indistinct characteristics are consistent with decohesive rupture through the interlayer phase in the semi-solid state. The crack surface gently undulates between protruding ridges, the most prominent being oriented parallel to the radial direction. Many of these ridges are likely associated with intersection of the SGBs separating dendrite colonies with the fracture surface (figure 5).

There is a decrease in the surface roughness between B6 and B5 that could be related to an increase in the crack growth rate and is manifested in two ways. First, the ridges are fewer and protrude less in B5 than B6, as highlighted by the insets. Second, the topography of the regions between these protrusions, the majority of the fracture surface, is flatter. In B6, these regions display a random, speckled appearance and are punctuated with smaller ridges of varying orientation. The contours of these minor ridges may be a reflection of fluid flow in the interlayer during cracking. The curvature and orientation of a few ridges are also reminiscent of the beach markings observed on fatigue fractures [ref. 41]. In B5, the regions between the larger ridges exhibit a periodic, textured appearance and the network of curved smaller ridges is absent. This transition suggests a reduction in thickness of the molten interlayer, thereby exposing traces of the cellular dendritic structure beneath.

The changes in fracture characteristics during early cracking near the outer wall in Ring 4 are depicted in figure 30. The BSE(compo) image in figure 30(a) outlines the serrated crack profile and identifies the radial fracture direction. The higher magnification SE(topo) images in figure 30(b), (c), and (d) are representative of the topographic features at the mid-bead location in B7, B6, and B5, respectively. The bulk of the fracture surface, between the ridges, is flatter than the topography observed in figure 27 for Ring 1. As shown in figure 28(b), the smoothness of the features is suggestive of semi-solid state fracture through the Cu-rich interlayer. In figure 30(b), the characteristics in B7 comprise a jagged, almost ductile appearance, and evidence of the underlying dendritic structure is absent. In figure 30(d), B5 exhibits a planar, almost brittle appearance, and the periodic array of fine protuberances resembles the tips of cellular dendrites (figure 5). In figure 30(c), a closer inspection of B6 suggests that the curved features may be indicative of successive positions of an advancing crack front. In general, the surface morphology in B6 may be described as a mixture of the features contained within B7 and B5. The squares highlight areas of commonality between B6 and B7, the circles between B6 and B5. This suggests a gradual change in fracture characteristics from B7 to B5, the progression being most evident across B6.

In contrast with Ring 1, the transition between B6 and B5 is not related to a change in fracture behavior, i.e. hot cracking to warm cracking. The difference in characteristics is reminiscent of figure 9 and is more likely related to a decrease in the volume of terminal liquid present during fracture [ref. 35]. Therefore, hot cracking through the interlayer phase persists in B5, but traces of the underlying cellular dendritic structure have emerged. The so-called eggcrate pattern associated with such decohesive rupture has been observed in both melted and re-solidified GB phases, i.e. following fracture in either the semi-solid or solid state [ref. 41]. The characteristics observed in figure 28(c) suggest a progressive shift towards solid state fracture, but these observations indicate that the transition to warm cracking occurred beyond B5 in Ring 4.

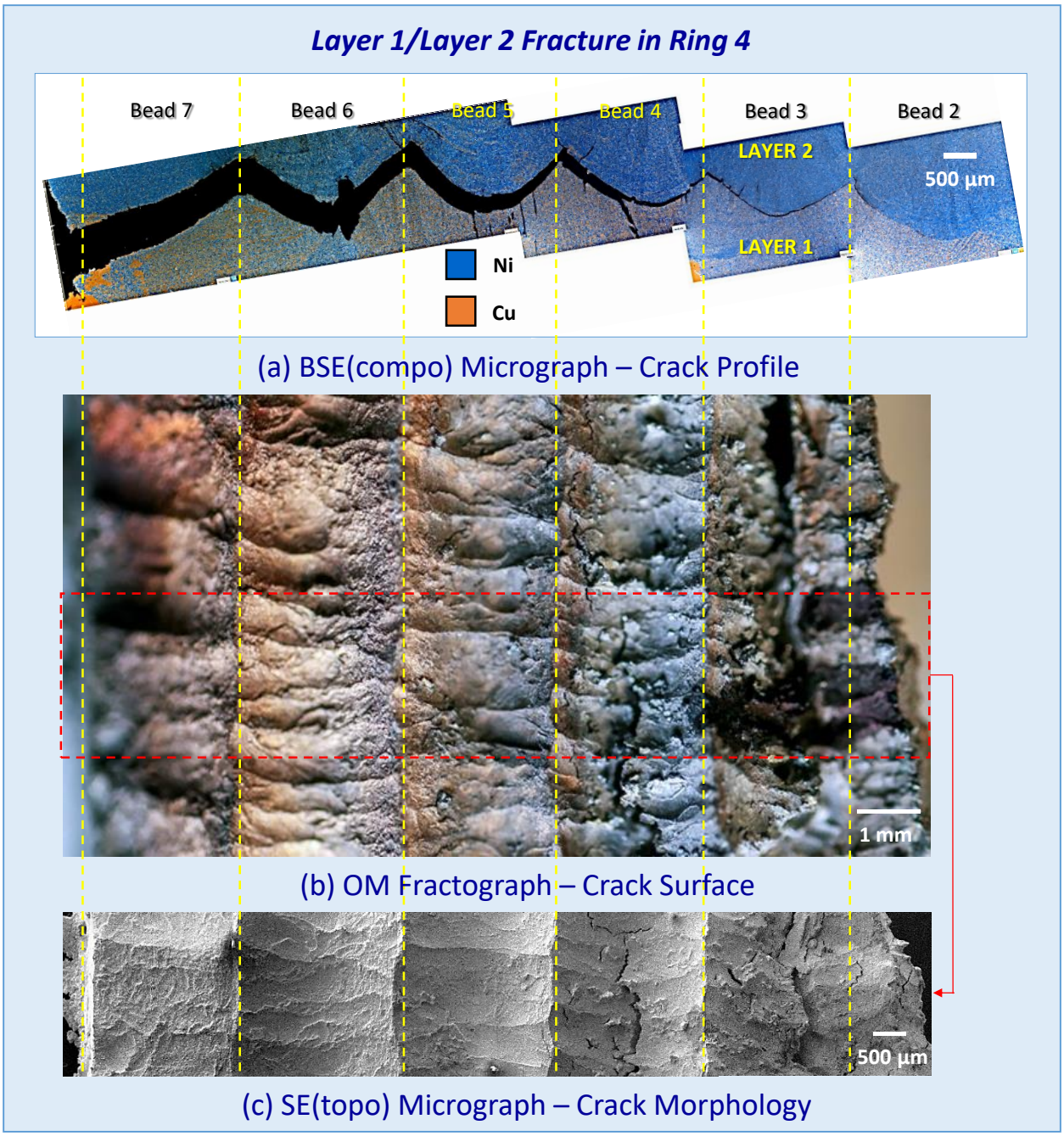

Figure 28. Fracture characteristics at the L1/L2 boundary through the cross-section of Ring 4; (a), BSE(compo) image of crack profile; (b), OM fractograph of crack surface; (c), SE(topo) image of fracture morphology. Note the Cu coating on the fracture surface that diminishes from left to right.

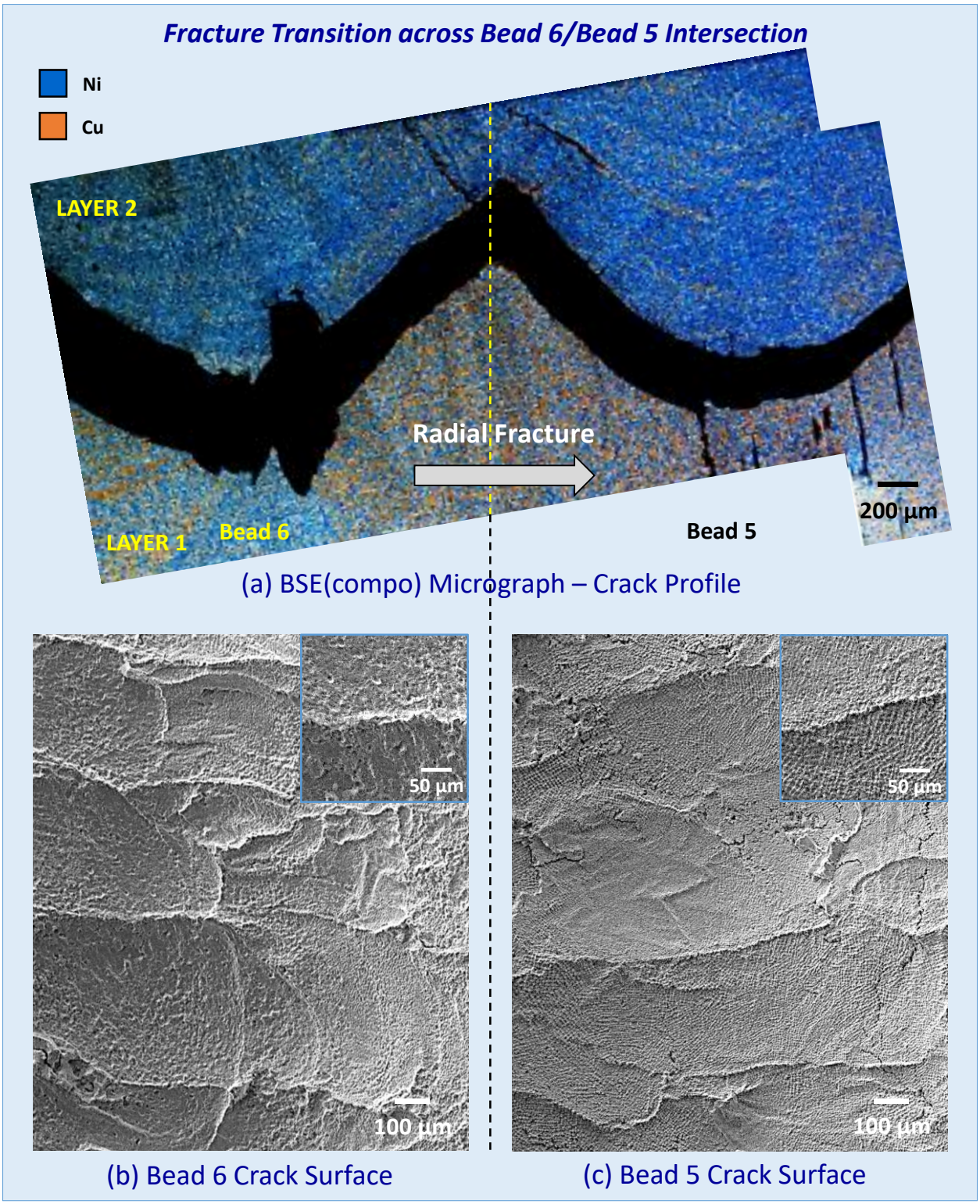

Figure 29. SEM imaging to correlate fractographic features of the lower crack surface with the crack profile across the B6/B5 intersection in L2 of Ring 4; (a), BSE(compo) image of crack profile; (b), SE(topo) image of B6; (c), SE(topo) image of B5. Note that the direction of fracture is left to right.

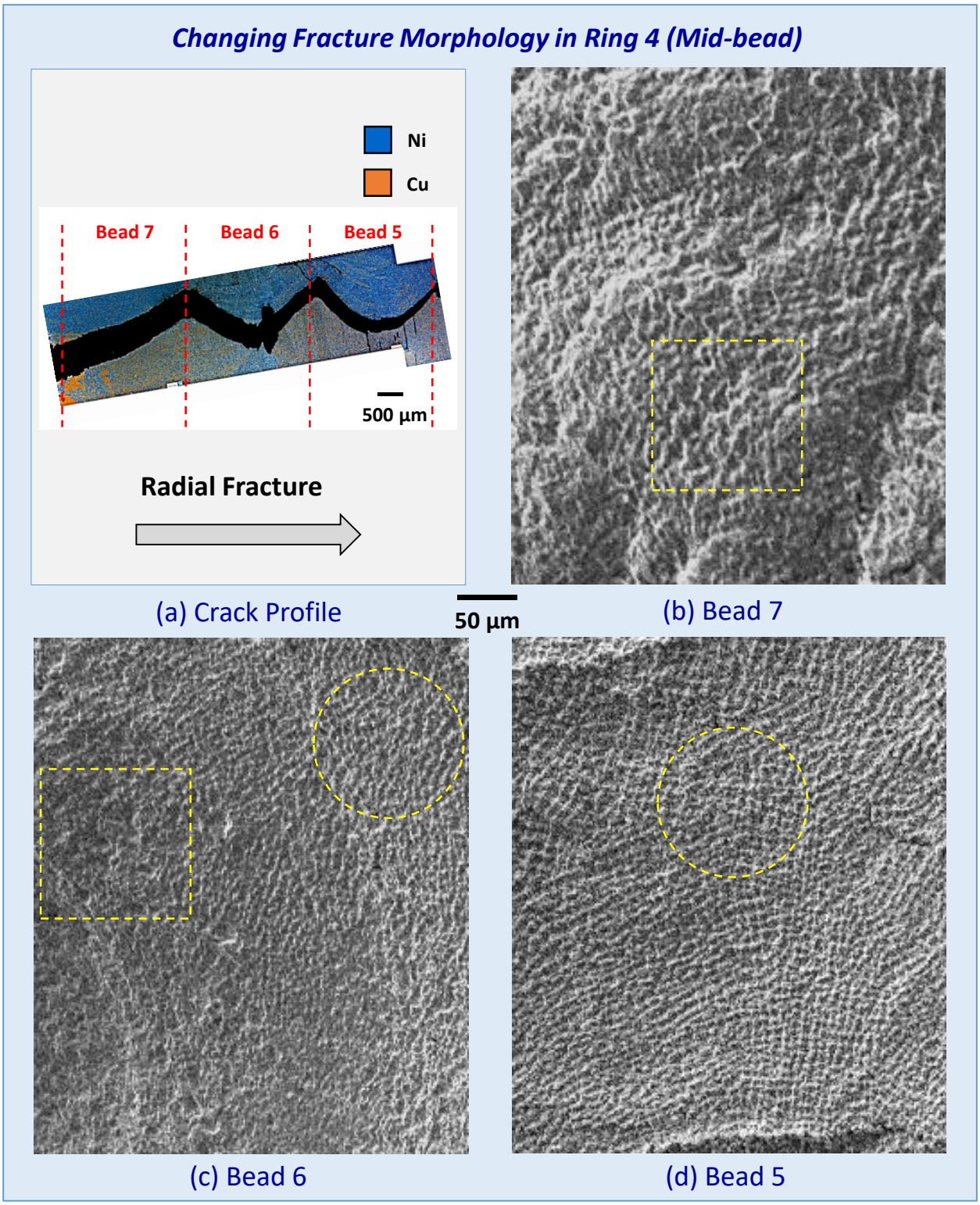

Figure 30. SEM images documenting the transition in fracture morphology between B7 and B5 in L1 of Ring 4; (a), BSE(compo) image of crack profile and representative SE(topo) images of the lower crack surface in; (b), B7, (c), B6, and (d), B5. Note that the direction of fracture is left to right.

4. Discussion

4.1. Microstructural Evidence

The primary objective of this investigation was to ascertain the metallurgical reasons for the premature cracking during EBF^3 of Ring 1 and Ring 4. The initial premise was that prevailing conditions at the union between GRCop-84 and Inconel 625 were most favorable for crack formation in both cases. First, the substrate/build interface was heavily decorated with brittle, intermetallic phases, representing a low-resistance crack path. Second, the combined effects of solidification shrinkage and differential CTE were optimal, exerting the largest driving force for fracture. Unexpectedly, cracking did not occur at the interface, but entirely within deposited material close to the substrate. The primary crack path was confined to an interlayer boundary in builds produced under markedly different processing conditions. This evidence strongly suggested that the cohesive strength of the fractured boundary was inferior to that of the substrate/build interface in each instance.

In Ring 1 and Ring 4, the microstructure of the deposited material exhibited a cellular dendritic structure oriented in close proximity with the build direction. This alignment reflected the dominant heat flux direction through the substrate. The resultant absence of dendrite branching during cellular dendritic solidification limited segregation between the growing colonies [ref. 29]. As a consequence, low melting point constituents were free-flowing, rather than trapped, and tended to be propelled ahead of the advancing S-L interface (figure 6). This may explain the propensity for the Cu-rich phase to accumulate at interlayer boundaries within the alloy transition zone of the deposits.

An ‘interlayer boundary’ in layer additive builds may be considered analogous to an ‘inter-pass boundary’ in multiple bead welds. Such boundaries are confined to the perimeter of weld beads and separate freshly deposited from previously deposited metal. Therefore, interlayer boundaries can exhibit characteristics similar to SGBs, but the process by which they form is different. SGBs are created by impingement of dendrite colonies during weld solidification. The misorientation of such boundaries is governed by the crystallographic mismatch between the adjacent dendritic colonies. As depicted in figure 5, a low-angle or high-angle SGB can result that depends on the inclination of the convergent dendritic growth.

In contrast, the formation of interlayer boundaries involves advancing dendritic growth, the solidification front migrates away from the re-solidified dendritic grain structure in the preceding layer. A close orientation relationship between dendrites across such boundaries signifies epitaxial growth and the creation of a low-angle SGB. Limited dendritic growth can traverse the interface, but the presence of excessive terminal liquid can inhibit such ‘microstructural bridging’ [ref. 36]. In effect, the loss of epitaxy results in the formation of a high-angle SGB that is prone to intergranular segregation and fracture mechanisms [ref. 66].

The current evidence suggests that continuous layers of segregation within the deposited metal were unable to sustain the thermally-induced stresses generated during solidification and subsequent cooling. In Ring 1 and Ring 4, the crack progressed along a single interlayer boundary that represented a path of least resistance when compared with all other interlayer boundaries. In both cases, the fractured boundary was heavily-decorated with a Cu-rich phase and exhibited a lack of epitaxy between the adjacent layers. The intergranular appearance of the fracture was consistent with the isolated, interlayer boundary behaving like a high-angle SGB.

4.2. Compositional Evidence

The solubility limit of Cr, Mo, and Nb in Cu was low in the liquid state, and minimal in the solid state [ref. 50]. The complete miscibility of Ni in Cu and the limited solubility of the other solute elements dictated that segregation comprised a Cu/Ni solid solution. The Ni content of these Cu-rich zones within the material transition zone governed the incipient melting point of the first few deposited layers. Microchemical analysis of Ring 1 and Ring 4 suggested that the composition of the Cu-rich segregation was comparable to the cupronickel alloy CuNi30. As illustrated in figure 31, the STR of this alloy is 1170°C to 1240°C. In comparison, the T_s and T_l of monolithic Inconel 625 are 1290°C and 1350°C, corresponding to an equilibrium STR of $\Delta T = 60°C$ (table 1). As a consequence, the incipient melting point was reduced from 1290°C to 1170°C, resulting in a non-equilibrium STR of $\Delta T = 180°C$. This increased the duration and volume of terminal liquid at the end of solidification and promoted hot cracking between the deposited layers in the alloy mixing zone.

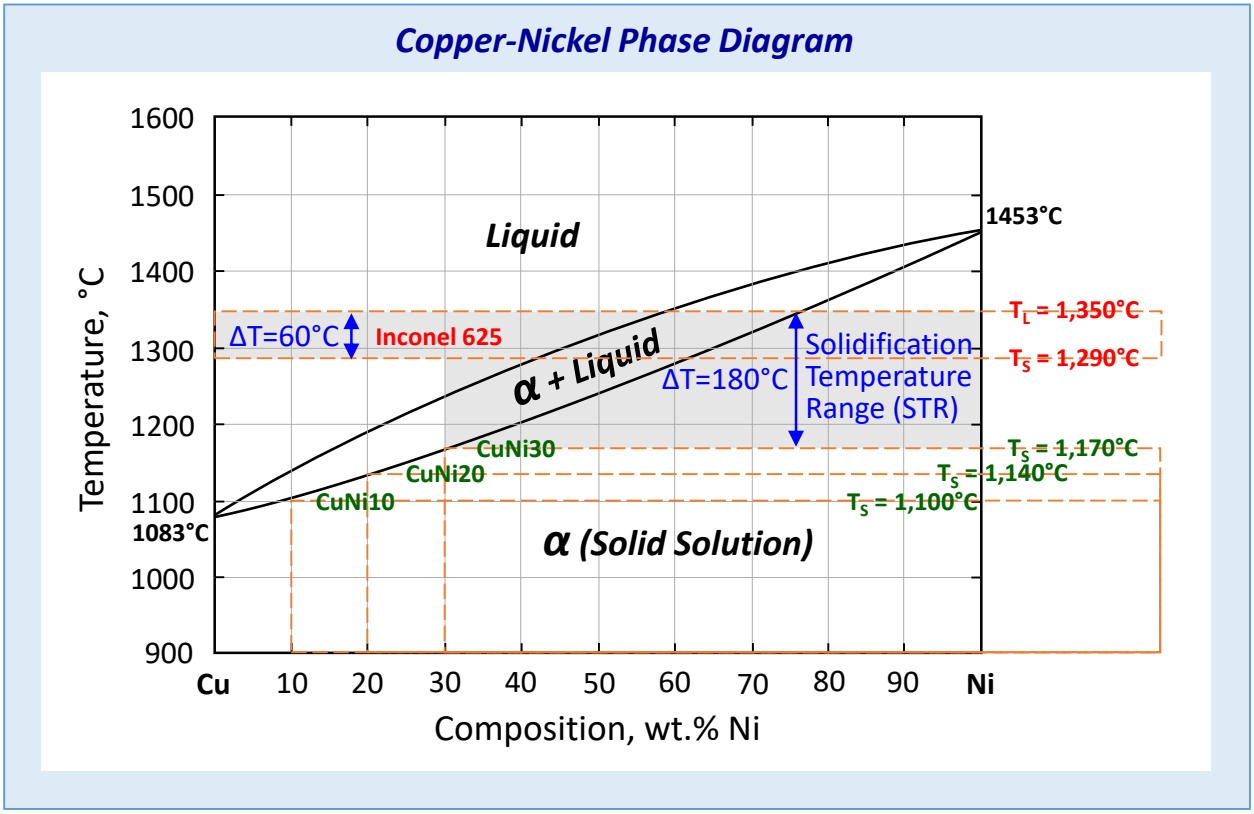

Figure 31. Using the Cu-Ni phase diagram to illustrate the dependence of the STR on the Ni content of a Cu-rich phase in an Inconel 625/GRCop-84 blend. Note that the composition of the Cu/Ni solid solution governs the incipient melting point in the alloy mixing zone.

An attempt to establish a relationship between solute mixing of the dissimilar alloys and the location of crack formation in the semi-solid state is illustrated in figure 32. The bulk chemistry and EDS analyses encompassing the first four layers in each deposit are compared in figure 32(a). The initial crack path resided between L2 and L3 in Ring 1 (figure 32(b)), but betweenL1 and L2 in Ring 4 (figure 32(c)). The same processing parameters were employed to deposit L1 in Ring 1 and Ring 4. Therefore, the Cu content in L1 was equal for both builds prior to the deposition of subsequent layers (L2+). The processing conditions for L2+ in Ring 1 and Ring 4

were such that no appreciable change in the layer height or the re-melt depth was expected. It was anticipated that the twofold increase in the substrate temperature would promote Cu migration into the build in Ring 4.

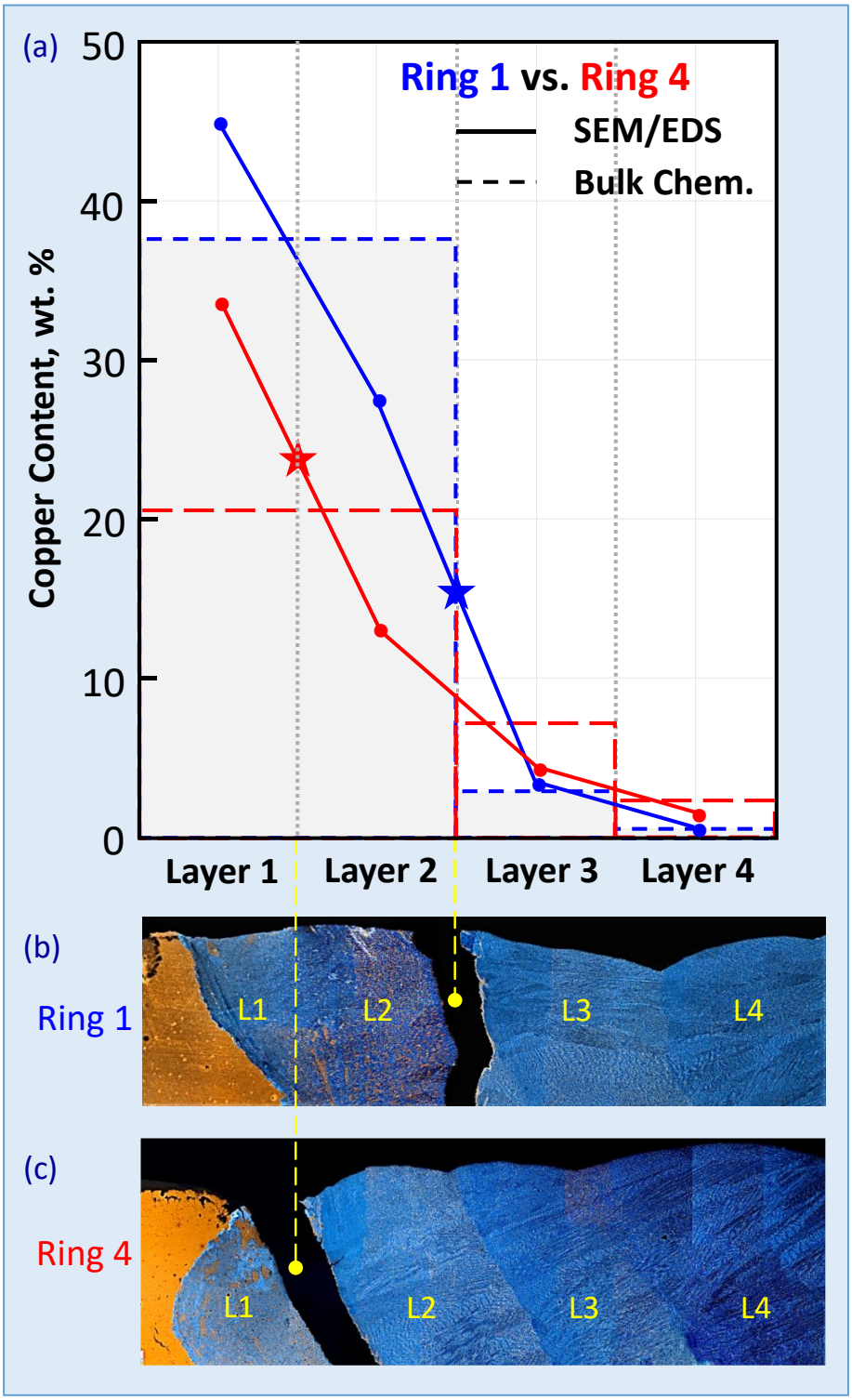

Figure 32. Possible correlation between Cu gradient and location of crack formation: (a) bulk chemical analysis and EDS data; (b), fracture at the L2/L3 boundary in Ring 1; (c), fracture at the L1/L2 boundary in Ring 4.

The independent results are comparable and the bulk chemistry data reveal that the total Cu content is actually lower in Ring 4 than Ring 1, particularly in L1 and L2. The EDS data reveal that the plots for Ring 4 and Ring 1 have the same slope, indicating that the Cu gradient is similar. However, the area beneath the curve is less, indicating that the total Cu content is lower. When combined, the two datasets reveal that the average Cu content of L1 + L2 ≈ 37 wt.% in Ring 1 and only ≈ 22 wt.% in Ring 4. The presence of less Cu is indicative of less solute mixing in the build, which is in apparent conflict with the higher substrate temperature. Evidently, the change in the location of crack initiation in the semi-solid state is not related to a differential in Cu migration into the initial layers.

There is a plausible explanation for the lower total Cu content in Ring 4 than Ring 1 that may account for the differing crack location. The Cu from the GRCop-84 substrate contained in the first few layers will be highly fugitive under Inconel 625 deposition conditions [ref. 69]. The vapor pressure at 1500°C is 2.5×10^{-1} torr for Cu, and 7×10^{-3} torr for Ni [ref. 70]. The vaporization temperature at 10^{-5} torr is 942°C for Cu, and 1142°C for Ni [ref. 71]. The higher superheat and average bulk temperature employed for Ring 4 implies increased Cu loss. A possible consequence is that the Cu-rich film forms at an interlayer boundary closer to the substrate. This eventuality may have shifted the location of crack initiation at an interlayer boundary from L2/L3 in Ring 1 to L1/L2 in Ring 4. The subsequent solidification of the Cu/Ni solid solution may have influenced the location of crack propagation in the solid state.

Formation of a weak phase at an interlayer boundary creates an interface susceptible to de-bonding via a mismatch in strength (aka GB embrittlement) [refs. 43and 44]. The RT yield strength of monolithic Inconel 625 is in the range of σ_y = 350-485 MPa in the as-solidified condition (table 1). In contrast, the CuNi30 alloy exhibits a RT yield strength in the range of σ_y = 120-250 MPa in the as-cast condition. Inconel 625 layers containing interdendritic Cu segregation are likely to exhibit an intermediate RT yield strength. It may be argued that an interlayer boundary containing abundant Cu-rich phases has the lowest fracture resistance among all boundaries. This includes the substrate/build interface that is heavily decorated with Laves phases and possibly Cr_2Nb dispersoids that tend to be strong, but brittle [refs. 54and 72]. Current observations are consistent with the cohesive strength of the interface being sufficient that fracture initiated elsewhere.

The attempt to correlate solute mixing of the dissimilar alloys with the location of extended crack growth in the solid state is illustrated in figure 33. Estimates of the localized variations in yield strength resulting from the distribution of Cu in the Inconel 625 deposit are postulated in figure 33(a). A strong Inconel 625 - Inconel 625+lo Cu boundary, ③, containing low interlayer Cu is shown in figure 33(b). A weak Inconel 625+lo Cu - Inconel 625+hi Cu boundary, ②, decorated with the CuNi30 phase is shown in figure 33(c). A strong Inconel 625+hi Cu - GRCop-84 interface, ①, decorated with non-Cu intermetallic phases is shown in figure 33(d).

The variations in estimated yield strength as a function of build height show that an interlayer boundary continuously decorated with a CuNi30 alloy phase represents a favorable crack path. In addition, the influence of such a YSM phenomenon would be at a maximum between that particular boundary and the directly adjacent layers. The solute gradient determines the Cu content of the layer beneath the boundary and the local solute distribution governs the amount of Cu segregated at the interlayer. The location within the build of the boundary at which this segregation is most prominent has the lowest probability of accommodating thermally-induced

stresses. Therefore, the distribution of Cu, as manifested by regional variations in yield strength, may be correlated with the preferential path for crack propagation in the solid state.

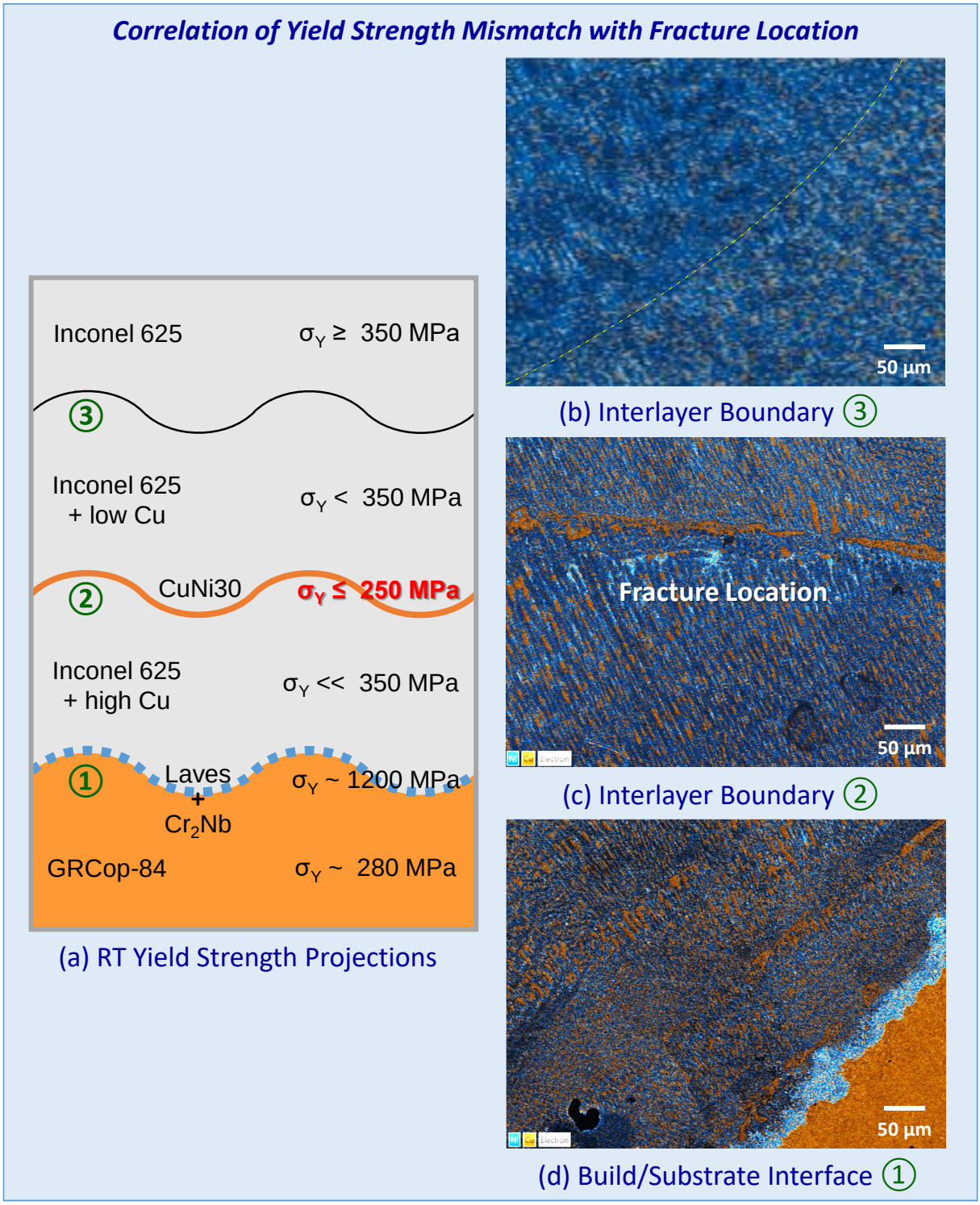

Figure 33. Potential correlation between location-dependent strength and preferential fracture path: (a), RT yield strength associated with the initial layers and interlayers; (b), strong, low Cu interlayer; (c), weak, high Cu interlayer; (d), strong, non-Cu bearing intermetallics at the substrate/build interface.

4.3. Fractographic Evidence

Variations in the fracture morphology through the build cross-section are consistent with cracking over a broad temperature range in both Ring 1 and Ring 4. The fracture behavior can be categorized into two regimes, namely crack formation and crack opening, that appear to be temperature-dependent. Crack formation refers to crack initiation and early crack propagation via progressive fracture, and crack opening refers to extensive crack growth via unstable fracture. The non-equilibrium solidus of $T_s \approx 1{,}170°C$, based on the ≈ 30 wt.% Ni content of the Cu-rich interlayer, represents the lower limit for the semi-solid state. The data suggest that crack formation occurred at super-solidus temperatures and crack opening at sub-solidus temperatures. Crack initiation in B7 was by hot cracking in Ring 1 and Ring 4. Early crack propagation in B6 was by warm cracking in Ring 1, but hot cracking persisted in Ring 4. Extensive crack growth by cold cracking commenced in B5 in Ring 1, but was delayed beyond B5 in Ring 4.

In Ring 1 and Ring 4, the fractographic evidence reveals that cracking occurred exclusively along a single interface separating consecutive layers of deposited beads. The loss of epitaxy across the separated interlayer boundary effectively resulted in the crack path following a high-angle GB. Therefore it may be inferred that crack formation was dominated by IGF in both instances. The surface topography is consistent with IGF through the Cu-rich interlayer phase in B7, B6, and B5 of the layer beneath the crack. In B7, crack initiation occurred at super-solidus temperatures in the semi-solid state for both ring sections. In B6 of Ring 1, early crack propagation occurred at temperatures just below the solidus in the solid state. In B5 of Ring 1, extensive crack growth occurred at temperatures approaching ambient in the solid state. In B6 and B5 of Ring 4, early crack propagation continued at super-solidus temperatures, i.e. in the semi-solid state. In contrast with Ring 1, the crack morphology indicates that the transition to extensive crack growth in the solid state did not occur in B5. This is a consequence of the differing EBF^3 conditions and likely reflects the higher bulk temperature employed during deposition of Ring 4.

Reports specific to interpass, rather than interbead, fracture during multi-pass welding are sparse, particularly in relation to the semi-solid state. Such boundaries are more prevalent in a layer additive build than is customary in multiple bead welds. In this case, attributing hot cracking to an established phenomena, such as SC, LC, or WMLC, may be open for debate. As illustrated in figure 8, both SC and LC involve GB segregation that culminates in IGF [ref. 28]. SC is associated with terminal liquid entrapment between converging solidification fronts [ref. 36]. It follows that SC occurs during boundary formation within the FZ, i.e. at SGBs. In contrast, LC involves localized fusion of low melting point constituent residing at pre-existing boundaries [ref. 36]. During single pass welding, LC occurs at GBs in parent metal within the HAZ. Likewise, WMLC occurs at GBs in previously deposited weld metal during multi-pass welding [ref. 37].

The contention with interpreting the present observations arises from the fact that WMLC is customarily associated with interbead boundaries residing out of the welding plane [ref. 48]. Invoking the characteristics of LC where fracture exhibits multiple orientations, WMLC at interbead boundaries oriented parallel with the welding plane can be expected. Such interfaces between consecutive rows of beads constitute interlayer boundaries in a layer-by-layer AM scenario. The physical constraints in the current build, that is freestanding and circular, differ from those commonly encountered in multi-pass welding [ref. 37]. It is reasonable to attribute

hot cracking to WMLC in the PMZ at a 'pre-segregated' interface, driven by differential thermal contraction [ref. 35].

Beyond B7 in Ring 1, the crack morphology is consistent with solid state fracture at elevated temperatures in B6, and temperatures closer to ambient in B5. In B6, the fracture characteristics may conform with established modes and mechanisms, but the alloy mixing and unique microstructure may alter conditions. In contrast with precipitation-strengthened Ni-base alloys, solid solution-strengthened alloys, such as Inconel 625, are normally not prone to warm cracking by DDC, RC, or SAC phenomena [ref. 36]. However, the abundant quantities of a Cu-rich phase created by blending with GRCop-84 may increase the susceptibility. The progressive fracture may be the result of TMF or LCF phenomena caused by the repetitive heating [ref. 40]. This raises the possibility that such elevated temperature, solid state mechanisms may have contributed to the fracture behavior. In B5, the fracture characteristics are commensurate with unstable crack growth involving cold cracking phenomena. Common descriptors include tensile overload, or 'pop-in' fracture caused by excessive residual stresses [ref. 45]. The location of the crack path within the Cu-rich interlayer in response to thermally-induced stresses also suggests that the proposed YSM phenomenon exerted a major influence on solid state fracture [ref. 44].

In Ring 4, hot cracking appears to persist through B7, B6, with a possible transition to warm cracking in B5. The predominant fracture mode during hot cracking entails decohesive rupture through an interlayer phase in the semi-solid state. The surface topography exhibits features reminiscent of immersion in liquid metal and is suggestive of fracture via a LME-type mechanism [ref. 43]. The changing fracture characteristics are consistent with a progressively decreasing thickness of molten interlayer phase [ref. 35]. In B5, this reduction in the volume of terminal liquid permits the underlying dendritic structure to emerge and the classic 'eggcrate' pattern to form. This fracture morphology has been attributed to material that is in either a melted or re-solidified condition [ref. 41]. The increased sharpness of the topographic features could be an indicator of a contribution from elevated temperature, solid state fracture. This warm cracking behavior has been described as macroscopically brittle, but microscopically ductile; when such limited plastic deformation is involved in fracture [ref. 42].

During the EBF^3 operations, the detection of crack opening was difficult and detecting crack formation was impractical. Deposition of Ring 1 was terminated when crack opening was detected, hence the lesser, ~ 36 mm build height. In contrast, crack opening was not detected during deposition of Ring 4 and the build progressed to the scheduled height of ~ 66 mm. In the absence of real-time diagnostics, such as thermal imaging, visual inspection was the only method available. Line-of-sight was restricted by the geometry of the processing equipment, particularly the surrounding vacuum chamber. Although the timeline for crack formation was indeterminate, the data presented provide some insight on the temperature-dependence of fracture events.

The fractographic results from both deposits are consistent with crack formation by hot cracking at super-solidus temperatures. This is in apparent conflict with cracking only being detected during post-deposition cooling in Ring 4. However, this discrepancy can be resolved if it is assumed that crack formation resulted in hairline fractures undetected during deposition. Consequently, it was surmised that the detection of cracks was only possible in the event of extensive crack growth. This explanation indicates that the current fractographic analyses of temperature-dependent characteristics are incomplete. Examination of mating fracture surfaces and spectrographic analysis of the fracture surfaces may provide more definitive evidence.

4.4. Driving Forces

The metallurgical factors considered so far do not include the driving forces responsible for the premature cracking. Thermal contraction was constrained by the circular geometry of the builds creating residual stresses, a very similar scenario to the circular patch weld test shown in figure 7 [ref. 37]. Two temperature-dependent sources were compatible with creating a crack-opening moment in the vicinity of the substrate/build interface. As shown in figure 34, tensile stresses were generated both by shrinkage strains while the deposit was in the semi-solid state, and by differential thermal contraction upon reaching the solid state. Potentially, both make a contribution at intermediate temperatures surrounding the solidus, i.e. in a localized semi-solid state.

The temperature regimes over which these mechanisms were active were separated by the non-equilibrium solidus, $T_s \approx 1{,}170°C$. At super-solidus temperatures, solidification shrinkage of the semi-solid Inconel 625 was constrained by the solid GRCop-84. At sub-solidus temperatures, thermal contraction of the GRCop-84 substrate was constrained by the Inconel 625 build. Therefore, material in the vicinity of the interface was subjected to bending/tearing loads throughout the processing temperature window.

The volumetric shrinkage associated with the liquid-to-solid transition in Inconel 625 is ≈ 8 vol.% as the temperature decreases from 1500°C to 20°C [refs. 52and 73]. This constitutes the driving force for crack initiation involving hot cracking phenomena. As indicated previously in figure 10, the mean CTE in the 20-1000°C range for GRCop-84 and Inconel 625 is 19.2×10^{-6} m/m-°C and 16.6×10^{-6} m/m-°C, respectively [refs. 53and 57]. Therefore, thermal contraction was ≈ 16% greater in the substrate than in the deposit following solidification. This constitutes the primary driving force for extensive crack growth via cold cracking phenomena. A combination of the two constitutes the driving force for early crack propagation including warm cracking phenomena.

The target substrate temperature during EBF^3 was $T_{Sub} \leq 250°C$ for Ring 1 and $T_{Sub} = 400$-550°C for Ring 4. Therefore, the process was frequently interrupted during deposition of Ring 1; the pauses between layers allowing the substrate temperature to equilibrate at $T_{Sub} \approx 250°C$. By contrast, the processing schedule was almost continuous during deposition of Ring 4; such interruptions proving unnecessary to maintain the substrate at $T_{Sub} \approx 500°C$. This difference in EBF^3 operations may be used to explain why crack opening was detected during deposition of Ring 1, but after deposition of Ring 4. It is suggested that the magnitude of residual stresses only became sufficient to cause extensive crack growth at $T_{Sub} \leq 250°C$. Higher processing temperatures may also have promoted hot cracking in B7 through B5 in Ring 4.

The temperature of the Ring 1 build entered this regime during the cooling intervals between every layer. However, the Ring 4 build was not subjected to such thermal excursions and only entered this temperature regime during post-deposition cooling. It is probable that unstable fracture only occurred during periods of static cooling in both cases. This also substantiates the notion that the event may be categorized as cold cracking, since the temperature is far below the non-equilibrium solidus, $T_s \approx 1{,}170°C$. Further, the final build height was ≈ 36 mm in Ring 1, but increased to ≈ 66 mm in Ring 4, resulting in almost twice the deposit volume. Such an increase in thermal mass would reduce the cooling rate and delay the effects of differential CTE.

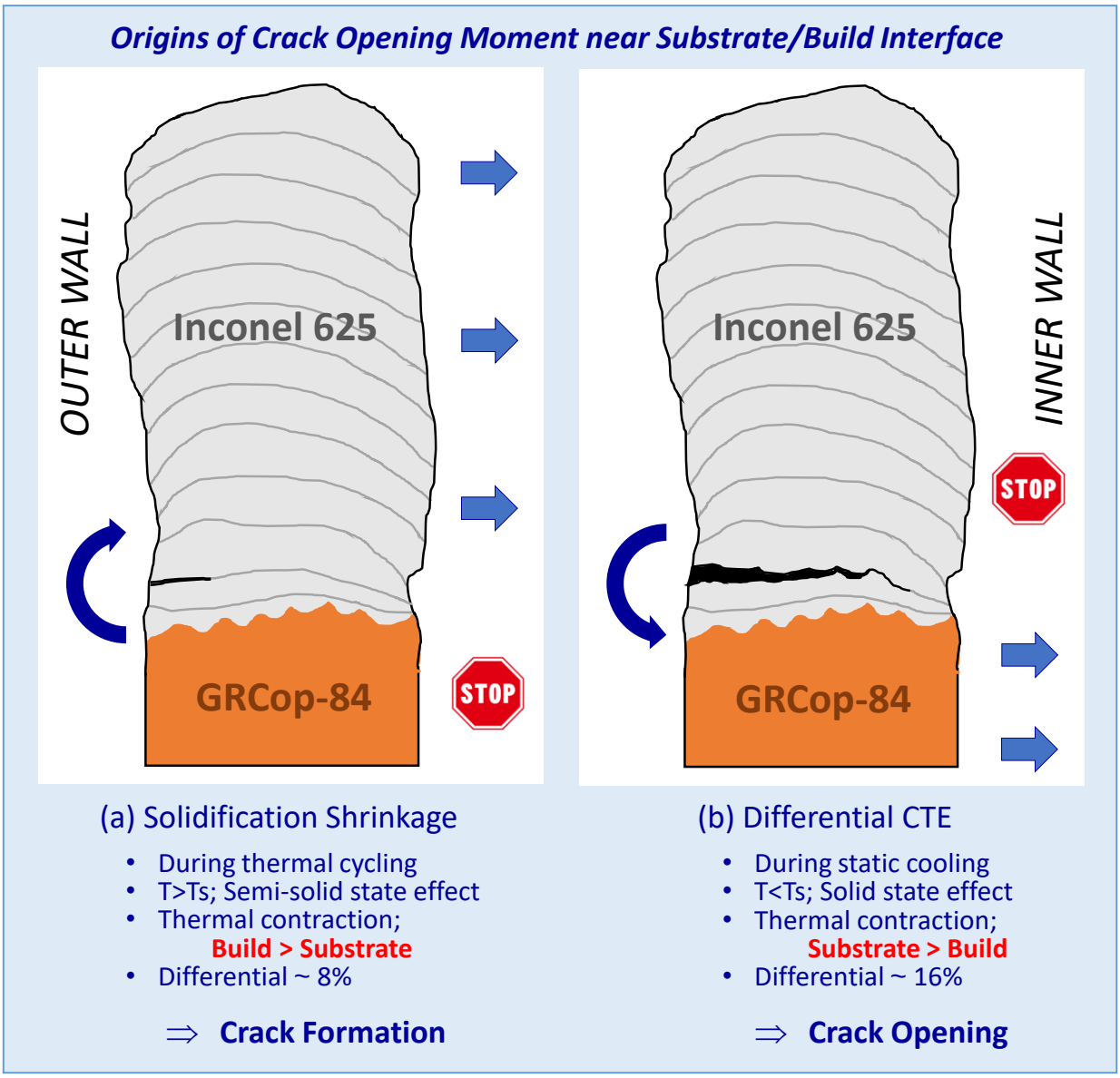

Figure 34. Origins of crack-opening moment in the vicinity of the substrate/build interface: (a), solidification shrinkage in Inconel 625; (b), differential CTE between Inconel 625 and GRCop-84. Note that both generate tensile/tearing loads over a broad temperature range.

5. Summary

1) A series of EBF^3 trials designed to alleviate premature cracking during axial deposition of Inconel 625 onto a cylindrical GRCop-84 substrate was unsuccessful. The focus of the parametric study was to reduce thermally-induced, residual stresses by progressively increasing the average bulk temperature. The processing conditions for Ring 1 and Ring 4 included in this failure investigation represented the lower and upper limit of the substrate temperature employed.

2) The substrate was preheated to T_{Sub} = 200-250°C prior to deposition of the initial layer in both cases. During deposition of subsequent layers, the temperature was restricted to $T_{Sub} \leq 250$°C for Ring 1 and maintained at T_{Sub} = 400-550°C for Ring 4. The most significant difference between the processing conditions was the frequency and duration of the beam-off intervals between successive layers in order to equilibrate the substrate at the target temperature.

3) In the case of Ring 1, the premature cracking was detected during deposition and the EBF^3 trial was aborted at a build height of ≈ 36 mm. In the case of Ring 4, the trial progressed to the scheduled build height of ≈ 66 mm and cracking was only detected during post-deposition cooling. The outer wall of both deposits exhibited circumferential cracks that were located in the vicinity of the Inconel 625/GRCop-84 interface.

4) In both ring sections, cracking occurred along an interlayer boundary within the build, rather than at the substrate/build interface. The deposited layers exhibited a cellular dendritic microstructure with epitaxial growth across most of the interlayer boundaries, with the exception of the boundary that succumbed to premature cracking in each case. The crack was located between layer 2 and layer 3 in Ring 1, and between layer 1 and layer 2 in Ring 4.

5) The cracked boundary exhibited unique microstructural characteristics that were common to both Ring 1 and Ring 4. In addition to the lack of microstructural bridging (epitaxy), interlayer segregation of abundant Cu-rich phase was another unique feature. The constituent comprised a cupronickel solid solution, demonstrated to have a Ni content of ≈ 30 wt.%. This alloy composition was commensurate with a much lower melting point and yield strength than the adjacent Inconel 625 layers.

6) It was surmised that the isolated interlayer boundary behaved like a high-angle GB and the fracture behavior could be classified as intergranular. The formation of the Cu-Ni30 phase in the semi-solid state caused a localized reduction in the solidus temperature of the Inconel 625 deposit from $T_s \approx 1{,}290$°C to $T_s \approx 1{,}170$°C. The net result was a significant increase in the STR (from ΔT = 60°C to ΔT = 180°C), the volume/longevity of terminal liquid, and the susceptibility to hot cracking.

7) Subsequently, the presence of the CuNi30 alloy phase in the solid state caused a local reduction in the yield strength of the build material from $\sigma_y \approx 350$ MPa to $\sigma_y \approx 250$ MPa. This created a weak interface at sub-solidus temperatures and a preferential crack path for

warm cracking and/or cold cracking. Therefore, IGF was promoted by the continuous film of interlayer segregation over the entire processing temperature range.

8) During the EBF^3 trials, deposition of the ring sections comprised seven overlapping beads (B1 through B7) in each of the ≈ 2 mm thick layers. The deposition sequence commenced at the inside diameter (B1) and advanced towards the outside diameter (B7). In Ring 1 and Ring 4, circumferential cracking started at the outer wall and progressed radially towards the inner wall, extending ≥ 80 % through the ≈ 19 mm wall thickness.

9) Fractographic data were consistent with crack formation during deposition and crack opening during periods of static cooling in both Ring 1 and Ring 4. The fracture morphology in Ring 1 indicated hot cracking in B7, warm cracking in B6, and cold cracking in B5. The fracture morphology in Ring 4 indicated fracture by hot cracking in B7 through B5. Decohesive rupture was the fracture mode with WMLC in the semi-solid state and tensile overload/ YSM in the solid state being the likely fracture mechanisms.

10) Crack initiation and early propagation in B7 and B6 likely involved progressive fracture driven by solidification shrinkage in the Inconel 625 build (≈ 8 vol.% mismatch). Extensive crack growth in B5 and beyond likely involved unstable fracture driven by differential CTE between the build and substrate (≈ 16 vol.% mismatch) after solidification. The alloy transition zone of the deposit where cracking occurred was subjected to tensile/tearing loads during both thermal cycling and static cooling.

11) It is important to emphasize that the premature cracking that hindered the production of test coupon materials was not encountered during EBF^3 of the rocket engine component. Differential thermal contraction in the circular cross-section created tensile forces within axial deposits, but compressive forces within radial deposits. As a consequence, solidification shrinkage and differential CTE did not generate a crack opening moment during cladding of the GRCop-84 thermal liner with the Inconel 625 structural jacket.

6. Recommendations

The implications of this investigation for applying DED/AM processes to the construction of multi-alloy components are significant. Accounting for differential thermal contraction over the entire processing temperature range is a necessity and in common practice. However, this study also demonstrates that a detailed understanding and careful control of alloy blending during EBF^3 of dissimilar materials may be paramount in producing deposits with high metallurgical and structural integrity. Using the deposition of Inconel 625 onto GRCop-84 as an example, the Ni content of any Cu-rich segregation governs T_s of the terminal liquid within the alloy transition zone. This is important because the susceptibility to hot cracking during EBF^3 increases with the width of the non-equilibrium STR.

This study suggests several approaches that might alleviate premature cracking during EBF^3 of dissimilar materials. The first approach is to reduce thermally-induced stresses by modifying the deposition sequence using incumbent EBF^3 parameters. The current sequence comprises depositing beads side-by-side, starting at the inner wall and progressing to the outer wall. A better sequence might involve depositing beads side-by-side, starting at the outer wall and progressing to the inner wall. An alternative is to employ a wider spacing for early beads and backfilling with later beads. A variation on this methodology might include building a 'fence' at the outer wall during initial deposition, or adjusting the deposition offset between adjacent beads.

The second approach is to transition the solidification mode from cellular dendritic to columnar dendritic grain growth using revised EBF^3 parameters. This might promote entrapment of the molten Cu-rich phase between growing dendrite colonies, thereby reducing the volume of terminal liquid ahead of the advancing S-L interface (figure 6). It is assumed that decreasing the total volume is difficult without adjusting the alloy composition, but it is possible to modify the distribution. The objective would be to discourage interlayer segregation oriented normal to the tearing load, and encourage interdendritic segregation oriented parallel with the tearing load. This could disrupt the continuity of the Cu-rich phase, increase the interlayer strength, and reduce the susceptibility to hot cracking.

The third approach is to introduce a 'buttering layer', thereby reducing the compositional gradient between the substrate and the deposit. There will be flexibility with regards to selection of deposition technique and the layer thickness needs to be compatible with the structural application. The composition of the feed wire needs to readily blend with both of the dissimilar materials if EBF^3 is employed. Monel 400 that is readily available as weld wire [ref. 74], is a good candidate for an intermediate layer during EBF^3 of Inconel 625 onto GRCop-84 Referring to figure 31, the STR of this Ni + 28-34 wt.% Cu alloy comprises $T_s \approx 1{,}170°C$ and $T_l \approx 1{,}240°C$, which is highly compatible. The binary composition also implies a solid solution alloy, i.e. the formation of no brittle, intermetallic phases during solidification.

Combining these approaches may prove to be the most effective method, i.e. reduce the driving force, modify the microstructure, and tailor the solute gradient. The proposed EBF^3 methodology concentrates on preventing crack formation, rather than arresting crack opening. The target is modification of the compositional transition within the alloy mixing zone adjacent to the substrate. These concepts may also apply to AM of dissimilar alloys using other DED processes, including powder-based techniques. This study also indicates that the orientation of functional gradients with respect to structural loads must be considered for AM involving alloys of any combination.

7. Acknowledgments

The authors are grateful to the following personnel at NASA-LaRC who provided technical assistance or guidance during this investigation (listed alphabetically):

- James M. Baughman: Analytical Mechanics Associates, Inc., D307
- Robert G. Bryant: NASA, Advanced Materials and Processing Branch, D307
- Jonny D. Callahan: Analytical Mechanics Associates, Inc., D307
- Harold D. Claytor: Analytical Mechanics Associates, Inc., D307
- Marcia S. Domack: NASA, Advanced Materials and Processing Branch, D307
- Richard E. Martin: NASA, Fabrication Technology Development Branch, D212B
- William J. Seufzer: NASA, Advanced Materials and Processing Branch, D307

The first author (SJH) dedicates this manuscript to the memory of his parents, Robert and Jessie Hales, without whose sacrifice his education would have been sparse. *Per ardua ad astra*

8. References

1. P.R. Gradl ..... and I.E. Locci, "Development and hot-fire testing of additively manufactured copper combustion chambers for liquid rocket engine applications," Proc. 53rd AIAA/SAE/ASEE Joint Propulsion Conf., Atlanta, GA, Paper# 4670, 27 pp., December 9, 2017.
2. W.S. Loewenthal and D.L. Ellis, "Fabrication of GRCop-84 rocket thrust chambers," Presentation at NASA Glenn Research Center, Cleveland, OH, January 12, 2006.
3. ***Standard for Additively Manufactured Spaceflight Hardware by Laser Powder Bed Fusion in Metals***, NASA Marshall Spaceflight Center, Huntsville, AL, MSFC-STD-3716, 93 pp., October 2017.
4. K.M. Taminger, J.K. Watson, R.A. Hafley, and D.D. Petersen, "Solid freeform fabrication apparatus and methods," US Patent # 7,168,935 B1, January 30, 2007.
5. V.R. Dave, ***Electron Beam (EB) – Assisted Materials Fabrication***, Ph.D. Thesis, Massachussetts Institute of Technology, Cambridge, MA, 280 pp., June 1995.
6. T.A. Rodrigues, V. Duarte, R.M. Miranda, T.G. Santos, and J.P. Oliveira, "Current status and perspectives on wire and arc additive manufacturing (WAAM)," Materials, vol.12, no. 7, pp.1121-1163, 2019.
7. A. Saboori ..... and M. Lombardi, "An overview of additive manufacturing of titanium components by directed energy deposition: Microstructure and mechanical properties," Appl. Sci., vol. 7, no. 9, paper# 883, 23 pp., 2017.
8. D. Ding, Z. Pan, D. Cuiuri, and H. Li, "Wire-feed additive manufacturing of metal components: technologies, developments and future interests," Int. J. Adv. Manuf. Technol., vol. 81, nos. 1-4, pp. 465-481, 2015.
9. W.J. Sames ..... and S.S. Babu, "The metallurgy and processing science of metal additive manufacturing," Int. Mater. Rev., vol. 61. no. 5, pp. 3115-360, 2016.
10. S. Stecker, "Electron beam layer manufacturing," US Patent # 8,546,717 B2, October 1, 2013.
11. C. Protz ..... and D. Willingham, "Additively manufactured low cost upper stage combustion chamber," NASA/TP-2019-000000, Marshall Spaceflight Center, Huntsville, AL, 2020. (in press)
12. J.N. DuPont, J.C. Lippold, and S.D. Kiser, "Alloying additions, phase diagrams, and phase stability," in ***Welding Metallurgy and Weldability of Nickel-Base Alloys***, John Wiley & Sons, Inc., Hoboken, NJ, pp. 15-25, 2009.
13. T.B. Massalski, J.L. Murray, L.H. Bennett, and H. Baker (eds.), ***Binary Alloy Phase Diagrams***, Amercian Society for Metals, Metals Park, OH, Vol. 1, 1100 pp., October 1986.
14. S. Floreen, G.E. Fuchs, and W.J. Yang, "The metallurgy of alloy 625," in ***Superalloys 718, 625, 706 and Various Derivatives***, E.A. Loria (ed.), TMS, Warrendale, OH, pp. 13-37, 1994.
15. Y. Chen, ... and Z. Li, "Characterization of heat affected zone liquation cracking in laser additive manufacturing of Inconel® 718," Mater. & Design, vol. 90, pp. 586-594, 2016.
16. J.J. Schirra, R.H. Caless, and R.W. Hatala, "The effect of Laves phase on the mechanical properties of wrought and cast + HIP Inconel® 718," in ***Superalloys 718, 625, and Various Derivatives***, E.A. Loria (ed.), TMS, Warrendale, OH, pp. 375-388, 1991.

17. E.R. Denlinger, J.C. Heigel, P. Michaleris, and T.A. Palmer, “Effect of inter-layer dwell time on distortion and residual stress in additive manufacturing of titanium and nickel alloys,” Mat. Proc. Tech., vol. 215, no. 1, pp. 123-131, 2015.
18. A. Theriault, L. Xue, and J.R. Dryden, “Fatigue behavior of laser consolidated IN-625 at room and elevated temperatures,” Mat. Sci. & Eng. vol. A516, nos. 1-2, pp. 217-225, 2009.
19. L.E. Murr ..... and R.B. Wicker, “Microstructural architecture, microstructures, and mechanical properties of a nickel-base superalloy fabricated by electron beam melting,” Met. & Mat. Trans., vol. 42A, no. 11, pp. 3491-3508, 2011.
20. F. Xu ..... and B. Xu, “Microstructural evolution and mechanical properties of Inconel® 625 alloy during pulsed plasma arc deposition process,” Mater. Sci. Technol., vol. 29, no. 5, pp. 480-488, 2013.
21. D.L. Ellis and R.L. Dreshfield, “Preliminary evaluation of a powder metal copper-8Cr-4Nb alloy,” Proc. Conf. on ***Advanced Earth-to-Orbit Propulsion Technology***, NASA, Washington DC, Marshall Spaceflight Center, AL, May 19-21, 1992.
22. K.R. Anderson, J.R. Groza, R.L. Dreshfield, and D. Ellis, “High-performance dispersion-strengthened Cu-8Cr-4Nb alloy,” Met. & Mat. Trans., vol. 26A, no. 9, pp. 2197-2206, 1995.
23. D.L. Ellis, W.S. Loewenthal, and H.M. Yun, ***Tensile Properties of GRCop-84***, NASA/TM-2012-217108, Glenn Research Center, Cleveland, OH, April 2012.
24. K.R. Anderson, J.R. Groza, R.L. Dreshfield, and D. Ellis, “Microstructural evolution and thermal stability of precipitation-strengthened Cu-8Cr-4Nb alloy,” Mat. Sci. Eng., vol. A169, pp. 167-175, 1993.
25. L.G. Vettraino ..... and J.C. Gibeling, “Influence of processing on the microstructure of Cu–8Cr–4Nb,” Mat. Sci., vol. 43, no. 19, pp. 6546-6555, 2008.
26. A.H. Seltzman and S.J. Wukitch, “Brazing, laser, and electron-beam welding of additively manufactured GRCop-84 copper for phased array lower hybrid launchers,” IEEE Trans. on Plasma Sci., 6 pp., 2020.
27. J.C. Lippold, “Welding metallurgy principles,” ***Welding Metallurgy and Weldability***, John Wiley & Sons, Inc., Hoboken, NJ, pp. 9-83, 2014.
28. T.W. Nelson, J.C Lippold, and M.J. Mills, “Nature and evolution of the fusion boundary in ferritic-austenitic dissimilar weld metals, Part 1 - Nucleation and growth,” Welding Journal, Research Supplement, vol. 78, no. 10, pp. 329s- 337s, 1999.
29. W.F. Savage, E.F. Nippes, and T.W. Miller, “Microsegregation in 70Cu-30Ni weld metal,” Welding Journal, Research Supplement, vol. 55, no. 6, pp. 165s-173s, 1976.
30. J.N. DuPont, J.C. Lippold, and S.D. Kiser, “Welding metallurgy,” in ***Welding Metallurgy and Weldability of Nickel-Base Alloys***, John Wiley & Sons, Inc., Hoboken, NJ, pp. 57-90, 2009.
31. U. Heubner, M. Kohler, and B. Prinz, “Determination of the solidification behavior of some selected superalloys,” ***Superalloys 1988***, TMS, Warrendale, PA, pp. 437-447, 1988.
32. G.A. Knorovsky ..... and W.F. Hammeter, “Inconel 718: A solidification diagram,” Metall. Trans., vol. 20A, no. 10, pp. 2149-2158, 1989.
33. K.N. Amato ..... and S. Collins, “Comparison of microstructures and properties for a Ni-base superalloy (Alloy 625) fabricated by electron and laser beam melting,” Mat. Sci. Res., vol. 1, no. 2, pp. 3-41, 2012.

34. F. Hanning, “Weld cracking in precipitation hardening Ni-based superalloys,” Ph.D. Thesis, Chalmers University, Gothenburg, Sweden, 45 pp., 2018.
35. J.C. Lippold, “Hot cracking,” ***Welding Metallurgy and Weldability***, John Wiley & Sons, Inc., Hoboken, NJ, pp. 84-129, 2014.
36. J.N. DuPont, J.C. Lippold, and S.D. Kiser, “Weldability,” in ***Welding Metallurgy and Weldability of Nickel-Base Alloys***, John Wiley & Sons, Inc., Hoboken, NJ, pp. 100-143, 2009.
37. S. Kou, “Solidification and liquation cracking issues in welding,” J. Metals, vol. 55, no. 6, pp. 37-42, 2003.
38. R.G. Baker, “Weldability and its implications for materials requirements,” Phil. Trans. Roy. Soc. London A, vol. 282, no. 1307, pp. 207-223, 1976.
39. A.J. Ramirez and J.C. Lippold, “High temperature behavior of Ni-base weld metal. Part II – Insight into the mechanism for ductility dip cracking,” Mat. Sci. Eng., vol. A380, nos. 1-2, pp. 245-258, 2004.
40. J.C. Lippold, “Fracture analysis,” ***Welding Metallurgy and Weldability***, John Wiley & Sons, Inc., Hoboken, NJ, pp. 311-332, 2014.
41. V. Kerlins, “Modes of fracture,” ***ASM Handbook – Fractography***, ASM International, Materials Park, OH, vol. 12, pp. 12-71, 1987.
42. W.T. Becker and S. Lampman, "Fracture appearance and mechanisms of deformation and fracture," ***ASM Handbook – Failure Analysis and Prevention***, ASM International, Materials Park, OH, vol. 11, pp. 559-586, 2002.
43. M. Kocak, “Structural integrity of welded structures: Process - Property - Performance (3P) relationship,” Proc. 63rd Ann. Assembly & Int. Conf. of the Int. Inst. of Welding, Istanbul, Turkey, pp. 3-19, July 2010.
44. U. Zerbst ..... and D. Klingbeil, “Review on fracture and crack propagation in weldments - A fracture mechanics perspective,” Eng. Frac. Mech., vol. 132, no. 12, pp. 200-276, 2014.
45. F. Matsuda and H. Nakagawa, “Some fractographic features of various weld cracking and fracture surfaces with scanning electron microscope: Studies on fractography of welded zone (I),” Trans. JWRI, vol.6, no. 1, pp. 81-90, 1977.
46. V.C. Kreuter and J.C. Lippold, "Ductility-dip cracking susceptibility of commercially pure Ni and Ni-base alloys utilizing the strain-to-fracture test." in ***Cracking Phenomena in Welds IV***, T. Boellinghaus, J.C. Lippold, and C.E. Cross (eds.), Springer, Switzerland, pp. 145-159, 2016.
47. S.C. Ernst, W.A. Baeslack III, and J.C. Lippold, “Weldability of high-strength, low-expansion superalloys,” Welding Journal, Research Supplement, vol. 61, no. 10, pp. 418s-430s, 1989.
48. C. Fink and M. Zinke, “Welding of nickel-based alloy 617 using modified dip arc processes,” Weld World, vol. 57, no. 5, pp. 323-333, 2013.
49. K.R. Vishwakarma, N.L. Richards, and M.C. Chaturvedi, “Microstructural analysis of fusion and heat affected zones in electron beam welded ALLVAC® 718PLUS™ superalloy,” Mat. Sci. Eng., vol. A480, nos. 1-2, pp. 517-528, 2008.
50. J.R. Davis (ed.), “Properties of cast copper alloys,” ***ASM Specialty Handbook: Copper and Copper Alloys***, ASM International, Materials Park, OH, pp. 529-563, 2001.
51. M.J. Cieslak, “The welding and solidification metallurgy of Alloy 625,” Welding Journal; Research Supplement, vol. 70, no. 2, pp. 49s–56s, 1991.

52. S. Birks, S. Roberts, and R. Leese, “Advances in materials technology for fossil power plants,” Proc. 7th Int. Conf. EPRI 2013, D. Gandy and J. Shingledecker (eds.), ASM International, Materials Park, OH, pp. 491-503, 2014.
53. J.R. Davis (ed.), “Properties of superalloys,” ***ASM Specialty Handbook: Heat-Resistant Materials***, ASM International, Materials Park, OH, pp. 219-271, 1997.
54. M. Takeyama and C.T. Liu, “Microstructure and mechanical properties of Laves-phase alloys based on Cr_2Nb,” Mat. Sci. & Eng., vol. A132, no. 2, pp. 61-66, 1991.
55. Copper Development Association, Inc., New York, NY, “Copper-nickel alloys: properties, processing, applications,” German Copper Institute (DKI), Echterdingen, Germany, 2017. https://www.copper.org/applications/marine/cuni/properties/DKI_booklet.html#2.1 accessed May 2 2019.
56. University of California-San Diego, http://www-ferp.ucsd.edu/LIB/PROPS/PANOS/cu.html accessed May 2 2019.
57. H.C. de Groh, D.L. Ellis, and W.S. Loewenthal, “Comparison of GRCop-84 to other Cu alloys with high thermal conductivities,” Mat. Eng. Perf., vol. 17, no. 4, pp. 594-606, 2008.
58. P. Verbnik, “VDM® Alloy 625”, VDM Metals, Werdohl, Germany, Data Sheet No. 4118, Rev. 01, May 2018; https://www.vdm-metals.com/fileadmin/user_upload/Downloads/Data_Sheets/Data_Sheet_VDM_Alloy_625.pdf
59. C.A. Johnson, ***Metallography Principles and Procedures***, Leco Corporation, St Joseph, MI, 77 pp., 2001.
60. ASTM E407-07, “Standard practice for microetching metals and alloys,” ASTM International, West Conshohocken, PA, 2015.
61. G.F. Vander Voort, E.P. Manilova, and G.M. Lucas, “Metallographic techniques for superalloys,” Microscopy and Microanalysis, vol. 10, no. S02, pp. 690-698, 2004.
62. K.B. Small, D.A. Englehart, and T.A. Christman, “Etching specialty alloys,” Adv. Mater. & Proc., vol. 33, no. 2, pp. 32-37, 2008.
63. Arcos Industries, LLC, Mt. Carmel, PA; http://www.arcos.us/nickel.asp accessed May 2 2019.
64. ATI Metals Corporation, Pittsburgh, PA; https://www.atimetals.com/Products/powder-metals accessed May 2 2019.
65. M.J. Cieslak, “A melting and solidification study of Alloy 625,” Met. Trans., vol. 19A, no. 9, pp. 2319-2331, 1988.
66. E. Chauvet ..... and G. Martin, “Hot cracking mechanism affecting a non-weldable Ni-based superalloy produced by selective electron beam melting,” Acta Mater., vol. 142, pp. 82-94, 2018.
67. F. Matsuda, H. Nakagawa, and K. Sorada, “Dynamic observation of solidification and solidification cracking during welding with optical microscope (I),” Trans. JWRI, vol.11, no. 2, pp. 67-77, 1982.
68. J.C. Lippold, “Solid state cracking,” ***Welding Metallurgy and Weldability***, John Wiley & Sons, Inc., Hoboken, NJ, pp. 130-212, 2014.
69. M.C. Hebeisen ..... and W.H. Pfeifer, “Vaccum melting and casting of superalloys,” NASA Technology Utilization Report, National Aeronautics and Space Administration, Washington DC, SP-5095, 175 pp., 1971.

70. R.E. Honig, "Vapor pressure data for the solid and liquid elements," RCA Review, Princeton, NJ, vol. 30, pp. 285-305, 1969.
71. S. Das, “On some physical aspects of process control in direct selective laser sintering of metals - Part II,” Proceedings Ann. Int. Symp. Solid Freeform Fabrication, University of Texas, Austin, TX, pp. 94-101, 2001.
72. J.D. Livingston, “Laves phase superalloys ?,” Physica Status Solidi A, vol. 131, no. 2, pp. 415-423, 1992.
73. H. Hosaeus, A. Seifter, E. Kaschnitz, and G. Pottlacher, “Thermophysical properties of solid and liquid Inconel® 718 alloy”, Int. J. High Temperatures–High Pressures, vol. 33, pp. 405-410, 2001.
74. K. Miller, ***MONEL® Alloy 400***, Special Metals Corporation, New Hartford, NY, Publication SMC-053, 16 pp., February 2005.

REPORT DOCUMENTATION PAGE

Form Approved
OMB No. 0704-0188

1. REPORT DATE *(DD-MM-YYYY)*
1-08-2020

2. REPORT TYPE
Technical Publication

3. DATES COVERED *(From - To)*

4. TITLE AND SUBTITLE
Electron beam freeform fabrication of dissimilar materials: Cracking in Inconel 625 on GRCop-84

5a. CONTRACT NUMBER

5b. GRANT NUMBER

5c. PROGRAM ELEMENT NUMBER

6. AUTHOR(S)
Hales, Stephen J.; Domack, Christopher S.; Brown Taminger, Karen M.

5d. PROJECT NUMBER

5e. TASK NUMBER

5f. WORK UNIT NUMBER
081876.02.07.18.01.01.01

7. PERFORMING ORGANIZATION NAME(S) AND ADDRESS(ES)
NASA Langley Research Center
Hampton, VA 23681-2199

8. PERFORMING ORGANIZATION REPORT NUMBER

9. SPONSORING/MONITORING AGENCY NAME(S) AND ADDRESS(ES)
National Aeronautics and Space Administration
Washington, DC 20546-0001

10. SPONSOR/MONITOR'S ACRONYM(S)
NASA

11. SPONSOR/MONITOR'S REPORT NUMBER(S)
NASA-TP-2020-5005040

12. DISTRIBUTION/AVAILABILITY STATEMENT
Unclassified
Subject Category
Availability: NASA STI Program (757) 864-9658

13. SUPPLEMENTARY NOTES

14. ABSTRACT
Anadditive manufacturing technology, known as electron beam freeform fabrication,was used in theconstructionofa prototyperocket engine component. The structural configuration comprised a cylindrical combustion chamber integrated with a conical thrust nozzle with an approximate wall thickness of 20 mm.The bi-metallic design exploited the physical properties of a Cu-based alloyfor the thermal liner and the mechanical properties of a Ni-based alloy for the surrounding structural jacket. The successfulproject culminatedin the radial deposition ofInconel®6251alloy cladding onto apre-fabricated,complex structure ofGRCop-84alloy.

15. SUBJECT TERMS
Additive manufacturing; Electron beam; Wire feed; Dissimilar metals; Solute mixing; Microstructural gradients; Weld cracking

16. SECURITY CLASSIFICATION OF:			17. LIMITATION OF ABSTRACT	18. NUMBER OF PAGES	19a. NAME OF RESPONSIBLE PERSON
a. REPORT	b. ABSTRACT	c. THIS PAGE			STI Help Desk (email: help@sti.nasa.gov)
U	U	U	UU	83	19b. TELEPHONE NUMBER *(Include area code)* (757) 864-9658